FINAL PROJECT REPORT

"Investigating the potential for long-term permeable reactive barrier (PRB) monitoring from the electrical signatures associated with the reduction in reactive iron performance", Environmental Management Science Program (EMSP), U.S. Department of Energy, DE-FG07-02ER63506, project period 09/15/02-09/14/05

PI: Lee D. Slater, Department of Earth & Environmental Sciences, Rutgers University, Newark, NJ 07102, E-mail: lslater@andromeda.rutgers.edu

Co-PI: Nic Korte, Private Consultant, 1946 Clover Court, Grand Junction, Colorado. 81506, E-mail: nkorte1@hotmail.com
Co-PI: Joe Baker, Honeywell Federal Manufacturing & Technologies, 2000 East 95th Street, Kansas City, Missouri, E-mail: jbaker@kcp.com

Contributing scientist: Andrew Binley, Department of Environmental Science, Lancaster University, LA1 4YQ, United Kingdom, E-mail: a.binley@lancaster.ac.uk

1 Summary of objectives and experiments conducted

The objective of this work was to conduct laboratory and field experiments to determine the sensitivity of low frequency electrical measurements (resistivity and induced polarization) to the processes of corrosion and precipitation that are believed to limit permeable reactive barrier (PRB) performance. The research was divided into four sets of experiments that were each written up and submitted to a peer-reviewed journal:
[1] A laboratory experiment to define the controls of aqueous chemistry (electrolyte activity; pH; valence) and total zero valent iron (Fe^0) available surface area on the electrical properties of Fe^0 columns.
[2] A laboratory experiment to determine the impact of corrosion and precipitation on the electrical response of synthetic Fe^0 columns as a result of geochemical reactions with $NaSO_4$ and $NaCO_3$ electrolytes.
[3] Laboratory experiments on a sequence of cores retrieved from the Kansas City PRB to determine the magnitude of electrical and geochemical changes within a field active PRB after eight years of operation
[4] Field-scale cross borehole resistivity and induced polarization monitoring of the Kansas City PRB to evaluate the potential of electrical imaging as a technology for non-invasive, long-term monitoring of indicators of reduced PRB performance.

2 Overview of report structure

This report first summarizes the findings of the four major experiments conducted under this research. The reader is referred to the four papers in Appendices 1-4 for a full description of each experiment, including motivation and significance, technical details, findings and implications. The deliverables of the project, including the publications, conference papers and new collaborative arrangements that have resulted are then described. Appendices 5-6 contain two technical reports written by co-PI Korte

describing (1) supporting geochemical measurements, and (2) the coring procedure, conducted at the Kansas City PRB as part of this project.

3 The experiments and primary findings

3.1 Experiment #1: Controls of aqueous chemistry (electrolyte activity; pH; valence) and total Fe^0 available surface area on the electrical properties of Fe^0 columns.

This experiment was designed to isolate the controls of fundamental physicochemical properties of saturated Fe^0 columns on low-frequency electrical measurements. The electrical response (0.1–1000 Hz) of reactive iron barriers was investigated by making measurements on zero valent iron (Fe^0)-sand columns under the following conditions: (1) variable Fe^0 surface area (0.1–100% by volume Fe^0) under constant electrolyte chemistry; (2) variable electrolyte activity (0.01–1 mol/liter), valence (mono-tri valent), and pH under constant Fe^0-sand composition; and (3) forced precipitation of iron hydroxides and iron carbonates on the Fe^0 surface. The measurements were modeled in terms of a conduction magnitude (σ_0), polarization magnitude (m_n), and polarization relaxation time (τ).

The key findings of this experiment are:

[1] Polarization magnitude exhibits a linear relation to the surface area of Fe^0, whereas conduction magnitude is only weakly dependent on the Fe^0 concentration below 30% by volume Fe^0.

[2] Polarization magnitude shows a power law relation to electrolyte activity, with exponents decreasing from 0.9 for monovalent solutions to 0.7 for trivalent solutions.

[3] The relaxation time (τ) parameter depends on activity and valence in a manner that is partly consistent with the variation in double layer thickness predicted from theory.

[4] pH exerts minor control on the electrical parameters.

[5] Polarization magnitude and relaxation time both increase as a result of precipitation induced on the surface of Fe^0.

The results are significant as they show that induced polarization parameters systematically change in response to changes in the Fe^0-electrolyte interfacial chemistry.

This work was conducted by PI Slater, postdoctoral scientist Jaeyoung Choi and Ph.D. candidate Yuxin Wu. It was published in “Slater, L., Choi, J. and Wu, Y., 2005, Electrical properties of iron-sand columns: implications for induced polarization investigation and performance monitoring of iron-wall barriers, Geophysics, 70, 4, G87-G94”. The full paper describing the findings is presented in Appendix 1.

3.2 Experiment #2: The impact of corrosion and precipitation on the electrical response of synthetic Fe^0 columns as a result of geochemical reactions with simple aqueous solutions.

The objective of this study was to investigate the electrical signatures of corrosion and precipitation in relatively simple, synthetic geochemical systems. Column studies were conducted to investigate the application of resistivity and induced polarization to monitor precipitation in Fe^0 columns using (a) Na_2SO_4 (0.01 M, dissolved oxygen (DO) = 8.8 ppm), and (b) Na_2CO_3 (0.01 M, DO = 2.3 ppm) solutions. An increase in complex

conductivity terms (maximum 40% in sulfate column and 23% in carbonate column) occurred over 25 days. Scanning electron microscopy (SEM) identified mineral surface alteration, with greater changes in the high DO sulfate column relative to the low DO carbonate column. X-ray diffractometry (XRD) identified reduced amounts of hematite/maghemite in both columns, precipitation of goethite/akaganeite in the sulfate column, and precipitation of siderite in the carbonate column. Nitrogen adsorption measurements showed increases in specific surface area of iron minerals (27.5% for sulfate column and 8.2% for carbonate column). As variations in electrolytic conductivity and porosity were minimal, electrical changes are attributed to (1) higher complex interfacial conductivity due to increased surface area and mineralogical alteration and (2) increased electronic conduction due to enhanced electron transfer across the iron-fluid interface. The results conclusively show that electrical measurements are a proxy indicator of Fe^0 surface alteration.

This work was performed by PI Slater, Ph.D. candidate Yuxin Wu and co-PI Korte. It was published in "Wu, Y., Slater, L. and Korte, N., 2005, Effect of precipitation on low frequency electrical properties of zero valent iron, Environmental Science & Technology, 39, 9197-9204". The full paper describing the findings is presented in Appendix 2.

3.3 Experiment #3: Electrical measurements on a sequence of reacted cores retrieved from the Kansas City PRB.

The objective of this experiment was to determine the electrical signature associated with the reacted front in an active field PRB installation. The electrical signatures of iron corrosion and mineral precipitation in angle cores from the Kansas City Fe^0 barrier installation in operation for eight years were measured. The real and imaginary parts of the complex electrical conductivity measured between 0.1-1000 Hz were 2-10 times higher (varying between cores) in the reacted zone at the upgradient edge of the barrier relative to less altered locations inside the barrier. Scanning electron microscopy (SEM) identified iron surface alteration with thickest corrosion rinds closest to the upgradient soil/iron interface. Specific surface area of iron minerals was also greatest at the upgradient interface, gradually decreasing into the cores. X-ray diffractometry (XRD) identified precipitation of iron oxide/hydroxide, carbonate minerals, iron sulfide as well as green rusts, with mineral complexity decreasing away from the interface. The electrical measurements correlate very well with the solid phase analyses and verify that electrical methods could be used to assess or monitor iron corrosion and mineral precipitation occurring in Fe^0 barriers.

This work was conducted by PI Slater, Ph.D. candidate Yuxin Wu and co-PI Korte (co-PI Baker coordinated site logistics). It was submitted for publication in *Environmental Science and Technology* on 10/20/05. The full paper describing the findings is presented in Appendix 3.

3.4 Experiment #4: Synthetic and field-based electrical imaging of a field PRB installation over time

The objective of this study was to analyze the sensitivity of electrical imaging to the geochemical alteration of a zerovalent iron permeable reactive barrier (PRB) over time.

Complex resistivity measurements on laboratory cores from the Kansas City PRB were used to define the electrical properties of both unreacted and geochemically altered (reacted) iron as well as the growth rate of the reacted front on the up-gradient edge of the barrier. Laboratory results were used to generate models of the electrical structure of the PRB at 0, 15 and 30 years of operation. Synthetic cross-borehole resistivity and induced polarization data were generated and perturbed with errors representative of noise at the site. In order to generate reliable images of the engineered structure, a complex resistivity inversion was employed with a 'disconnect' in the regularization between the part of the finite element mesh (FEM) representing the internal structure of the barrier and the remainder of the FEM mesh. Synthetic results show that, although the internal structure of inverted images at 15 and 30 years does not accurately reflect the width of the reacted front modeled along the up-gradient edge of the barrier, perturbations to the internal structure of the imaged PRB are diagnostic of the growth of the reacted front. Cross-borehole electrical data obtained at the field site over a 15 month period demonstrate that the complex resistivity algorithm can reliably resolve the PRB target. Both resistivity and induced polarization reciprocal errors are low and the induced polarization data highly repeatable over this period. Changes in the electrical properties of the PRB over time were small, but consistent with growth of a reacted front based on the synthetic study.

This work was conducted by PI Slater and co-PI Binley (co-PI Baker coordinated site logistics). It was submitted for publication in *Geophysics* on 08/18/05. The full paper describing the findings is presented in Appendix 3.

4 Project deliverables

The deliverables of this project will include a series of four peer-reviewed journal articles, a sequence of conference presentations, invited workshop lectures and new collaborative arrangements with other scientists on Department of Energy (DOE) funded projects.

4.1 Peer reviewed journal articles:

The four journal articles describing work that was 100% supported by FG07-02ER63506 are:

1. Slater, L., Choi, J. and Wu, Y., 2005, Electrical properties of iron-sand columns: implications for induced polarization investigation and performance monitoring of iron-wall barriers, **Geophysics**, 70, 4, G87-G94.
2. Wu, Y., Slater, L. and Korte, N., 2005, Effect of precipitation on low frequency electrical properties of zero valent iron, **Environmental Science & Technology**, 39, 9197-9204
3. Wu, Y, Slater, L. and Korte, N., Low frequency electrical properties of corroded iron barrier cores, **Environmental Science & Technology**, Submitted 10/20/05.
4. Slater, L. and Binley, A., 2005, Case history - synthetic & field based electrical imaging of a zerovalent iron barrier: implications for monitoring long-term barrier performance, **Geophysics**, Submitted 08/18/05.

The following work was 20% supported by FG07-02ER63506 and 80% supported by grant DE-AC04-01-AL66850 awarded to Slater:

5. Slater, L. and Binley, A., 2003, Evaluation of permeable reactive barrier (PRB) integrity using electrical imaging methods, **Geophysics**, 68, 3, 911-921

4.2 Book chapters:

As a direct result of this geophysical research on PRBs, PI Slater and contributing scientist Binley were invited to write the following book chapter:

1. Slater, L. and Binley, A., Engineered barriers for pollutant containment and remediation: In, Vereeken, Ed., "Applied Hydrogeophysics", Revised and resubmitted 05/10/05

4.3 Dissertations:

The laboratory parts of this research form the dissertation of Ph.D. student Yuxin Wu at Rutgers University. Yuxin is expected to graduate in May 2006. The title of his dissertation is "Low frequency electrical properties of zero valent iron: implications for performance monitoring of permeable reactive barriers".

4.4 Conference presentations, workshop presentations and abstracts

This research has been presented at national and international meetings and workshops. Notable is that PI Slater and contributing scientist Binley were invited to present this work at the North Atlantic Treaty Organization (NATO) Advanced Research Workshop on "Soils and Groundwater Contamination: Improved Risk Assessment", July 26-30, 2004, St. Petersburg, Russia. The following seven presentations were 100% supported by FG07-02ER63506:

1. Wu, Y., Slater, L. and Korte, N., 2005, Electrical properties of reacted iron cores extracted from a permeable reactive barrier installation, Eos Trans. AGU, 86(52), Fall Meet. Suppl., Abstract H41F-0466
2. Slater, L., Binley, A. and Wu, Y., 2005, Synthetic and field based electrical tomography of a permeable reactive barrier: implications for monitoring barrier performance, Eos Trans. AGU, 86(52), Fall Meet. Suppl., Abstract H43J-06
3. Wu, Y., Slater, L. and Korte, N., 2004, Effects of precipitation and particle size on low frequency electrical properties of zero valent iron, Eos Trans., AGU, Abstract H21G-07
4. Slater, L., 2004, Interfacial electrical properties of soils measurable with induced polarization: implications for hydraulic characterization, contaminant assessment and monitoring of chemical and biological processes, NATO Advanced Research Workshop "Soils and Groundwater Contamination: Improved Risk Assessment", July 26-31, 2004, St. Petersburg, Russia, Abstract, INVITED
5. Binley, A. and Slater, L., 2004, "Imaging permeable reactive barriers using resistivity and IP methods", NATO Advanced Research Workshop "Soils and Groundwater Contamination: Improved Risk Assessment", July 26-31, 2004, St. Petersburg, Russia, Abstract, INVITED
6. Choi, J., Slater, L. and Wu, Y., 2003, Low-frequency electrical properties of zero valent iron sand columns: implications for monitoring the performance of reactive

iron wall barriers in DNAPL degradation, Partners in Environmental Technology Technical Symposium & Workshop, sponsored by SERDP and ESTCP, Dec. 2-4, 2003, Washington D.C., Poster #155, INVITED

7. Choi, J., Slater, L. and Wu, Y., 2003, Low-frequency electrical properties of zero valent iron-sand columns: implications for monitoring the performance of reactive iron wall barriers, American Geophysical Union Fall Meeting, Dec 6-10, 2003, San Francisco, CA, Abstract # H12H-06

4.5 Invited talks

PI Slater gave the following invited talks on this research:

1. "Characterizing the chemical and physical properties of permeable reactive barriers using induced polarization", University of Missouri-Rolla, Environmental Research Center Speaker Series, Rolla, Missouri, 2004
2. "Electrical properties of sand-Fe^0 columns: implications for long-term monitoring of PRB chemistry", NABIR Field Research Center (FRC) Annual Meeting, Oak Ridge, Tennessee, 2004

4.6 Collaborations resulting from this study

PI Slater was invited to collaborate on Environment Management Science Program (EMSP) grant "Characterization of Coupled Hydrological-Biogeochemical Processes using Geophysical Methods", DE-AC03-76SF00098 (Susan Hubbard, Lawrence Berkeley Laboratory, PI). Slater was responsible for measuring the electrical signatures associated with the microbial precipitation of metal sulfides. Slater serves as a co-PI on the funded project renewal for DE-AC03-76SF00098 submitted under EMSP DE-FG01-05ER05-12, April 26, 2005 (notified of funding 11/28/05). Two multi-author journal papers resulted from this collaboration:

1. Ntarlagiannis, D., Williams, K.H., Slater, L. and Hubbard, S., The low frequency electrical response to microbially induced sulfide precipitation, **Journal of Geophysical Research - Biogeoscience**, In Press.
2. Williams, K.H., Ntarlagiannis, D., Slater, L. Dohnalkova, A., Hubbard, S.S. and Banfield, J.F., 2005, Geophysical imaging of stimulated microbial biomineralization, **Environmental Science & Technology**, 39, 19, 7592-7600.

Slater is currently collaborating with Douglas LaBrecque (Multiphase Technologies LLC) on DE-FG02-04ER84013 "Autonomous cross-borehole induced polarization system for monitoring permeable reactive barriers" funded by the DOE Small Business Innovation Research (SBIR) Program (LaBrecque, PI). The goal of this project is to develop and test an autonomous resistivity system for long-term PRB monitoring. Slater is assisting with proof of concept laboratory studies and the possible implementation of this autonomous system at the Kansas City PRB. Long-term monitoring of the Kansas City PRB is being continued under this SBIR grant using the twelve electrical imaging borehole arrays installed as part of the EMSP work reported here. Finally, Slater also served as a co-PI on a new EMSP proposal, "Integrated nuclear magnetic resonance, complex resistivity and multiphase pore-scale modeling study of air/fluid/grain interfaces in porous media (Hai Huang, Idaho National Laboratory, PI) submitted under EMSP DE-FG01-05ER05-12, April 26, 2005.

APPENDIX 1

Slater, L., Choi, J. and Wu, Y., 2005, Electrical properties of iron-sand columns: implications for induced polarization investigation and performance monitoring of iron-wall barriers, **Geophysics**, 70, 4, G87-G94.

DE-FG07-02ER63506 - Final Project Report (Slater, PI)
GEOPHYSICS, VOL. 70, NO. 4 (JULY-AUGUST 2005); P. G87–G94, 7 FIGS., 1 TABLE.
10.1190/1.1990218

Electrical properties of iron-sand columns: Implications for induced polarization investigation and performance monitoring of iron-wall barriers

Lee D. Slater[1], Jaeyoung Choi[1], and Yuxin Wu[1]

ABSTRACT

We investigate the electrical response (0.1–1000 Hz) of reactive iron barriers by making measurements on zero valent iron (Fe^0)-sand columns under the following conditions: (1) variable Fe^0 surface area (0.1–100% by volume Fe^0) under constant electrolyte chemistry; (2) variable electrolyte activity (0.01–1 mol/liter), valence (mono trivalent), and pH under constant Fe^0-sand composition; and (3) forced precipitation of iron hydroxides and iron carbonates on the Fe^0 surface. We model the measurements in terms of conduction magnitude, polarization magnitude, and polarization relaxation time. Our key findings are:

- Polarization magnitude exhibits a linear relation to the surface area of Fe^0, whereas conduction magnitude is only weakly dependent on the Fe^0 concentration below 30% by volume Fe^0.
- Polarization magnitude shows a power law relation to electrolyte activity, with exponents decreasing from 0.9 for monovalent solutions to 0.7 for trivalent solutions.
- The relaxation time parameter depends on activity and valence in a manner that is partly consistent with the variation in double layer thickness predicted from theory.
- pH exerts minor control on the electrical parameters.
- Polarization magnitude and relaxation time both increase as a result of precipitation induced on the surface of Fe^0. Our results show that induced polarization parameters systematically change in response to changes in the Fe^0-electrolyte interfacial chemistry.

INTRODUCTION

At contaminated sites, the reactive iron wall barrier is an effective passive technology for the in-situ remediation of chlorinated solvents as well as heavy metals (Gilham and O'Hannesin, 1994). However, the effectiveness of these barriers depends on construction and installation meeting design specifications. Furthermore, concern exists regarding long-term (decade-scale) performance reduction as a result of oxidation and precipitation at the zero valent iron (Fe^0) surface (Gavaskar et al., 1998) as well as clogged pore space (Mackenzie et al., 1999). Thus, there is a need for technology that can (a) noninvasively image and verify the in-situ emplacement of a barrier and (b) monitor and warn of performance reduction, permitting remedial measures and minimizing increased contaminant concentrations at locations downgradient from the barrier.

Low-frequency electrical measurements are sensitive to pore-fluid chemistry and the electrochemistry of a metal-fluid contact. Slater and Binley (2003) demonstrate the utility of resistivity and induced polarization (IP) imaging for in-situ verification of iron wall barriers. They also consider IP to sense reduction in reactive barrier performance indirectly from the electrical response of mineral precipitation on the Fe^0 surface. Long-term monitoring could be achieved via electrical measurements using electrodes emplaced within the wall during construction or noninvasively using tomographic imaging.

Development of the IP method in mineral exploration has advanced understanding of the electrical properties of metal-rich, mineralized rocks. Near-surface environmental applications of IP related to metals potentially include characterization of metal-contaminated soils, monitoring of biogeochemical processes resulting in metallic mineral precipitation, and investigation of reactive iron walls. In our laboratory study, we investigate the sensitivity of resistivity and IP measurements to physicochemical properties of columns

Manuscript received by the Editor April 15, 2004; revised manuscript received November 13, 2004; published online July 7, 2005.
[1]Rutgers University, Department of Earth & Environmental Sciences, Newark, New Jersey 07102. E-mail: lslater@andromeda.rutgers.edu.
© 2005 Society of Exploration Geophysicists. All rights reserved.

containing Fe^0. We conduct measurements on Fe^0-sand mixtures as a function of (1) Fe^0 concentration and surface area of Fe^0 per unit pore volume (2) electrolyte and electrical double layer (EDL) chemistry and (3) Fe^0 surface precipitation induced by changes in redox chemistry. Results of this study and significance with respect to in-situ installation verification and long-term monitoring of Fe^0 reactive barriers are presented.

INDUCED POLARIZATION IN SAND-Fe^0 MIXTURES

We measure the frequency-dependent electrical response of soils in the laboratory using an impedance analyzer. Impedance magnitude and phase shift ϕ on the sample are recorded relative to a reference resistor following stimulation by a sine-wave current. Results are presented in terms of magnitude and phase or real and imaginary components of the impedance. It is personal choice whether to present measurements as sample impedance, resistivity, conductivity, or dielectric permittivity; all are calculable from the impedance and sample geometry. Each of these parameters contains a term for total energy storage and a term for total energy loss (Knight and Endres, 2005). In terms of measured resistivity magnitude $|\rho|$ or conductivity magnitude $|\sigma|$ and ϕ,

$$|\sigma| = \frac{1}{|\rho|} = \sqrt{(\sigma'^2 + \sigma''^2)} = \frac{1}{\sqrt{(\rho'^2 + \rho''^2)}}, \quad (1)$$

$$\phi = \tan^{-1}\left[\frac{\sigma''}{\sigma'}\right] = -\tan^{-1}\left[\frac{\rho''}{\rho'}\right], \quad (2)$$

where a single apostrophe represents real parts and a double apostrophe represents imaginary parts of the complex resistivity ρ^* and conductivity σ^*. At low frequencies (<1000 Hz) ohmic conduction (the loss term) dominates, occurring in nonmetallic soils as electrolytic conduction within the pore space and as surface conduction in the EDL at the grain-fluid interface. Physicochemical controls on electrolytic conduction (Archie, 1942) and surface conduction (Waxman and Smits, 1968; Sen et al., 1981) are well established. Electronic conduction occurs in metal-containing soils when metallic minerals form a continuous conduction path.

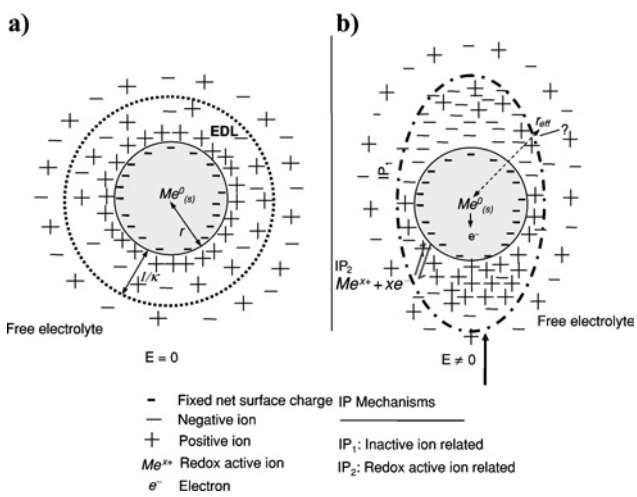

Figure 1. Conceptual model for possible polarization mechanisms in metal-particle-containing soils such as sand-Fe^0 mixtures. (a) No electric field; (b) application of electric field. IP_1 represents diffusion inactive ions normal to the metal surface; IP_2 represents electrochemical reaction between metal (Me_s) and metal ions in solution (Me^{x+}) (x represents the stoichiometric number). Symbols are r = metallic particle radius; $1/\kappa$ = EDL thickness; $r_{eff} = r + f(1/\kappa)$ is the postulated polarization sphere radius sensed with IP. EDL thickness is vastly exaggerated for illustration purposes (EDL theory assumes $1/\kappa << r$).

Wong (1979) attributes the polarization that occurs at a metal-electrolyte interface to two mechanisms. The first results from the flow of inactive ions in the mobile part of the EDL normal to the metal surface, resulting in the accumulation of inactive charge excess or deficit near the metal surface. The second results from a minor concentration of redox-active ions in solution engaging in electrochemical reactions and allowing charge transfer across the metal-electrolyte interface. These mechanisms are illustrated in the conceptual model presented in Figure 1. In this figure, the thickness of the EDL is grossly exaggerated for illustration; EDL electrochemical theory assumes that the EDL thickness $(1/\kappa) << $ grain radius r.

Relationships between the magnitude of the IP effect and the percentage of metallic mineral are documented (Pelton et al., 1978; Vanhala and Peltoniemi, 1992; Seigel et al., 1997; Bigalke and Junge, 1999). The speed of the movement of charged ions to and from such an interface results in a characteristic relaxation time of the polarization that is well related to the size of the metallic minerals in solution (Olhoeft, 1985). Experimental studies confirm that the characteristic time constant of the relaxation is proportional to the grain size of the metallic particles (Pelton et al., 1978; Wait, 1982; Olhoeft, 1985).

We note that the movement of the inactive ions is similar to the ion movement in the EDL at the grain-fluid interface generally attributed to the IP response in nonmetallic minerals. The difference is that whereas ion movement is predominantly normal to a metal-fluid interface, it is predominantly tangential to a nonmetallic mineral-fluid interface. This EDL polarization in nonmetallic soils is a function of grain surface area, surface charge density, and surface ionic mobility (Vinegar and Waxman, 1984; Schön, 1996; Lesmes and Frye, 2001). A strong, near-linear relationship between the surface area available for EDL ion migration and polarization magnitude is observed in sands and sandstone (Börner and Schön, 1991; Slater and Lesmes, 2002). Similar to IP observations in metallic mineral systems, the relaxation-time distribution is closely associated with the grain-size distribution (Lesmes and Morgan, 2001).

EXPERIMENTAL METHODS

Four-electrode electrical measurements were obtained with a dynamic signal analyzer (DSA) as illustrated by Slater and Lesmes (2002). Phase shift between current stimulus-voltage signal and impedance magnitude were measured at 40 frequencies, spaced at equal logarithmic intervals from 0.1 to 1000 Hz. Current was injected at silver coil electrodes at the sample ends. Sample voltage was measured using silver-silver chloride point electrodes placed in chambers on the edge of the sample holder (4 cm apart). Preamplification was used to boost the input impedance on the voltage channel to approximately 10^9 ohms, preventing current leakage into the circuitry. The frequency- and sample resistance-dependent phase response of the preamplifier was removed by obtaining

a calibration on a precision resistor matching the sample resistance. Repeatability tests indicate that errors are generally less than 0.5 mRad for the phase and 0.5% for impedance magnitude, respectively (Slater and Lesmes, 2002).

Experiments were first conducted to determine the sensitivity of IP measurements to the surface area of Fe^0 per unit pore volume [$S_{Fe(por)}$]. The specific surface area S_s of Ottawa sand (0.05 m^2/g; 0.63–0.71 mm in diameter) and Fisher Fe^0 40 mesh filings (2.8 m^2/g; approximately 0.4 mm in diameter) was measured in triplicate with a high-speed nitrogen gas sorption analyzer. Fisher filings were then uniformly mixed with Ottawa sand and packed into polyvinylchloride (PVC) columns (14 cm long, 2.5 cm in diameter). The sand-Fe^0 mixtures were first homogenized and then dry packed under the same pressure for each sample. The volume of Fe^0 filings to Ottawa sand varied from 0.1% to 100%. Samples were then saturated by gravity-siphoning influent electrolyte to the column under a constant head, with flow from bottom to top. One liter ($\approx$38 pore volumes) of 0.01 molar (M) sodium nitrate ($NaNO_3$) was passed through each column. The IP measurements were made after reaching equilibrium electrolyte conductivity in the column, when inflow and outflow electrolyte conductivity were equal. Sample porosity was calculated in triplicate from wet and oven-dried weight measurements. It varied between 0.35 and 0.38, increasing toward higher Fe^0 concentration.

We also conducted experiments on the sensitivity of IP measurements to changes in Fe^0 surface chemistry as a result of electrolyte chemistry. The effects of the electrolyte on low-frequency electrical measurements are commonly illustrated by plotting electrical parameters as a function of fluid conductivity σ_w or ionic concentration. IP measurements depend on the electrochemistry of the grain-fluid interface; it may therefore be more appropriate to consider the electrolyte activity a (Keevil and Ward, 1962). We examined the dependence of a, being the moles equivalent corrected for activity coefficient per liter of solution, and valence on the IP response. These measurements were performed on 5% Fe^0 filings by volume Fe^0-sand samples packed in PVC columns with the same dimensions as described previously. Five identical columns were assembled for simultaneous measurement using sodium nitrate $NaNO_3$, sodium chloride (NaCl), cadmium nitrate [$Cd(NO_3)_2$], calcium chloride ($CaCl_2$), and aluminum chloride ($AlCl_3$) electrolytes. One liter of electrolyte was passed through each column flushed with mono- and bivalent solutions, with measurements made at seven values of a varying between 0.01 and 1 mol/liter. The maximum activity for trivalent $AlCl_3$ was limited to 0.4 mol/liter to prevent precipitation of goethite at high activity. All samples were equilibrated for one to two days at each electrolyte activity interval investigated prior to measuring the electrical IP response. We used MINTEQA2 software (Allison et al., 1990) to model the aqueous geochemistry of our samples. The modeling predicted that no precipitates would form on the Fe^0 surface over this range of experimental parameters.

We examined the effect of pH on IP for a 5% by volume Fe^0-sand mixture saturated with 0.01 M $NaNO_3$. This experiment was conducted at five pH values (3.0, 5.5, 7.0, 8.5, and 10.5) by adding small amounts of 1 M nitric acid (HNO_3) or 1 M sodium hydroxide (NaOH). Induced polarization measurements were made only after reaching target pH and target electrolyte conductivity (0.09–0.11 S/m). We thus assessed the influence of pH independent of electrolyte conductivity.

We finally assessed the sensitivity of IP measurements to precipitation on the Fe^0 surface. Sand-Fe^0 columns were prepared at higher Fe^0 concentrations (30% and 70%) to increase the likelihood of detecting the effects of precipitation. Columns were initially saturated with 0.01 M $NaNO_3$ electrolyte to obtain a background (prior to precipitation) electrical measurement. We introduced precipitation by slowly invading each column with 1 liter of 1 M NaOH electrolyte; geochemical modeling with MINTEQA2 predicted the formation of iron (II) hydroxide [$Fe(OH)_2$] and iron (III) hydroxide [$Fe(OH)_3$] precipitates on the Fe^0 surface under these experimental conditions. Columns were then reinvaded with 1 liter of 0.01 M $NaNO_3$ to return the electrolyte chemistry to the background condition and electrical measurements obtained. The 70% Fe^0 column was then invaded with 1 liter of 0.5 M sodium carbonate (Na_2CO_3) electrolyte to encourage further precipitation; geochemical modeling with MINTEQA2 predicted the formation of iron (II) carbonate ($FeCO_3$) and iron (III) carbonate [$Fe_2(CO_3)_3$] under these conditions. Electrical measurements were again obtained after reinvasion with 1 liter of 0.01 M $NaNO_3$ to return the electrolyte chemistry to the background condition.

RELAXATION MODELING

We used a single Cole-Cole dispersion model (Cole and Cole, 1941) to define global conduction and polarization magnitudes as well as a characteristic relaxation time τ, where τ is related to the phase peak. The model was developed to simulate the electrical response of dielectrics and was later modified to simulate the IP response of metallic mineral-rich rocks (Pelton et al., 1978; Pelton et al., 1983). It is a purely phenomenological model, and the physicochemical significance of its parameters is unclear (Dias, 2000) although it has been treated for the IP response of sandstone (Lesmes et al., 2000). In this paper we investigate the empirical relationship between the model parameters and physicochemical properties of mixed Fe^0–sand systems. In terms of complex resistivity ($\rho^* = 1/\sigma^*$),

$$\rho^* = \rho_0 \left[1 - m \left(1 - \frac{1}{1 + (i\omega\tau)^c} \right) \right], \qquad (3)$$

where ρ_0 is the dc resistivity (inverse of dc ohmic conductivity), m is the chargeability, τ is the characteristic time constant, c is a shape parameter, and $i = \sqrt{-1}$. Interdependence between the model parameters must be considered in the interpretation. The chargeability determines the magnitude of the polarization storage relative to the conduction loss (Keller, 1959; Lesmes and Frye, 2001). The ratio m to ρ_0 provides a direct measure of the polarization magnitude (Lesmes and Frye, 2001), defined here as m_n. The time constant is related to the relaxation time of the interfacial polarization mechanism. However, it is a function of ρ_0, leading to potential confusion in the interpretation of the significance of changes in τ in systems where ohmic conduction varies considerably, e.g., under variable electrolyte conductivity. Some workers model $\tau \propto \rho_0$ (Pelton et al., 1978), whereas others model $\tau \propto \rho_0^2$ (Wait, 1982).

Previous workers identify mineral grain size as the primary petrophysical control on τ, with τ increasing as polarizable grain size increases (Pelton et al., 1978; Wong, 1979; Olhoeft, 1985). Larger grains are associated with larger EDL ion or redox ion diffusion distances. These relationships were observed under experimental conditions of near-invariant electrolyte chemistry. We suggest that electrolyte chemistry may also influence ionic diffusion length through its control on EDL thickness (Figure 1). As EDL thickness increases, we anticipate an increase in the relaxation time of the polarization mechanism because inactive and/or redox ions presumably diffuse over larger distances during an applied current. We thus suggest that the relaxation time measured with IP depends on an effective grain size r_{eff}, being the sum of the mineral radius and some function of EDL thickness (Figure 1). Activity and valence both exert a strong influence on EDL thickness. The Guoy-Chapman model of the EDL predicts that EDL thickness ($1/\kappa$) is inversely proportional to the square root of ion concentration C and inversely proportional to the electrolyte valence Z:

$$\kappa = \left(\frac{8\pi N Z^2 e^2 C}{\varepsilon k T}\right)^{1/2}, \tag{4}$$

where N is Avogadro's number, e is electronic charge, ε is the dielectric constant, k is Boltzman's constant, and T is temperature (Stumm and Morgan, 1996). From the considerations above we might expect an inverse relationship between electrolyte activity and polarization relaxation time and between valence and polarization relaxation time.

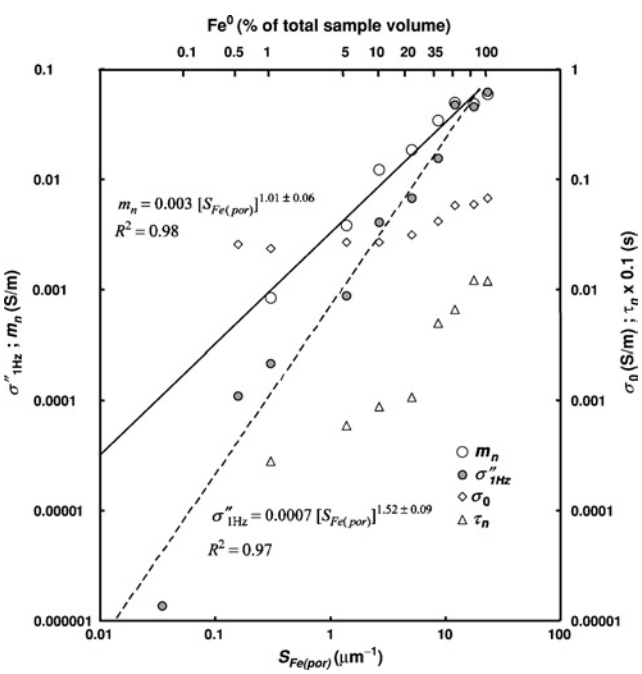

Figure 2. Cole-Cole model parameters as a function of Fe^0 surface area per unit pore volume $[S_{Fe(por)}]$ for Ottawa sand-Fe^0 samples that vary from 0.1% to 100% Fe^0 volume concentration: m_n = polarization magnitude; σ_0 = conduction magnitude; τ_n = normalized time constant. The imaginary conductivity measured at 1 Hz ($\sigma''_{1\text{Hz}}$) is also shown. Power-law relationships obtained from least-squares regression of measures of the polarization magnitude (m_n; $\sigma_{1\text{Hz}}$) are included. Linear correlation coefficients (R^2) are 0.99 and 0.987 for the m_n versus $S_{Fe(por)}$ and σ'' versus $S_{Fe(por)}$ relationships, respectively.

We inverted spectral data for the relaxation model parameters using an algorithm based on a conventional real-valued, least-squares approach with Marquardt regularization (Kemna, 2000). Starting model parameters were constrained to realistic values from the measured shape of the complex resistivity spectra. We found the following parameters most informative in terms of data interpretation and significance: σ_0 represented the conduction magnitude, m_n represented the polarization magnitude, and $\tau_n = \tau/\rho_0$ represented a relaxation time scaled to remove most of the effect of changes in ρ_0 between samples of varying electrolyte concentration. Although the physicochemical meaning of this parameter is unclear, we show that it exhibits the same variation as τ in systems where ρ_0 does not change appreciably. In systems where ρ_0 does change significantly, it reveals behavior showing some consistency with variation in EDL thickness predicted by equation 4. We find only small changes in c (0.36–0.55) in our measurements, so we omit it from our results.

RESULTS

Sand-Fe^0 mixtures as a function of Fe^0 surface area per unit pore volume $[S_{Fe(por)}]$

The dependence of m_n, (polarization magnitude), σ_0 (dc conduction magnitude), and τ_n on the surface area of Fe^0 per unit pore volume $[(S_{Fe(por)})]$ for Ottawa sand-Fe^0 mixtures between 1% and 100% Fe^0 by volume is shown in Figure 2. Below 1% Fe^0 concentration, the phase is only a few millirads and the inverse algorithm is unable to resolve the relaxation model parameters reliably. A linear correlation (coefficient, $R^2 = 0.98$) between m_n and $S_{Fe(por)}$ is revealed. The conductivity magnitude is practically independent of $S_{Fe(por)}$ between 0.1 and 10 μm^{-1} (1%–30% Fe^0 by volume) but increases with greater amounts of Fe^0 at higher Fe^0 concentration. We attribute this to the absence of significant continuous conduction paths at low-Fe^0 concentrations; the influence of Fe^0 on electronic conduction is only noticeable when such paths begin to form above 30% Fe^0 concentration. In contrast, the polarization is highly sensitive to small increases in the Fe^0 surface area and exhibits linear dependence across the entire range of Fe^0 concentration. We also plot the imaginary conductivity at 1 Hz ($\sigma''_{1\text{Hz}}$) (Figure 2); this defines the local polarization magnitude at 1 Hz. This single-frequency measure of the polarization magnitude also shows a good correlation ($R^2 = 0.97$) with $S_{Fe(por)}$ that extends down to 0.1% Fe^0 concentration (the lowest concentration measured).

Sand-Fe^0 mixtures as a function of activity and pH

Figure 3 illustrates the frequency shift in the phase spectra that results from changing only the electrolyte activity; we show ϕ for a 5% by volume Fe^0 sample saturated with $CaCl_2$ at three electrolyte activities (the resistivity magnitude is also shown for the $a = 0.09$ mol/liter solution). The frequency of the phase peak increases by more than an order of magnitude, with an order of magnitude increase in electrolyte activity. An example of the fit of the measured resistivity (plotted normalized to ρ_0) and phase for a 5% Fe^0 sample saturated with $a = 0.09$ mol/liter $CaCl_2$ to the Cole-Cole model is given in Figure 3.

Figure 4 shows σ_0 and m_n as a function of electrolyte activity for five electrolytes. The conduction magnitude σ_0 is linearly dependent on activity ($R^2 = 0.99$) for the monovalent, bivalent, and trivalent solutions, as expected given the dominance of electrolytic conduction in the 5% by volume Fe^0 sample (electronic conduction in 5% Fe^0 does not significantly influence σ_0; Figure 2). Polarization magnitude is also strongly correlated with a (linear correlation coefficient, $R^2 > 0.98$ in each case) with exponents less than one (Table 1). The weak dependence of polarization magnitude (shown here as measured $\sigma''_{1\text{Hz}}$) on a for a 100% sand sample is shown for comparison. There is a correlation between the m_n versus a relationship and the electrolyte valence. For the monovalent electrolytes the exponent is approximately 0.9; it is approximately 0.8 for the bivalent electrolytes and only about 0.7 for the trivalent electrolyte studied. Least-squares regressions for the smallest ($AlCl_3$) and largest (NaCl) m_n dependence on a are plotted in Figure 4.

Figure 5 shows the dependence of relaxation-time parameters on a. Here, we plot both τ(s) and τ_n (s S/m) to further

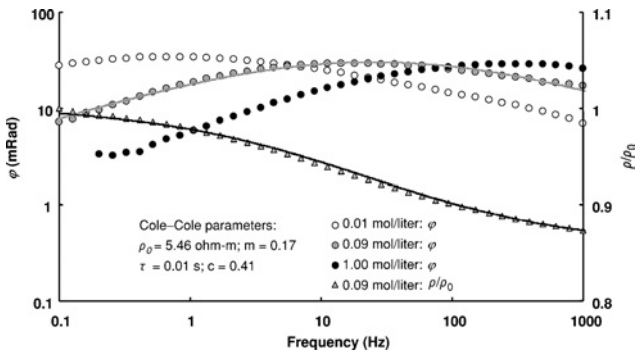

Figure 3. Phase spectra (0.1–1000 Hz) for a 5% Fe^0 by volume sand-Fe^0 sample at three electrolyte activities. The fit of the phase ϕ and relative resistivity magnitude ρ/ρ_0 at 0.09 mol/liter activity to a single Cole-Cole relaxation model is also shown. The ϕ below 0.3 Hz for the 1.0-mol/liter electrolyte is unreliable because of the low signal level and therefore is removed from the plot.

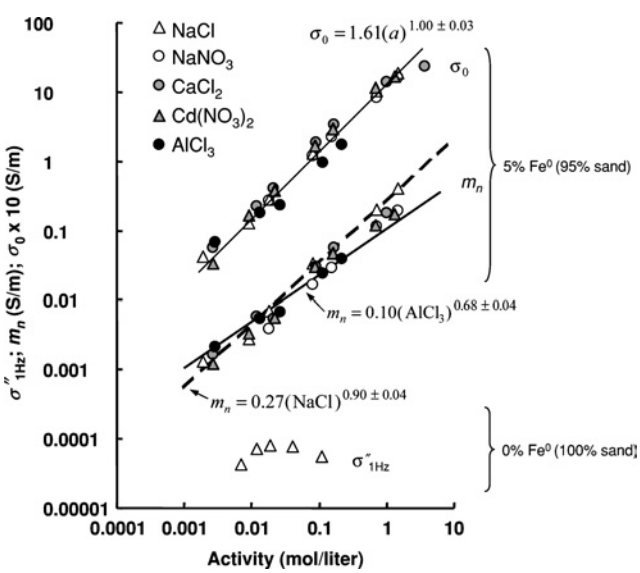

Figure 4. Cole-Cole conduction magnitude σ_0 and polarization magnitude m_n as a function of electrolyte activity and valence observed for a 5% Fe^0 by volume sand–Fe^0 sample. The measured polarization at 1 Hz ($\sigma''_{1\text{Hz}}$) is plotted for a 100% sand sample for comparison. Also shown are regression of σ_0 and activity for all monovalent and bivalent electrolytes as well as regression of m_n and activity for both NaCl and $AlCl_3$ solutions. In all cases $R^2 = 0.99$.

Table 1. Power-law exponent, standard error, and linear correlation coefficient (R^2) for the relationship between polarization magnitude (m_n) and electrolyte activity observed for monovalent, bivalent, and trivalent solutions.

Valence	Electrolyte	Exponent	Standard error	R^2
Monovalent	$NaNO_3$	0.89	0.02	0.99
	Nacl	0.90	0.04	0.99
Bivalent	$CaCl_2$	0.82	0.05	0.98
	$Cd(NO_3)_2$	0.83	0.04	0.99
Trivalent	$AlCl_3$	0.68	0.04	0.99

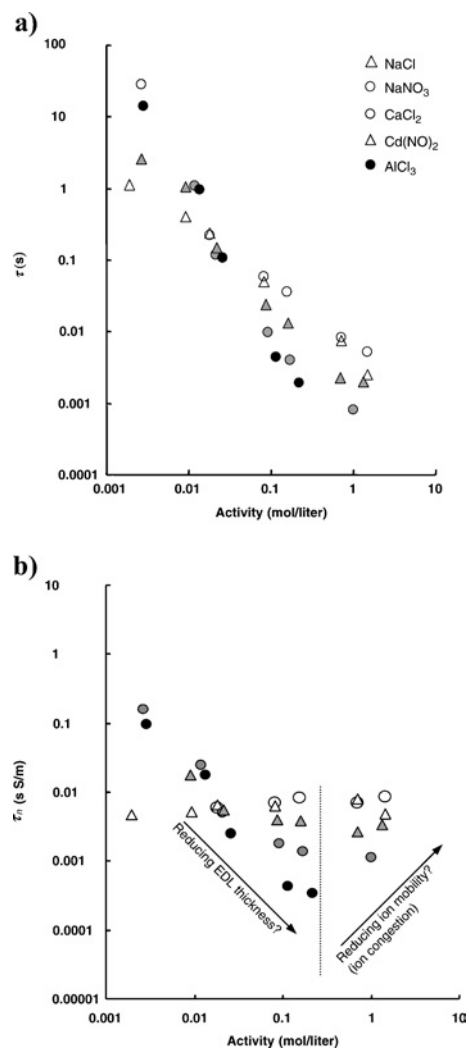

Figure 5. Cole-Cole model relaxation time parameters as a function of electrolyte activity and valence observed for a 5% Fe^0 by volume sand-Fe^0 sample. (a) Time constant τ; (b) normalized time constant ($\tau_n = \tau/\rho_0$). Refer to the Discussion section for an explanation of the annotation referring to behavior observed for bivalent and trivalent electrolytes.

illustrate the strong dependence of the resistivity on τ in systems where electrolyte conductivity varies significantly. For the monovalent electrolytes, the change in τ (Figure 5a) is almost entirely accounted for by the change in ρ_0 ($1/\sigma_0$), and there is thus only minor dependence of τ_n (τ/ρ_0) on a (Figure 5b). However, the bi- and trivalent electrolytes display a distinct dependence of τ_n on a; τ_n decreases when a is between 0.001 and 0.4 mol/liter. Above $a = 0.4$ mol/liter τ_n levels out and begins to increase with a for the $Cd(NO_3)_2$ electrolyte.

The dependence of σ_0, m_n, and τ_n on pH is shown for a 5% Fe^0 sample saturated with 0.01 M NaCl electrolyte in Figure 6. Both σ_0 and m_n are effectively pH independent across the investigated range. However, τ_n exhibits a distinct order of magnitude increase above pH $\approx$ 8. Below pH $\approx$ 8, τ_n is invariant. Here, ρ_0 does not change significantly, and the τ dependence on pH is essentially the same as shown for τ_n. This order of magnitude change in τ_n may coincide with the point of zero charge for Fe^0. The point of zero change was not measured during this experiment. However, the point of zero charge of iron oxides that coat the Fe^0 surface in aerobic conditions typically occurs at a pH of 6 to 8 (Stumm and Morgan, 1996).

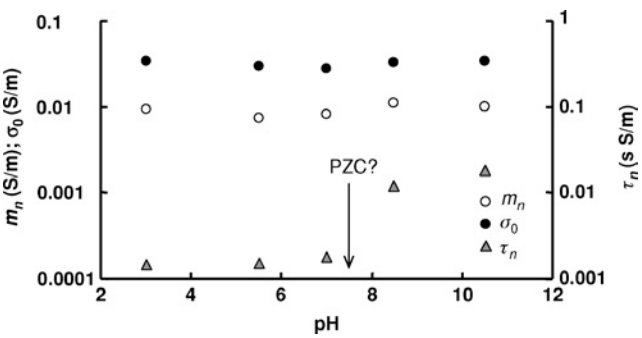

Figure 6. Cole-Cole model parameters as a function of pH for a 5% Fe^0 by volume Fe^0-sand sample saturated with 0.01 M $NaNO_3$ solution and doped with 1 M HNO_3 or 1 M NaOH. PZC denotes possible point of zero charge (see text for explanation).

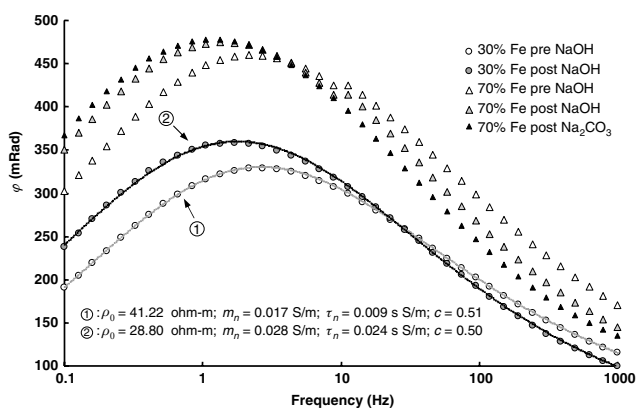

Figure 7. Phase versus frequency for 30% Fe^0 by volume and 70% Fe^0 by volume sand-Fe^0 samples before and after inducing precipitation on the Fe^0 surface by invasion with NaOH and Na_2CO_3. Cole-Cole model parameters for the 30% Fe^0 sample before and after invasion with NaOH are also shown. Note that measurements both before and after precipitation were made with the sample flushed with 1 liter ($\approx$ 38 pore volumes) of 0.01 M $NaNO_3$ solution.

Sand-Fe^0 mixtures as a function of aging

Figure 7 compares the phase ϕ as a function of frequency before and after inducing precipitation in the Fe^0 columns. For the 70% Fe^0 sample, we contrast the response after invasion by both NaOH and subsequent Na_2CO_3 electrolytes with the background column. For the 30% Fe^0 sample, we contrast only the response after invasion by NaOH. The Cole-Cole relaxation model parameters for the 30% Fe^0 sample before and after invasion with NaOH are also shown in Figure 7. The pre- and postprecipitation measurements were made at equal electrolyte composition and activity. Precipitation increases the magnitude of the phase peak and shifts the position of the phase peak to lower frequencies. This response is manifested in the relaxation model parameters by an increase in m_n and τ_n with precipitation.

DISCUSSION

Our results illustrate that IP measurements are sensitive to Fe^0 surface area per unit pore volume [$S_{Fe(por)}$]. We observe a strong linear correlation between $S_{Fe(por)}$ and polarization magnitude m_n obtained from relaxation models of sand-Fe^0 systems. There is a need for methods to verify the distribution of Fe^0 following the completion of permeable reactive barrier (PRB) installations. This is particularly important when new technologies (e.g., pressure injection) are used to emplace PRBs. IP is highly sensitive to changes in $S_{Fe(por)}$; the change in $S_{Fe(por)}$ associated with an increase from 0.1% to 1% Fe^0 concentration is readily resolved in our $\sigma''_{1\text{Hz}}$ measurements. Resistivity is capable of imaging PRB structures constructed of pure Fe^0 (Slater and Binley, 2003). In our experiments resistivity was insensitive to changes in Fe^0 surface area when the Fe^0 concentration was less than 30% of the sand-Fe^0 mixture. Similar findings are reported in a study by Endres et al. (2000).

Our results clearly favor IP as the most suitable low-frequency electrical method for the noninvasive investigation of PRB installations. The IP parameters are much more sensitive to Fe^0 concentration than resistivity parameters. However, electromagnetic coupling between instrumentation and the conductive earth makes IP field measurements extremely challenging at frequencies above a few hertz. In contrast, single-frequency (1 Hz or below) IP measurements are readily obtainable in the field. The polarization magnitude at 1 Hz ($\sigma''_{1\text{Hz}}$) is only slightly less correlated with $S_{Fe(por)}$ of Fe^0 as compared to m_n obtained from relaxation modeling of the spectral response. Thus, the single-frequency IP method appears to be a promising, field-deployable method for investigating PRBs.

Considering the relaxation time, τ_n increases with increasing $S_{Fe(por)}$, and there is an inflection point that coincides with the Fe^0 concentration where electronic conduction becomes significant (Figure 2). There is only a relatively small change in ρ_0 in these samples; τ and τ_n consequently show very similar behavior. The increase in τ_n suggests that the relaxation time of the interfacial polarization increases with increasing $S_{Fe(por)}$. Longer relaxation times are interpreted or modeled

in terms of an increase in the size of the polarization sphere (i.e., grain size), causing surface charge migration over greater distances. It is possible that aggregation of Fe^0 filings could increase the effective size of the polarized element. This is more likely to occur at the high Fe^0 concentrations and might partly reflect the steeper rise in τ_n above $S_{Fe(por)} = 10\ \mu m^{-1}$. Alternatively, a reduction in the mobility of polarized EDL ions as a result of surface ion congestion might occur at high Fe^0 concentration. The increase in τ_n with increasing $S_{Fe(por)}$ is consistent with the higher exponent in the σ''_{1Hz}-$S_{Fe(por)}$ relationship compared to the m_n-$S_{Fe(por)}$ relationship (Figure 3). As τ_n increases, the polarization peak shifts to lower frequencies (toward 1 Hz), contributing in part to the observed increase in σ''_{1Hz} with increasing $S_{Fe(por)}$.

We also show that IP measurements are sensitive to EDL chemistry at the Fe^0 surface. A power-law dependence of polarization magnitude on electrolyte activity (exponents vary from 0.68 to 0.89) is observed. This dependence of m_n on electrolyte activity reduces with increasing valence. The time constant of the relaxation after normalization for resistivity dependence varies with electrolyte activity (primarily for bivalent and trivalent electrolytes) and valence. Some of the observed variation is consistent with our interpretation of τ_n (the length scale of the polarized ion displacement) as a measure of an effective grain size defined as the sum of the particle radius and some function of electrolyte-dependent EDL thickness ($1/\kappa$). From the EDL theory (equation 4) we then anticipate an inverse relation between τ_n and both activity and valence. The bivalent and trivalent electrolytes indeed exhibit a decrease in τ_n with increasing activity when a is 0.001 to 0.4 mol/liter (see annotation in Figure 5). Furthermore, τ_n does decrease with increasing valence above $a = 0.02$ mol/liter. However, the increase in τ_n with activity above $a = 0.1$ mol/liter for the bivalent electrolytes, as well as the invariance of τ_n with activity for the monovalent electrolytes, suggests that factors other than EDL thickness influence τ_n. A possible explanation for the increase in τ_n with increasing activity above $a = 0.1$ mol/liter is a reduction in surface ionic mobility at these high concentrations (see annotation in Figure 5). Lesmes and Frye (2001) invoke such an effect to explain a reduction in polarization magnitude observed for sandstone samples at high electrolyte concentration.

Electrolyte pH did not significantly affect polarization magnitude for the NaCl electrolyte studied here. However, τ_n does change with pH. Since Fe^0 and Fe oxide minerals are categorized by pH-dependent surface charge (Sposito, 1989), it is possible that the observed jump in τ_n is related to a change in the surface charge characteristics of iron oxide minerals on the iron surface. Although our current work leaves questions regarding the dependence of IP measurements in Fe^0 containing materials on electrolyte chemistry, it has two distinct implications: (1) the migration of the inactive ions to/from the metal surface, rather than the electrochemical reaction associated with the redox active ions, dictates the IP response in these systems and (2) simultaneous monitoring of electrolyte chemistry at PRB sites is required for meaningful IP monitoring of PRB performance.

Precipitation in our columns increased the polarization magnitude and the time constant of the relaxation. The precipitates likely formed in our experiments [$Fe(OH)_2$; $Fe(OH)_3$; $FeCO_3$; $Fe_2(CO_3)_3$] are assumed to coat the Fe^0 surface, although some precipitation onto the sand might also have occurred. One possible explanation for the increase in m_n is that precipitation of iron hydroxide and/or iron carbonate minerals results in an increase in the surface area of reactive iron in contact with solution. This explanation assumes that precipitation results in a rougher metal mineral-fluid surface and consequently higher specific surface. The increase in τ_n is consistent with an increase in polarizable particle size that will result from precipitation forming on the iron surface. Our results show the potential for IP measurements to detect precipitation on iron surfaces as commonly associated with reduction in PRB reactivity and suggest that IP imaging may be a viable tool for long-term monitoring of PRB performance. Continuing work is focusing on experiments to determine the sensitivity of IP to precipitation under geochemical conditions simulating those observed at PRB installations.

CONCLUSIONS

Induced polarization parameters show a linear dependence on surface area of Fe^0 per unit pore volume [$S_{Fe(por)}$] in Fe^0–Ottawa sand mixtures. This relationship is strongest ($R^2 = 0.99$) when the global polarization magnitude is calculated from relaxation modeling accommodating the frequency dependence of the polarization between 0.1 and 1000 Hz. A weaker relationship ($R^2 = 0.97$) is obtained, over a wider range of percentage Fe^0 concentration, between $S_{Fe(por)}$ and imaginary conductivity at 1 Hz. Induced polarization for Fe^0–Ottawa sand mixtures depends on electrolyte activity but is largely unaffected by pH. The polarization magnitude shows a power-law dependence on electrolyte activity that weakens for higher-valent electrolytes. A relaxation-time parameter varies with electrolyte activity and valence in a manner partly consistent with the variation in electrical double-layer thickness at the Fe^0 surface predicted from Gouy-Chapman's electrical double-layer theory. Preliminary experiments suggest that precipitation onto the Fe^0 surface induced by changes in redox chemistry causes a measurable change in the polarization magnitude and relaxation time.

This laboratory study strongly supports the use of induced polarization for in-situ verification of PRB installations. Most significant, the IP magnitude is an excellent proxy indicator of the amount of iron surface area available for hydrocarbon degradation. The results also suggest that IP is a candidate technology for the long-term monitoring of geochemical changes that determine PRB performance. However, the dependence of the IP parameters on the electrolyte chemistry must be considered in the design of such PRB monitoring systems. The results of this study also have significance for other potential environmental applications of the IP method, including characterization of heavy metals and monitoring of microbial precipitation of heavy metals.

ACKNOWLEDGMENTS

This research was supported by the Environmental Management Science Program (EMSP) of the Office of Science, U.S. Department of Energy, grant DE-FG07-02ER63506. We are grateful to Andreas Kemna (Institute of Chemistry and Dynamics of the Geosphere, Forschungszentrum Jülich) for

providing a reliable algorithm for the estimation of Cole-Cole relaxation model parameters. We also thank David Lesmes (George Washington University) for his advice regarding the interpretation of Cole-Cole model parameters and Nic Korte for his input regarding the geochemistry of reactive iron barriers. Review comments provided by Andreas Weller and an associate editor of GEOPHYSICS improved the quality of this manuscript.

REFERENCES

Allison, J. D., D. S. Brown, and K. J. Novo-Gradac, 1990, MINTEQA2/PRODEFA2: A geochemical assessment model for environmental systems, version 3.0 user's manual: Environmental Research Laboratory, Office of Research and Development, U.S. Environmental Protection Agency.

Archie, G. E., 1942, The electrical resistivity log as an aid in determining some reservoir characteristics: Transactions of the American Institute of Mineral, Metallurgy and Petroleum Engineers, **146**, 54–62.

Bigalke, J., and A. Junge, 1999, Using evidence of non-linear induced polarization for detecting extended ore mineralizations: Geophysical Journal International, **137**, 516–520.

Börner, F. D., and J. H. Schön, 1991, A relation between the quadrature component of electrical conductivity and the specific surface area of sedimentary rocks: Log Analyst, **32**, 612–613.

Cole, K. S., and R. H. Cole, 1941, Dispersion and absorption in dielectrics, vol. I: Alternating current field: Journal of Chemical Physics, **9**, 341–351.

Dias, C., 2000, Developments in a model to describe low-frequency electrical polarization in rocks: Geophysics, **65**, 437–451.

Endres, A. L., S. D. Piggott, and J. D. Redman, 2000, Characterization of reactive treatment zones containing granulated iron using induction logging: 7th International Symposium on Borehole Geophysics for Minerals, Geotechnical and Groundwater Applications, Mineral and Geotechnical Logging Society, Proceedings, 1–8.

Gavaskar, A. R., N. Gupta, B. M. Sass, R. J. Janosy, and D. O'Sullivan, 1998, Permeable reactive barriers for groundwater remediation: Batelle Press.

Gilham, R. W., and S. F. O'Hannesin, 1994, Enhanced degradation of halogenated alophatics by zero valent iron: Ground Water, **32**, 958–967.

Keevil, N. B., and S. H. Ward, 1962, Electrolyte activity: Its effect on induced polarization: Geophysics **27**, 677–690.

Keller, G. V., 1959, Analysis of some electrical transient measurements on igneous, sedimentary and metamorphic rocks, *in* J. R. Wait, ed., Overvoltage research and geophysical applications: Pergamon Press, Inc., 92–111.

Kemna, A., 2000, Tomographic inversion of complex resistivity — Theory and application: Der Andere Verlag.

Knight, R., and A. L. Endres, 2005, Introduction to rock physics for near-surface applications in near-surface geophysics: SEG.

Lesmes, D. P., and K. M. Frye, 2001, The influence of pore fluid chemistry on the complex conductivity and induced-polarization responses of Berea Sandstone: Journal of Geophysical Research, **106**, 4079–4090.

Lesmes, D. P., and F. D. Morgan, 2001, Dielectric spectroscopy of sedimentary rocks: Journal of Geophysical Research, **106**, 13329–13346.

Lesmes, D. P., J. Sturrock, and K. M. Frye, 2000, A physiochemical interpretation of the Cole-Cole dielectric model: Symposium on the Application of Geophysics to Engineering & Environmental Problems, Proceedings 533–543.

Mackenzie, P. D., D. P. Horney, and T. M. Sivavec, 1999, Mineral precipitation and porosity losses in granular iron columns: Journal of Hazardous Materials, **68**, 1–17.

Olhoeft, G. R., 1985, Low-frequency electrical properties: Geophysics, **50**, 2492–2503.

Pelton, W. H., W. R. Sill, and B. D. Smith, 1983, Interpretation of complex resistivity and dielectric data: Part I: Geophysical Transactions, **29**, 297–330.

Pelton, W. H., S. H. Ward, P. G. Hallof, W. R. Sill, and P. H. Nelson, 1978, Mineral discrimination and removal of inductive coupling with multifrequency IP: Geophysics, **43**, 588–609.

Schön, J. H., 1996, Physical properties of rocks — Fundamentals and principles of petrophysics: Pergamon Press, Inc.

Seigel, H. O., H. Vanhala, and S. Nicholas Sheard, 1997, Some case histories of source discrimination using time-domain spectral IP: Geophysics, **62**, 1394–1408.

Sen, P. N., C. Scala, and M. H. Cohen, 1981, A self-similar model for sedimentary rocks with application to the dielectric constant of fused glass beads: Geophysics, **46**, 781–795.

Slater, L., and A. Binley, 2003, Evaluation of permeable reactive barrier (PRB) integrity using electrical imaging methods: Geophysics, **68**, 911–921.

Slater, L., and D. P. Lesmes, 2002, Electical-hydraulic relationships observed for unconsolidated sediments: Water Resources Research, **38**, 1213, doi: 10.1029/2001WR001075.

Sposito, G., 1989, The chemistry of soils: Oxford University Press.

Stumm, W., and J. J. Morgan, 1996, Aquatic chemistry: Chemical equilibria and rates in natural waters: John Wiley & Sons, Inc.

Vanhala, H., and M. Peltoniemi, 1992, Spectral IP studies of Finnish ore prospects: Geophysics, **57**, 1545–1555.

Vinegar, H. J., and M. H. Waxman, 1984, Induced polarization of shaly sands: Geophysics, **49**, 1267–1287.

Wait, J. R., 1982, Geo-electromagnetism: Academic Press Inc.

Waxman, M. H., and L. J. M. Smits, 1968, Electrical conductivities in oil-bearing shaly sands: Transactions of the American Institute of Mineral, Metallurgy & Petroleum Engineers, **243**, 107–122.

Wong, J., 1979, An electrochemical model of the induced-polarization phenomenon in disseminated sulfide ores: Geophysics, **44**, 1245–1265.

APPENDIX 2

Wu, Y., Slater, L. and Korte, N., Effect of precipitation on low frequency electrical properties of zero valent iron, **Environmental Science & Technology**, ASAP Web Release Date: 28-Oct-2005, DOI: 10.1021/es051052x.

Environ. Sci. Technol. **2005**, *39*, 9197−9204

Effect of Precipitation on Low Frequency Electrical Properties of Zerovalent Iron Columns

YUXIN WU,*,† LEE D. SLATER,† AND NIC KORTE‡

Department of Earth and Environmental Sciences, Rutgers University, Newark, New Jersey 07102, and 1946 Clover Court, Grand Junction, Colorado 81506

We conducted column studies to investigate the application of a noninvasive electrical method to monitor precipitation in Fe^0 columns using (a) Na_2SO_4 (0.01 M, dissolved oxygen (DO) = 8.8 ppm), and (b) Na_2CO_3 (0.01 M, DO = 2.3 ppm) solutions. An increase in complex conductivity terms (maximum 40% in sulfate column and 23% in carbonate column) occurred over 25 days. Scanning electron microscopy (SEM) identified mineral surface alteration, with greater changes in the high DO sulfate column relative to the low DO carbonate column. X-ray diffractometry (XRD) identified reduced amounts of hematite/maghemite in both columns, precipitation of goethite/akaganeite in the sulfate column, and precipitation of siderite in the carbonate column. Nitrogen adsorption measurements showed increases in specific surface area of iron minerals (27.5% for sulfate column and 8.2% for carbonate column). As variations in electrolytic conductivity and porosity were minimal, electrical changes are attributed to (1) higher complex interfacial conductivity due to increased surface area and mineralogical alteration and (2) increased electronic conduction due to enhanced electron transfer across the iron−fluid interface. Our results show that electrical measurements are a proxy indicator of Fe^0 surface alteration.

Introduction

The Fe^0 permeable reactive barrier (PRB) is an in situ technology for the remediation of chlorinated hydrocarbon, heavy metal, or radionuclide contaminated groundwater (*1*−*5*). Corrosion of the Fe^0 surface and subsequent precipitation of iron minerals causes performance reduction (*6*−*9*) in both synthetic and in situ PRBs (*6*, *7*, *9*−*12*). A critical issue is how to monitor performance reduction caused by oxide formation and the decreased permeability associated with pore clogging.

Electrical methods have been applied to study iron corrosion processes. Tafel scan and electrochemical impedance spectroscopy (EIS) analysis of iron has identified geochemical controls on the Fe^0 corrosion process (*13*−*15*). Electrical measurements have also been applied at the field-scale to image the in situ installation of Fe^0 barriers (*16*). In this study, we utilize an electrical method to measure the electrical response of iron columns during corrosion and precipitation. The measurement is analogous to an upscaled EIS measurement and is transferable to field-scale monitoring of PRBs.

* Corresponding author e-mail: yuxinwu@pegasus.rutgers.edu; phone: (973) 596-5863.

† Rutgers University.

‡ Consultant, Grand Junction, CO.

Electrical measurements on soils and minerals can be represented in terms of a measured frequency (ω) dependent complex conductivity $\sigma^*(\omega)$

$$\sigma^*(\omega) = \sigma^{/}(\omega) + i\sigma^{//}(\omega) \quad (1)$$

where σ' is the real part of $\sigma^*(\omega)$, being the conduction (energy loss) component, and σ'' is the imaginary part of $\sigma^*(\omega)$, being the polarization (energy storage) component ($i = \sqrt{-1}$). The physicochemical controls on electrical properties of soils depend on frequency, being the subject of an extensive volume of literature (a review can be found in ref *17*). At low frequencies (<1000 Hz), we identify three mechanisms of charge transfer in soils containing metallic minerals. First, σ_{el} is the conductivity of the electrolytic current path through the interconnected, fluid-filled pores (a real term); second, σ^*_{int} is a complex term describing conduction and polarization at mineral grain/electrolyte interfaces; and third, σ_{elc} accounts for electronic conduction (a real term) in metallic minerals. Equivalent circuit models can be formulated to simulate particular geometric arrangements of these conductivity mechanisms as described in the geophysical literature (*18*, *19*).

The σ_{el} is linearly dependent on the electrolyte conductivity (σ_w) and is also controlled by the pore space geometry (20). The σ^*_{int} incorporates both conduction along the electrical double layer (EDL) and polarization occurring at interfaces between metallic (and to a much lesser extent nonmetallic) minerals and electrolyte. At the metallic mineral−electrolyte interface, ions in the EDL move relative to the metal surface resulting in a diffusive mechanism (σ^*_{mdiff}) that linearly increases with the metallic surface area (*21*, *22*). Second, an electrochemical mechanism (σ^*_{melc}) associated with redox active ions (in this research DO, Fe^{2+}, and Fe^{3+}), allowing electrical currents to bridge between electrolytic (σ_{el}) conduction in the pore fluid and electronic conduction (σ_{elc}) in the metallic grains, occurs (*21*). The measured σ' depends on σ_{el}, σ_{elc}, and σ^*_{int}, whereas σ'' is only dependent on σ^*_{int} (i.e., it exclusively relates to the interfacial properties of the soil).

Here, we examine the sensitivity of $\sigma^*(\omega)$ to precipitation occurring on the Fe^0 surface following corrosion by conducting comparative experiments under controlled dissolved oxygen (DO) conditions. We investigate the iron corrosion process associated with Na_2SO_4 and Na_2CO_3 as sulfate and carbonate are ions in natural groundwater that impact PRBs (*6*, *8*−*10*, *23*). Aqueous geochemical measurements combined with solid-phase analysis of grain surfaces are used to evaluate corrosion and precipitation processes. The results demonstrate the sensitivity of electrical measurements to precipitation on the Fe^0 surface and suggest that the method is a viable technology for monitoring corrosion in PRBs.

Materials and Methods

Column Setup. Our samples were Fe^0−sand mixtures as used in PRBs (*24*) and previous studies (*23*, *25*). The addition of sand to Fe^0 increases porosity and reduces clogging (*23*, *25*). Samples were prepared by mixing 75% Fisher filings (approximately 0.4 mm diameter; density (ρ) = 3.29 g/cm^3, specific surface area (S_s) = 2.84 m^2/g) by volume with 25% Ottawa sand (0.6−0.7 mm diameter, ρ = 1.75 g/cm^3, S_s = 0.05 m^2/g) by volume. This mixture was dry-packed into poly(vinyl chloride) column sample holders (16 cm length × 3 cm i.d.) prepared in as near to an identical manner as possible in terms of packing and composition. However, some differences occurred as modeled electrical parameters for the two columns at the start of the experiment differed by 10%.

10.1021/es051052x CCC: $30.25 © 2005 American Chemical Society
Published on Web 10/28/2005

The solutions in the two columns were (a) 0.01 M Na_2CO_3 sparged with N_2 (1 h per liter of solution) to provide relatively low DO (2.3 ppm), a slow corrosion rate representative of groundwater conditions, and to cause precipitation of carbonate minerals and (b) 0.01 M Na_2SO_4 exposed to air to simulate DO rich (8.8 ppm) conditions, high corrosion rates, and precipitation of iron (oxy)hydroxide. Synthetic groundwater was not manufactured as our intention was to make measurements under simplified geochemical conditions and to evaluate electrical signatures resulting from different solution chemistries and reaction rates.

Electrolyte was pumped into the columns at a volumetric flow rate of 0.3 mL/min, equivalent to a flow rate of 0.61 m/day, 20 pore volumes/day, and a residence time of about 180 min, being relatively short but within a range used elsewhere (*8*, *10*, *26*). Temperature was maintained at 21 ± 0.5 °C. A diagram and a detailed description are available in Supporting Information Figure S1.

Geochemical Monitoring. Geochemical samples were collected to monitor changes in aqueous chemistry. Electrolyte pH, E_h, and conductivity as well as DO and dissolved iron concentrations were measured. Solution pH and E_h were obtained with a Corning 313 pH/temperature meter. Electrolyte conductivity was obtained with an Orion 135A conductivity meter. DO was determined from the Indigo Carmine method (minimum detection limit, MDL = 0.4 ppm) and dissolved iron was determined with the 1,10-phenanthroline titration method (MDL = 0.15 ppm). Measurements were made daily for the first week and then every 2−3 days.

Porosity and Surface Area. Porosity of both unreacted and reacted (end of experiment) Fe^0−sand mixtures was calculated by measuring water content through weight loss (uncertainty of about 1%). A five point Brunauer, Emmett, and Teller (BET) (*27*) method was used to measure S_s for unreacted Fe^0 and Ottawa sand as well as the reacted Fe^0−sand mixture obtained from destructive sampling. Measurements were made in triplicate using a NOVA 3000 analyzer from Quantachrome instruments.

Scanning Electron Microscopy (SEM). Surface and cross-sectional SEM was used to characterize morphological and mineralogical changes to the Fe^0 surface. A LEO 1530 VP field emission scanning electron microscope with an energy-dispersive X-ray (EDX) detector was used for image acquisition and elemental composition analysis. The operating voltage was 10 kV for surface imaging and 25 kV for cross-sectional analysis to enhance image quality. SEM was performed on the reacted Fe^0−sand mixture obtained from destructive sampling as well as on unreacted Fe^0 for comparison. Samples were first dried with a Bal Tec Med020 HR dryer/coater, with an air exposure time below 10 min to minimize alteration of the Fe^0 surface.

Cross-sectional imaging was conducted to study the thickness of surface coatings (both Fe^0 and sand were examined). Five grams of sample mixture proximal to each column inlet were extracted and impregnated into epoxy resin (7:3 resin/hardener ratio by volume) immediately to prevent air oxidation. Samples were then subject to a vacuum oven (60 °C) for 20 h. After curing, samples were polished to acquire a cross-section of the Fe^0 particles. A layer of carbon (several angstroms in thickness) was coated onto the polished surface to facilitate electronic conductivity and inhibit surface glaring.

XRD. Ten grams of sample was extracted proximal to the inlets of both columns within an anaerobic chamber to minimize contamination by air. Samples were washed with a deoxygenated acetone/water mixture (1:1 volume ratio) to eliminate residual solution and dried in the chamber for 4 h. No grinding was done as the particle size was relatively small (0.1−0.4 mm diameter) and preliminary runs showed good data quality and reproducibility. Unreacted iron was similarly prepared and mixed with Ottawa sand (75% Fe^0 by volume) for comparison with reacted columns. Samples were analyzed with a Philips PW3040 powder X-ray diffractometer operated at 45 kV and 40 mA. Scans from $2\theta = 15-85°$ were acquired where θ is the glancing angle between the X-ray beam and the sample surface. A Cu Kα anode was used as radiation source ($\lambda = 1.5406$ Å). The scan rate was 0.02° per step. The analytical software X'pert highscore with a reference database Powder Diffraction File was used for mineral phase identification.

Electrical Data. Electrical measurements (Supporting Information, Figure S1) were conducted with a dynamic signal analyzer (*28*). Inlet and outlet valves were closed to pause flow and minimize pressure differences between inlet and outlet prior to measurements. Current was injected at the stainless steel mesh electrodes, and the sample voltage was recorded using Ag/AgCl electrodes. A preamplifier was used to boost the input impedance to 10^9 Ω to avoid current leakage into the external circuitry. Any residual frequency and sample resistance dependent phase response resulting from circuitry was removed through calibration measurements on pure electrolyte solutions with known $\sigma^*(\omega)$. Repeatability tests indicate that errors were less than 0.5 milrads for the phase and 0.5% for conductivity magnitude, respectively (*28*). Electrical measurements were conducted daily for the first 5 days and then every 2−3 days. The phase shift (ϕ) and conductivity magnitude ($|\sigma|$) for the sample were determined relative to a reference resistor (Supporting Information, Figure S1) for 40 frequencies spaced at equal logarithmic intervals from 0.1 to 1000 Hz. The real and imaginary parts of the complex conductivity were determined as

$$\sigma'' = |\sigma| \sin \phi \tag{2}$$

$$\sigma' = |\sigma| \cos \phi \tag{3}$$

Electrical Modeling. Physically based models to describe the $\sigma^*(\omega)$ of soils are lacking, and macroscopic representations, such as the Cole−Cole model (*29*), are typically adopted (see for review, ref *18*). The dependence of complex conductivity with frequency was modeled as in ref *30*.

$$\sigma^* = \sigma_0\left[1 + m\left(\frac{(i\omega\tau)^c}{1 + (i\omega\tau)^c(1 - m)}\right)\right] \tag{4}$$

where σ_0 is the conductivity at DC frequency, τ is the mean relaxation time, c is a shape exponent (typically 0.1−0.6), and m is the chargeability ($m = 1 - \sigma_0 / \sigma_\infty$, where σ_∞ is the conductivity at high frequency). The two model parameters of interest here are σ_0 and $m_n = m\sigma_0$, representing global measures of conduction and interfacial polarization, respectively (*31*). We inverted electrical data using an algorithm based on a least-squares approach with Marquardt regularization (*32*).

Results and Discussion

Fluid Geochemistry. Figure 1 shows the aqueous geochemistry results for both columns.

Aside from early-stage variations, effluent chemistry was relatively stable for both columns. Influent chemistry is summarized in Supporting Information Table S1. Influent conductivity of the sulfate column was 0.217 S/m, and effluent conductivity started at 0.218 S/m, exhibiting a maximum of 1.8% change. The pH in the sulfate column initially changed from 6.7 at the influent to around 10 at the effluent (Figure 1A), being attributed to aerobic corrosion of Fe^0 and release of OH^- (*6*). Fe^0 would be oxided to Fe^{2+} (limited DO condition) or Fe^{3+} (high DO condition).

The influent DO in the sulfate column was about 8.8 ppm, and DO dropped to around 2 ppm after passing through the

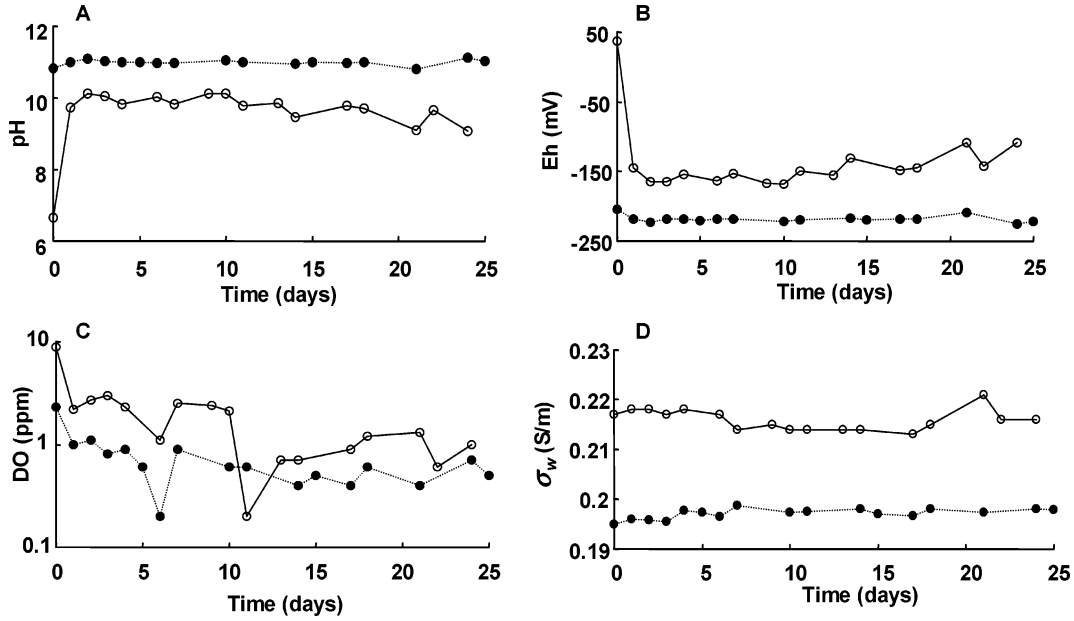

FIGURE 1. Na_2SO_4 (○) and Na_2CO_3 (●) column effluent chemistry with influent chemistry plotted at day 0: (A) pH, (B) E_h, (C) dissolved oxygen (DO) (plotted on logarithmic scale), and (D) electrolyte conductivity (σ_w) as a function of time.

column (Figure 1C), indicating participation of DO in the corrosion and precipitation process. The sulfate column had a positive input E_h (about 40 mV), but it dropped to −150 mV after passing through the column (Figure 1B). According to pH−E_h diagrams (*7*, *10*), the high DO concentration and high influent E_h probably promoted production of Fe^{3+} at the column inlet. Iron oxidation at the inlet reduced DO and increased pH, such that Fe^{2+} was probably dominant further into the column.

The influent conductivity of the carbonate column was 0.195 S/m. Effluent conductivity started at 0.188 S/m with a 2.1% change (Figure 1D). Solution pH for the carbonate column was high (10.8) at the influent; although of limited environmental relevance, we did not buffer the pH (buffering to pH 7 would have increased reaction rates). Solution pH alone exerts a negligible effect on electrical properties of Fe^0 (*22*). Effluent pH remained high (initially increasing) during the experiment (Figure 1A). Corrosion of Fe^0 did not exert a significant effect on pH because of the initially high input pH and the low reaction rate in this column. DO in the influent of the carbonate column was 2.3 ppm, and it dropped to below 1 ppm in the effluent (Figure 1C). The E_h changed from −200 mV at the influent to about −220 mV at the effluent (Figure 1B), indicating a near constant reductive environment. Given these pH−E_h ranges and measurable DO, significant hydrogen gas generation was unlikely in either column (*10*, *33*).

Porosity and Surface Area. Porosity of the unreacted Fe^0−sand mixture was 38.1% (Table S1). Values for reacted samples from the sulfate and carbonate columns were 36.1 and 37.3%, respectively. Porosity losses (2% for sulfate column and 0.8% for carbonate column) were close to the uncertainty of the measurement (about 1%) (i.e., significant porosity losses did not occur). The S_s of the Ottawa sand and unreacted iron filings was determined from nitrogen adsorption to be 0.05 ± 0.002 m^2/g and 2.8 ± 0.08 m^2/g (Table S1), respectively. The S_s of the unreacted iron−sand mixture was measured as 2.35 ± 0.07 m^2/g, being within the error of the calculated value of this mixture (2.42 ± 0.07 m^2/g) based on the values of S_s and ρ of the constituents. The S_s of samples extracted from the columns upon experiment completion was 3.04 ± 0.09 m^2/g for the sulfate column and 2.58 ± 0.08 m^2/g for the carbonate column. The S_s of reacted iron from both columns was back-calculated from the measured S_s of the mixture assuming constant S_s and ρ for the sand and constant ρ for iron. We assume that the precipitation caused a much greater change in S_s than in ρ such that this assumption does not impact the calculation. Calculated S_s of the iron after the experiment was 3.57 ± 0.11 m^2/g for the sulfate column and 3.03 ± 0.09 m^2/g for the carbonate column.

SEM/EDX. SEM imaging of samples at the end of the experiment revealed an unaltered sand surface, although some attachment of small mineral clusters to the sand was observed. Changes in surface morphology were observed for reacted Fe^0 particles as shown in Figure 2.

Compared with unreacted iron (Figure 2A), the DO-rich sulfate column exhibits a strong change of surface morphology (Figure 2C): instead of amorphous fine particles on an unreacted surface, the sulfate impacted Fe^0 surface is covered by a mixture of amorphous and platelet shaped minerals. EDX analysis revealed the main elements to be Fe and O. Sulfur was not detected. Cross-sectional imaging (Figure 2B,D) further revealed differences in surface morphology. The unreacted Fe^0 has a clean edge, whereas samples from the sulfate column (Figure 2D) revealed corrosion rinds for the Fe^0 particles with a thickness of 20 μm or more.

The DO-poor carbonate column samples (Figure 2E) do not show significant changes of surface morphology, but EDX analysis reveals a significant amount of carbon (16.4 atomic %) on the surface as well as Fe and O, indicating iron carbonate phases. Cross-sectional imaging of samples from this column (Figure 2F) also exhibit corrosion rinds, although the thickness is less than 20 μm and only a portion of the grains imaged show a rind. The SEM imaging thus reveals corrosion and precipitation reactions, being greater in the DO-rich sulfate column than in DO-poor carbonate column.

XRD Analysis. XRD analysis of the unreacted mixture (Figure 3A) revealed mineral phases other than quartz to be Fe^0, magnetite (Fe_3O_4)/hematite (α-Fe_2O_3), and maghemite (γ-Fe_2O_3), among which hematite, maghemite, and magnetite are difficult to separate as they share close peaks. Quartz was identified as a major phase for all three samples due to the sand. The higher (about 0.05 2θ°) and narrower quartz peaks reflect the larger size of the sand as compared to the iron minerals, having lower, broader peaks (about 0.4−1.7 2θ°)

XRD analysis for the sulfate column is shown in Figure 3C. Maghemite and hematite exist at reduced peak intensity,

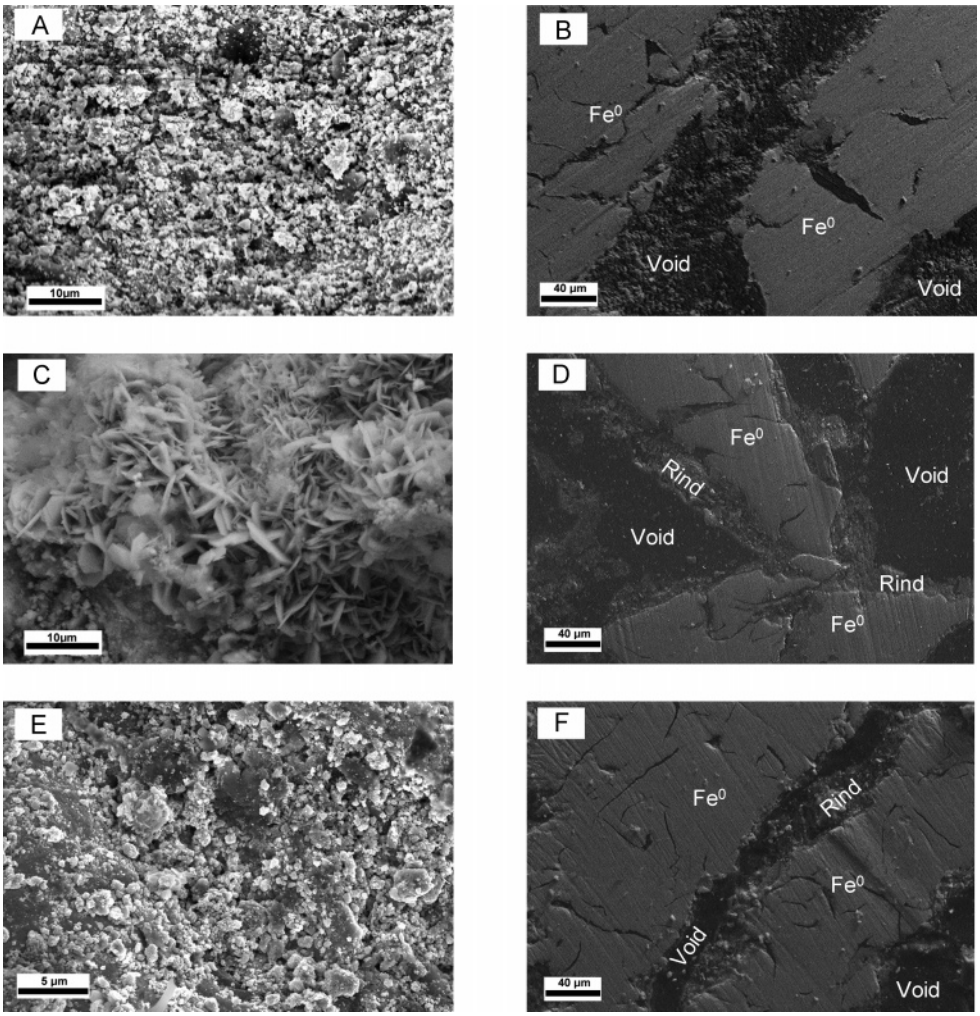

FIGURE 2. SEM images of (A) part of an unreacted Fe^0 particle surface; (B) unreacted Fe^0 cross-section; (C) part of a sulfate treated Fe^0 particle surface; (D) sulfate treated Fe^0 cross-section; (E) part of a carbonate treated Fe^0 particle surface; and (F) carbonate treated Fe^0 cross-section. Sulfate and carbonate treated Fe^0 particles were from the columns after 25 days.

and goethite (α-FeOOH) and akaganeite (*β*-FeOOH) are identified as new phases. No sulfate or sulfide minerals are identified. Hexagonal platelet shaped minerals were identified in SEM imaging (Figure 2C, possibly indicative of green rust (a mineral phase of mixed $Fe^{2+}/Fe3^{+}$ oxy(hydroxide) layers with anions (i.e., Cl^-, CO_3^{2-}, SO_4^{2-}) incorporated into inner-layer spaces (*34*)). However, XRD did not show characteristic peaks of green rust, possibly reflecting a limited concentration and sparse distribution.

Orange stains observed at the inlet verified the existence of ferric (oxy)hydroxide as corrosion products neared the inlet. As DO was depleted at the inlet, the redox condition became more reductive further into the column, and Fe^0 was likely oxidized to the +2 state facilitating the formation of magnetite. Moreover, hematite and maghemite are transformed by an autoreduction reaction, whereby water and electrons from the iron participate in the reduction of these phases (*35*). Blackening of the column was observed to expand from beyond the inlet toward column ends, indicating precipitation of magnetite. Direct conversion from hematite/maghemite to magnetite without dissolution and precipitation of Fe^{2+} is also suggested by Haruyama et al. (*36*). No sulfide minerals were detected as expected given the geochemical environment.

XRD analysis for the carbonate column (Figure 3B) suggests reduced amounts of magnetite and hematite (and possibly maghemite) and the appearance of siderite ($FeCO_3$). Hematite and maghemite are transformed by autoreduction reactions. However, our results suggest siderite as the major phase rather than magnetite, probably reflecting the high concentration of carbonate and the insolubility of iron carbonate ($FeCO_3$, solubility $= 3.07 \times 10^{-11}$). Within the pH−E_h range of this column (pH about 10−11, E_h about −240mV), precipitation of siderite was expected (*7*, *10*). Dissolved iron that precipitates out as siderite is not only from autoreduction of hematite/maghemite but also from corrosion of Fe^0. Compared to the unreacted Fe^0, results from the carbonate column exhibit reduced magnetite/hematite/maghemite peaks, suggesting reduced amounts of each.

XRD measurements also revealed decreases in the peaks for Fe^0 after the experiment. The unreacted Fe^0 sample has the highest peak at all characteristic 2θ values ($2\theta = 44.8$, 65.1, and 82.5°), representing the highest Fe^0 concentration of the three samples; the low DO carbonate column exhibits medium peaks, whereas the high DO sulfate column shows the lowest peaks. These observations confirm the occurrence of corrosion of Fe^0 in both columns and faster rates in the sulfate column (primarily due to high DO). Finally, the broader peaks in the mineral phases identified in the sulfate column suggest the precipitation of finer precipitates (consistent with the higher S_s recorded for the sulfate column).

Complex Conductivity. Figure 4 shows the σ'' and σ' changes as a function of frequency and time for both columns.

There is a continuous increase of σ'' in both columns during the first 5 days of the experiment. The σ'' then remained at elevated levels achieved on day 5 until the end

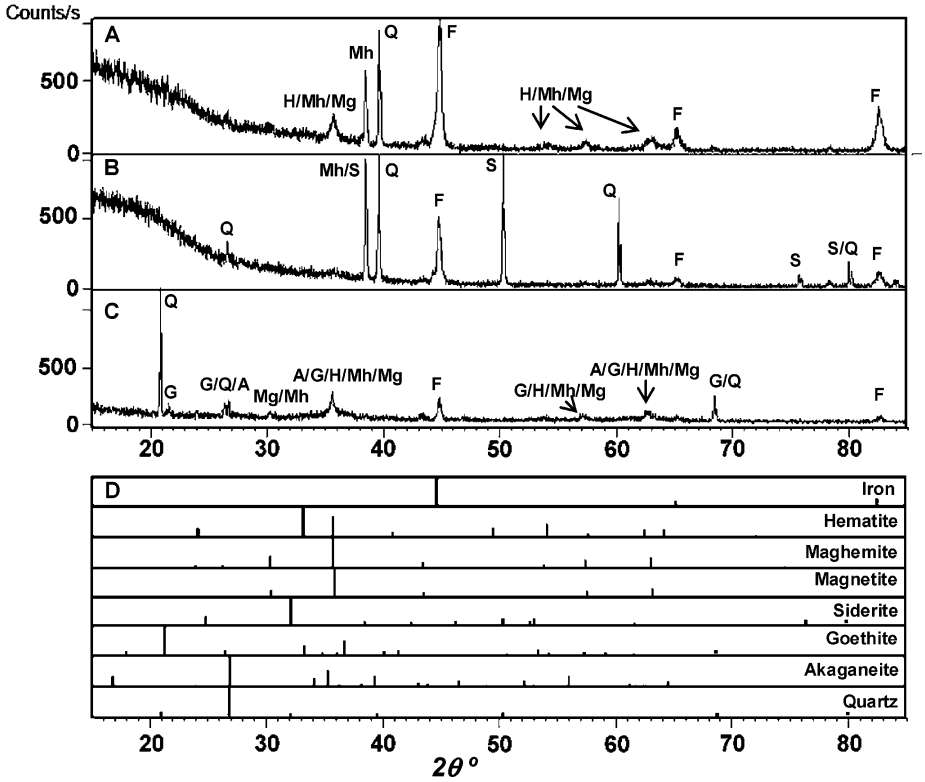

FIGURE 3. X-ray diffractograms of (A) unreacted Fe^0 with 25 vol % mixed Ottawa sand; (B) carbonate treated Fe^0−sand mixture; (C) sulfate treated Fe^0−sand mixture; and (D) indexing peaks of selected phases (H, hematite; Mh, maghemite; Mg, magnetite; S, siderite; G, goethite; A, akaganeite; F, Fe^0; and Q, quartz).

of the experiment. We attribute the constant conditions after day 5 to the extension of the reaction front beyond the support volume of the electrical measurement (volume between the two potential electrodes) as the consistently high pH, coupled with the continuously falling DO after day 5 (Figure 1), verifies that reactions continued in both columns. Figure 4C,D also reveals consistent changes in σ' for both columns: it increased during the first 4−5 days (except between 0.1 and 1 Hz from day 0 to day 1 in the sulfate column) and then remainined elevated and near constant. Supporting Information Figure S3 is an example of the fit of $\sigma^*(\omega)$ to the Cole−Cole model. All datasets were found to fit the model well.

Figure 5 shows the variation in the model parameters (m_n and σ_0) throughout the experiment. The different starting model parameters on day 0 (10% variation) likely reflect differences in column packing as previously discussed. The modeling is consistent with the behavior inferred from Figure 4: model parameters increase steadily for the first 5−6 days, changing minimally thereafter. Small fluctuations in both m_n and σ_0 occur between days 5 and 15 in the sulfate column. Figure 5 reveals an overall 35.4% increase of m_n for the sulfate column (Figure 5A) and a 22.5% increase for the carbonate column (Figure 5B). We attribute this increase to strengthening of EDL polarization at the iron mineral−fluid interface. The sulfate column (high DO level) shows greater changes, suggesting a greater increase of EDL polarization.

The DC conductivity (σ_0) exhibits similar behavior, showing an increase of 45.4% for the sulfate column (Figure 5A) and 24.9% for the carbonate column (Figure 5B). Temperature and σ_w (Figure 1D) were approximately constant throughout the experiment, and porosities were constant or decreased slightly. Enhanced electrolytic conductivity through the interconnected pore space (σ_{el}) is therefore not a significant contributing factor to the increases in m_n and σ_0. Although porosity loss may enhance pore throat tortuosity and possibly generate membrane polarization at pore entrances, the small changes in porosity indicate that this mechanism is unlikely. Thus, the electrical response of the system is due to the mineral surface alteration associated with the corrosion and precipitation processes and subsequent enhancement of electronic conduction.

The electrical responses are consistent with the aqueous and solid-phase analyses. Enhanced conduction and interfacial polarization is supported by the observed modification of the surface morphology and mineral phase. The altered surface morphology and thick corrosion rind observed represent the cumulative result of surface alteration during the experiment. The sulfate column (high DO) exhibits the largest surface alteration and the largest change in $\sigma^*(\omega)$. The small fluctuations in the electrical parameters observed between days 5 and 15 in the sulfate column (Figure 5A) are not reflected in the aqueous geochemistry and therefore probably reflect mineralogical changes that were not captured with our solid-phase analyses.

Previous research suggests that the interfacial polarization is linearly related to the S_s of metallic particles, is independent of pH, and displays a power law relation to electrolyte activity (*22*). We suggest that the increased polarization in part results from an increase in S_s of the metallic mineral−electrolyte interface resulting from the precipitation process. A larger S_s provides more contact between ions in solution and iron surface, facilitating more charge accumulation and polarization. BET measurements confirmed this increased S_s of iron materials (Fe^0 corrosion products) that we attribute to minerals coating the Fe^0 surface. The higher reactivity of the sulfate column, primarily due to higher DO, is consistent with a greater increase in S_s, and hence polarization terms (m_n, σ''), resulting from more extensive surface alteration. Both surface and cross-sectional SEM imaging of Fe^0 particles from the sulfate column (Figure 2C,D) support an increased S_s due to precipitation; cross-sectional imaging of the carbonate column also revealed a surface rind even though surface alteration was not obvious from the surface imaging. Finally, the XRD data also suggest the precipitation of fine

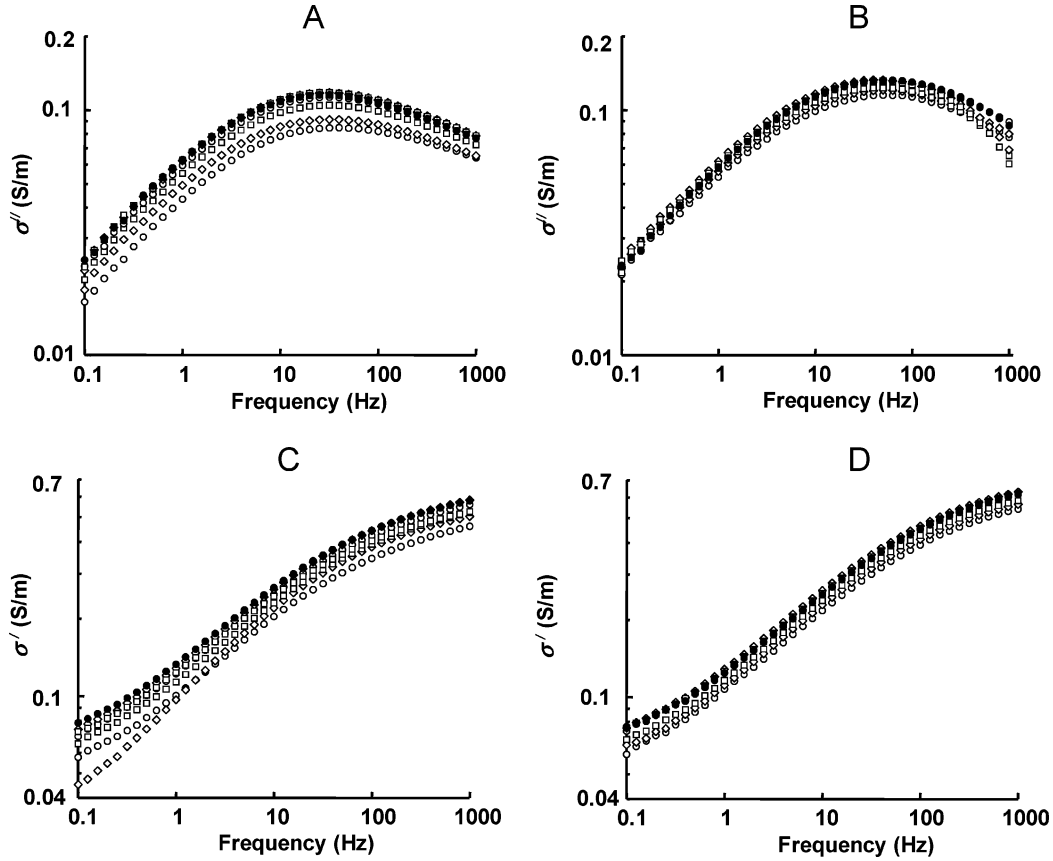

FIGURE 4. Spectral electrical data on selected days (for Na_2SO_4 column: 0 (open circle), 1 (open diamond), 3 (open square), 4 (gray circle), 5 (gray diamond), 17 (gray square), and 25 (black circle) days; for Na_2CO_3 column: 0 (open circle), 1 (open diamond), 3 (open square), 10 (gray circle), 14 (gray diamond), 18 (gray square), and 21 (black circle) days). (A) Imaginary part of complex conductivity (σ'') of Na_2SO_4 column; (B) σ'' of Na_2CO_3 column; (C) real part of complex conductivity (σ') of Na_2SO_4 column; and (D) σ' of Na_2CO_3 column. Data are plotted on a logarithmic scale.

(high S_s) particles: the sulfate column exhibits broad peaks indicative of finely particulate minerals following oxidation. We note that the magnitude of the S_s increase of iron minerals (27%) in the sulfate column is close to the increase of m_n (35.4%) in this column, although the values are less similar for the carbonate column. Hence, other factors, notably precipitate mineralogy, impact the electrical response but cannot be fully evaluated here.

The increased electrical conduction results from two mechanisms: first, the increase of metallic mineral–electrolyte surface area increases the real part of the interfacial conductivity (σ^*_{int}) due to larger contact between ions in solution and the iron as described previously. The mechanism is analagous to the reduction in charge transfer resistance associated with nanoporous precipitation of oxide phases that increase the surface area described elsewhere (*15*). Second, the newly precipitated and transformed electroactive mineral phases (i.e., magnetite, which is electronically conductive and redox active (serve as a reductant) (*37*)) enhanced electronic conduction. EIS results confirm that the formation of secondary oxide phases appears to mediate electron transfer from the Fe^0 surface to oxidants in solution (*13*). Both the electroactive mineral phases and the increased surface area reduces the charge-transfer resistance across metallic mineral/electrolyte interfaces and results in improved interfacial and electron conduction (*13*, *15*). The effect is greater in the sulfate column as magnetite is a major corrosion product and the surface area increase is larger relative to the carbonate column. Although porosity loss caused by infilling of the pore space was small, interlinking of adjacent iron particles due to pore space reduction may also have occurred.

EIS and Tafel analysis has revealed electrochemical kinetics of iron corrosion under controlled fluid chemistry (*13*, *15*, *38*) and aid understanding of the electrical measurements presented here. However, EIS is a microscale method that cannot be readily applied to study corrosion and precipitation in installed barriers. The electrical method used here is an upscaled method that measures electrochemical properties of bulk PRB material, providing a linkage between laboratory electrochemical research and practical field studies. Our experiment suggests that complex conductivity measurements are indeed diagnostic of metal surface precipitation occurring in granular Fe^0. The technique is noninvasive as measurements are made on a bulk soil mixture. The correlation between electrical data and surface alteration determined from the destructive surface phase analyses suggests that the electrical measurements are a proxy indicator of Fe^0 surface alteration.

Research on PRB installations shows more intensive precipitation, coupled with greater porosity and surface area changes, relative to observations from our synthetic columns (*7*, *26*, *39*). The longer reaction times and more complex aqueous geochemistry associated with field-installed PRBs facilitate more mineralogical changes than observed here. We therefore expect greater changes in the electrical parameters measured over long-term monitoring of a PRB than described here. This has been confirmed by measurements on cores recovered from a PRB in Kansas City after 8 years of operation, showing large electrical changes in the reacted zone. Hence, the technique may provide a noninvasive way to monitor long-term performance of PRB installations.

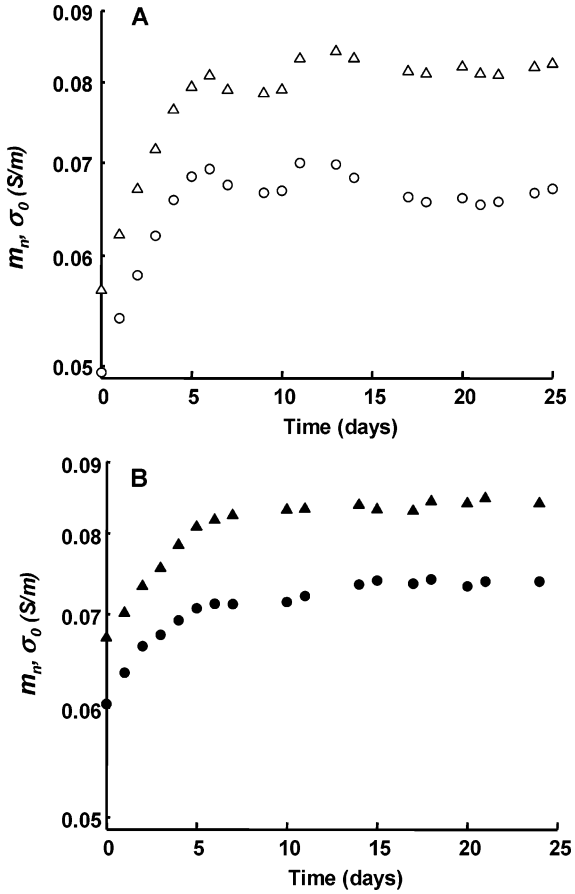

FIGURE 5. Cole−Cole model parameters polarization (m_n) (○ , ●) and conduction (σ_0) (△, ▲) as a function of time over the 25 day experiment duration: (A) Na_2SO_4 column and (B) Na_2CO_3 column. The plot has a logarithmic *y*-axis and linear *x*-axis.

Acknowledgments

This research was supported by the Environmental Management Science Program (EMSP) of the Office of Science, U.S. Department of Energy, Grant DE-FG07-02ER63506. Andreas Kemna (Institute of Chemistry and Dynamics of the Geosphere, Forschungszentrum Jülich) provided Cole−Cole relaxation modeling support. We thank three reviewers and the associate editor for constructive comments that improve this paper.

Supporting Information Available

Schematic of the experimental setup; figure containing additional cross-sectional SEM images from both columns; illustration of the Cole−Cole model fit to the electrical data; table of geochemical parameters of influent solutions. This material is available free of charge via the Internet at http://pubs.acs.org.

Literature Cited

(1) Agrawal, A.; Ferguson, W. J.; Gardner, B. O.; Christ, J. A.; Bandstra, J. Z.; Tratnyek, P. G. Effects of carbonate species on the kinetics of dechlorination of 1,1,1-trichloroethane by zerovalent iron. *Environ. Sci. Technol.* **2002**, *36*, 4326−4333.

(2) Gillham, R. W.; Ohannesin, S. F. Enhanced Degradation of Halogenated Aliphatics by Zerovalent Iron. *Groundwater* **1994**, *32*, 958−967.

(3) Gu, B.; Liang, L.; Dickey, M. J.; Yin, X.; Dai, S. Reductive precipitation of uranium(VI) by zerovalent iron. *Environ. Sci. Technol.* **1998**, *32*, 3366−3373.

(4) Su, C. M.; Puls, R. W. Arsenate and arsenite removal by zerovalent iron: Kinetics, redox transformation, and implications for in situ groundwater remediation. *Environ. Sci. Technol.* **2001**, *35*, 1487−1492.

(5) Vogan, J. L.; Focht, R. M.; Clark, D. K.; Graham, S. L. Performance evaluation of a permeable reactive barrier for remediation of dissolved chlorinated solvents in groundwater. *J. Hazard. Mater.* **1999**, *68*, 97−108.

(6) Furukawa, Y.; Kim, J. W.; Watkins, J.; Wilkin, R. T. Formation of ferrihydrite and associated iron corrosion products in permeable reactive barriers of zerovalent iron. *Environ. Sci. Technol.* **2002**, *36*, 5469−5475.

(7) Liang, L. Y.; Korte, N.; Gu, B. H.; Puls, R.; Reeter, C. Geochemical and microbial reactions affecting the long-term performance of in situ iron barriers. *Adv. Environ. Res.* **2000**, *4*, 273−286.

(8) Liang, L. Y.; Sullivan, A. B.; West, O. R.; Moline, G. R.; Kamolpornwijit, W. Predicting the precipitation of mineral phases in permeable reactive barriers. *Environ. Eng. Sci.* **2003**, *20*, 635−653.

(9) Phillips, D. H.; Gu, B.; Watson, D. B.; Roh, Y.; Liang, L.; Lee, S. Y. Performance evaluation of a zerovalent iron reactive barrier: Mineralogical characteristics. *Environ. Sci. Technol.* **2000**, *34*, 4169−4176.

(10) Gu, B.; Phelps, T. J.; Liang, L.; Dickey, M. J.; Roh, Y.; Kinsall, B. L.; Palumbo, A. V.; Jacobs, G. K. Biogeochemical dynamics in zerovalent iron columns: Implications for permeable reactive barriers. *Environ. Sci. Technol.* **1999**, *33*, 2170−2177.

(11) Kohn, T.; Livi, K. J.; Roberts, A. L.; Vikesland, P. J. Longevity of granular iron in groundwater Treatment Processes: Corrosion product development. *Environ. Sci. Technol.* **2005**, *39*, 2867−2879.

(12) Ritter, K.; Odziemkowski, M. S.; Gillham, R. W. An in situ study of the role of surface films on granular iron in the permeable iron wall technology. *J. Contam. Hydrol.* **2002**, *55*, 87−111.

(13) Melitas, N.; Farrell, J. Understanding chromate reaction kinetics with corroding iron media using Tafel analysis and electrochemical impedance spectroscopy. *Environ. Sci. Technol.* **2002**, *36*, 5476−5482.

(14) Melitas, N.; Conklin, M.; Farrell, J. Understanding the mechanisms controlling the kinetics of arsenate and chromate removal from solution using zerovalent iron. *ACS Symp. Ser.* **2003**, *837*, 165−180.

(15) Mishra, D.; Farrell, J. Understanding nitrate reactions with zerovalent iron using tafel analysis and electrochemical impedance spectroscopy. *Environ. Sci. Technol.* **2005**, *39*, 645−650.

(16) Slater, L.; Binley, A. Evaluation of permeable reactive barrier (PRB) integrity using electrical imaging methods. *Geophysics* **2003**, *68*, 911−921.

(17) Schon, J. H. *The physical properties of Rocks: Fundamentals and principles of petrophysics*; Elsevier: Amsterdam, 1996.

(18) Dias, C. Developments in a model to describe low-frequency electrical polarization in rocks. *Geophysics* **2000**, *65*, 437−451.

(19) Pelton. W. H.; Sill, W. R.; Smith, B. D. Interpretation of complex resistivity and dielectric data. Part 1. *Geophys. Trans.* **1978**, *29*, 297−330.

(20) Archie, G. E. The electrical resistivity log as an aid in detemining some reservoir characteristics: Transactions of the American Institute of Minerals. *Metall. Petrol. Eng.* **1942**, *146*, 54−62.

(21) Wong, J. An electrochemical model of the induced-polarization phenomenon in disseminated sulfide ores. *Geophysics* **1979**, *44*, 1245−1265.

(22) Slater, L. D.; Choi, J.; Wu, Y. Electrical properties of iron-sand columns: Implications for induced polarization investigation and performance monitoring of iron-wall barriers. *Geophysics* **2005**, *70*, G87−G94.

(23) Mackenzie, P. D.; Horney, D. P.; Sivavec, T. M. Mineral precipitation and porosity losses in granular iron columns. *J. Hazard. Mater.* **1999**, *68*, 1−17.

(24) O'Hannesin, S. F.; Gillham, R. W. Long-term performance of an in situ iron wall for remediation of VOCs. *Ground Water* **1998**, *36*, 164−170.

(25) Kaplan, D. I.; Gilmore, T. J. Zerovalent iron removal rates of aqueous Cr(VI) measured under flow conditions. *Water, Air, Soil Pollut.* **2004**, *155*, 21−33.

(26) Kamolpornwijit, W.; Liang, L.; West, O. R.; Moline, G. R.; Sullivan, A. B. Preferential flow path development and its influence on long-term PRB performance: column study. *J. Contam. Hydrol.* **2003**, *66*, 161−178.

(27) Brunauer, S.; Emmett, P. H.; Teller, E. Adsorption of gases in multimolecular layers. *J. Am. Chem. Soc.* **1938**, *60*, 309−319.

(28) Slater, L.; Lesmes, D. P. Electrical−hydraulic relationships observed for unconsolidated sediments. *Water Resour. Res.* **2002**, *38*.

(29) Pelton, W. H.; Sill, W. R.; Smith, B. D. Interpretation of complex resistivity and dielectric data. Part I. *Geophys. Trans.* **1978**, *29*, 297−330.
(30) Jones, D. P. Master's Thesis, Department of Geophysics, Colorado School of Mines, 2002; p 403.
(31) Lesmes, D. P.; Frye, K. M. Influence of pore fluid chemistry on the complex conductivity and induced polarization responses of Berea sandstone. *J. Geophys. Res.* **2001**, *106*, 4079−4090.
(32) Kemna, A. *Tomographic inversion of complex resistivity—theory and application*; Der Andere Verlag: Osnabrück, Germany, 2000.
(33) Zhang, Y.; Gillham, R. W. Effects of gas generation and precipitates on performance of Fe PRBs. *Ground Water* **2005**, *43*, 113−121.
(34) Legrand, L.; Savoye, S.; Chausse, A.; Messina, R. Study of oxidation products formed on iron in solutions containing bicarbonate/carbonate. *Electrochim. Acta* **2000**, *46*, 111−117.
(35) Pryors, M. J.; Evans, U. R. Chemical communication. *J. Am. Chem. Soc.* **1950**, 1259.
(36) Haruyama, S.; Ogura, K.; Nagasaki, K. Potential decay of passivated iron in neutral solutions. *J. Electrochem. Soc. Jpn.* **1969**, *37*, 38−44.
(37) Simard, S.; Odziemkowski, M.; Irish, D. E.; Brossard, L.; Menard, H. 191st Meeting of the Electrochemical Society: Montreal, Quebec, 1997; Vol. 97, pp 279−280.
(38) Melitas, N.; Chuffe-Moscoso, O.; Farrell, J. Kinetics of soluble chromium removal from contaminated water by zerovalent iron media: Corrosion inhibition and passive oxide effects. *Environ. Sci. Technol.* **2001**, *35*, 3948−3953.
(39) Wilkin, R. T.; Puls, R. W.; Sewell, G. W. Long-term performance of permeable reactive barriers using zerovalent iron: Geochemical and microbiological effects. *Ground Water* **2003**, *41*, 493−503.

Received for review June 4, 2005. Revised manuscript received September 26, 2005. Accepted September 26, 2005.

ES051052X

Supporting Information

Effect of Precipitation on Low Frequency Electrical Properties of Zero Valent Iron Columns

Yuxin Wu, Lee D Slater, Nic Korte

Pages: 5
Contents: 3 figures (S1-S3)
1 table (S1)

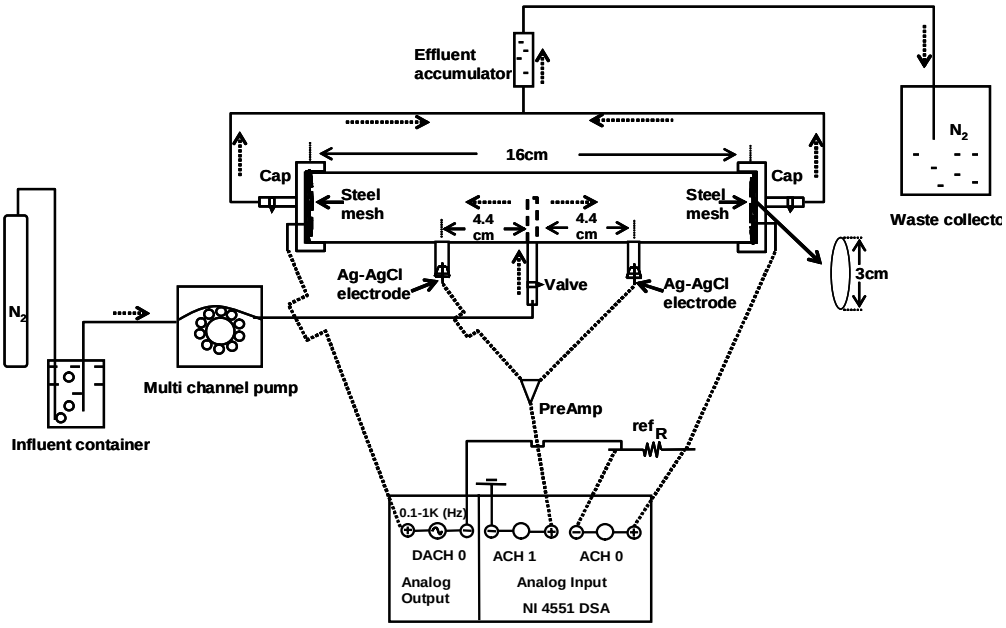

Figure S1. Experimental design of column flow-through and electrical measurement system. N_2 gas flow was only for Na_2CO_3 column. Influent container of Na_2SO_4 column was open to the atmosphere. Sample holder was packed with 75% Fe^0-25% Ottawa sand by volume mixture.

Brief description: Sample holders were equipped with a fluid inlet located at the middle of the column, and effluent outlets at either end. This design was used to promote precipitation towards the column center and in the support volume of the electrical measurement. Plastic valves were used to control the flow. A stainless steel mesh was installed at either column end to introduce an external current field. Two ports were installed on the edge of the sample spaced 4.4 cm either side of the inlet to house Ag/AgCl electrodes for measuring the voltage waveform across the sample. Sample holders were oriented horizontally to ensure parallel flow toward both outlets. The influent container for the Na_2CO_3 column was sealed air tight and continuously supplied with N_2 (5 psi) to avoid vacuum of head space and the fluid circuit was flushed with N_2 for 10 minutes to eliminate air from the tubing prior to the experiment. The collapsible bag used to collect effluent was also initially filled with N_2 to reduce possible access of O_2 through the end of the pipe. Effluent accumulators were used on both columns to collect effluent samples for geochemical analysis.

(a)

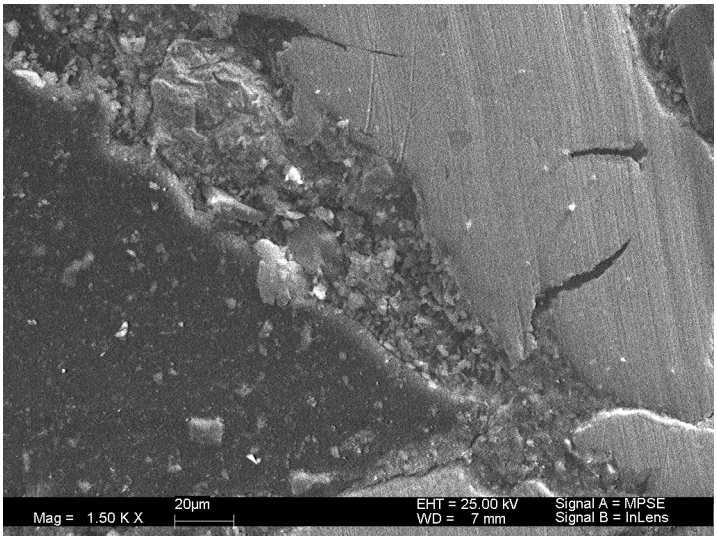

(b)

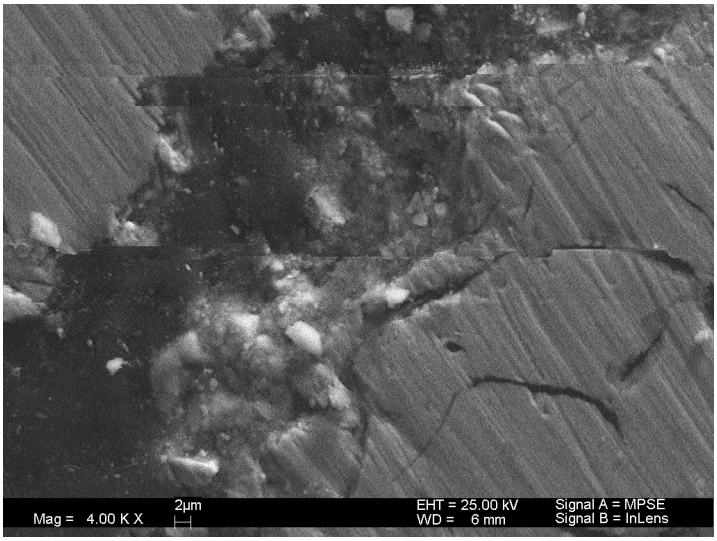

Figure S2. SEM images of (a) Sulfate treated Fe^0 cross section; (b) carbonate treated Fe^0 cross section. Both sulfate and carbonate treated Fe^0 particles were from the columns after 25 days (end of experiment).

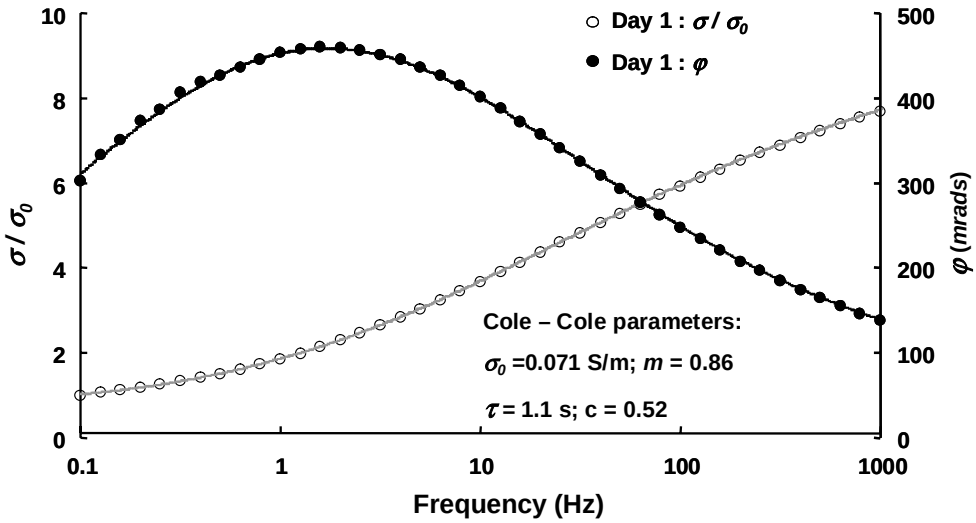

Figure S3. Illustration of the Cole-Cole model fit to the electrical data for day 1 of the carbonate column. Model fitting parameters are also shown.

Table S1. Influent solution chemistry and unreacted iron column properties

	Parameters	Sulfate Column	Carbonate Column
Influent Solutions	$\square_w$ (S/m)	0.217	0.195
	Major species	SO_4^{2-},H_2O, O_2	CO_3^{2-}, H_2O, OH^-, O_2
	pH	6.7	10.8
	Eh (mV)	37	-225
	DO (ppm)	8.8	2.3
Column	Porosity	38.10%	38.10%
	Fe^0 S_s (m^2/g)	2.8	2.8
	Sand S_s (m^2/g)	0.05	0.05

APPENDIX 3

Wu, Y, Slater, L. and Korte, N., Low frequency electrical properties of corroded iron barrier cores, **Environmental Science & Technology**, Submitted 10/20/05.

Low Frequency Electrical Properties of Corroded Iron Barrier Cores

Yuxin Wu[1], Lee D Slater[1], Nic Korte[2]*

[1]Department of Earth and Environmental Sciences, Rutgers University, Newark, NJ 07102

[2]1946 Clover Court, Grand Junction, Colorado 81506

[*]Corresponding author email: yuxinwu@pegasus.rutgers.edu; Phone: (973) 596-5863

Coauthor emails: Lee Slater, lslater@andromeda.rutgers.edu; Nic korte, nkorte1@hotmail.com

We investigated the electrical signatures of iron corrosion and mineral precipitation in angle cores from a Fe^0 barrier installation in operation for eight years. The real and imaginary parts of the complex electrical conductivity measured between 0.1-1000 Hz were 2-10 times higher (varying between cores) in the reacted zone at the upgradient edge of the barrier relative to less altered locations inside the barrier. Scanning electron microscopy (SEM) identified iron surface alteration with thickest corrosion rinds closest to the upgradient soil/iron interface. Surface area (S_s) of iron minerals was also greatest at the upgradient interface, gradually decreasing into the cores. X-ray diffractometry (XRD) identified precipitation of iron oxide/hydroxide, carbonate minerals, iron sulfide as well as green rusts, with mineral complexity decreasing away from the interface. The electrical measurements correlate very well with the solid phase analyses and verify that electrical methods could be used to assess or monitor iron corrosion and mineral precipitation occurring in Fe^0 barriers.

Introduction

Permeable reactive barriers (PRBs) composed of granular zero valent iron (Fe^0) are an established technology for groundwater remediation (1-7). Iron corrosion and mineral precipitation due to reactions between Fe^0 and groundwater constituents are widely recognized as the primary causes of Fe^0 barrier performance reduction (8-15). Corrosion and precipitation may result in formation of iron minerals that are less reactive with groundwater contaminants (8,16,17) and may also clog pore spaces (8,10), thus reducing hydraulic efficiency (3,8,18).

Corrosion and precipitation is typically investigated by aqueous geochemical or solid phase analysis. Electrical methods can be used to indirectly assess iron corrosion and mineral precipitation processes. Tafel scan and electrochemical impedance spectroscopy (EIS) analysis of iron has identified geochemical controls on Fe^0 redox reactions (19-21). A recent study illustrated the sensitivity of four electrode electrical measurements (essentially an upscaled version of an EIS measurement) to corrosion and precipitation processes occurring in columns of granular Fe^0 as a result of invasion with simple electrolytes (22). This work illustrated the possibility of non-invasively monitoring precipitation in PRBs using electrical geophysical methods. Monitoring could be achieved by inserting electrode strings in the barrier during construction and recording the electrical changes as a function of time. This would conceivably reduce monitoring costs by eliminating the need for coring and solid phase analysis or installation of monitoring wells for geochemical analysis

The electrical properties of a soil can be stated in terms of a measured frequency (ω) dependent complex conductivity $\sigma^*(\omega)$,

$$\sigma^*(\omega) = \sigma^{/}(\omega) + i\sigma^{//}(\omega) \tag{1}$$

where σ' is the measured real part of $\sigma^*(\omega)$, being the conduction component, and σ'' is the measured imaginary part of $\sigma^*(\omega)$, being the polarization component ($i = \sqrt{-1}$). Charge transfer in granular Fe^0 columns can be attributed to three mechanisms (22). First, σ_{el} represents the

conductivity of the interconnected, fluid-filled pore space (a real term); second, σ^*_{int} is a complex term describing conduction and polarization at the iron mineral/electrolyte interfaces; third, σ_{elc} accounts for electronic conduction (a real term) through the iron minerals. The σ_{el} is linearly dependent on the conductivity (σ_w) of the electrolyte saturating the Fe^0 column. The σ^*_{int} incorporates both conduction along the electrical double layer (EDL) and polarization occurring at the electrolyte/iron mineral interface. It includes a diffusive mechanism (σ^*_{mdiff}) that linearly increases with the metallic surface area (23,24) and an electrochemical mechanism (σ^*_{melc}) associated with redox active ions that permit electrical current to bridge between electrolytic conduction (σ_{el}) in the pore space and electronic conduction (σ_{elc}) in iron minerals (23). The measured σ' therefore depends on σ_{el}, σ_{elc} and σ^*_{int} whereas σ'' is only dependent on σ^*_{int} (i.e. it exclusively relates to the interfacial properties of the iron minerals).

Measurements on Fe^0-sand mixtures show that the polarization (σ'') is linearly related to the S_s of the iron minerals in a Fe^0 column (24). Furthermore, Wu *et al.* (22) observed an increase in σ'' following corrosion and precipitation induced in Fe^0 columns that they primarily attributed to the increase in S_s of the iron minerals due to surface alteration. EIS measurements have demonstrated that electrical conduction (σ') increases after iron corrosion and mineral precipitation due to increased metallic mineral/electrolyte surface area combined with enhanced electronic conduction in electroactive precipitants, primarily magnetite (21). Wu *et al.* (22) similarly observed an increase in σ' of reacted Fe^0 columns that occurred coincident with precipitation of iron corrosion products including magnetite.

In this paper we describe low frequency electrical measurements on angle cores recovered from an iron barrier that has been in operation for eight years. Surface morphology, mineral phase analysis and core material elemental analysis were performed to evaluate the sensitivity of electrical measurements on iron corrosion and mineral precipitation along the cores. These measurements

were also compared with barrier aqueous geochemistry evaluated with a network of boreholes at the site. The results show that electrical measurements reflect the amount of corrosion and precipitation occurring in an operative Fe^0 PRB. Significantly, the electrical signatures on these cores are much greater than those recorded in previous synthetic studies on Fe^0 columns (22). These findings conclusively demonstrate the applicability of low frequency electrical methods for long-term monitoring of iron barriers.

Materials and Methods

Site description. The PRB under study was installed in April 1998 at the Kansas City Plant (KCP) operated by the U.S. Department of Energy (25). The barrier was designed to remediate 1, 2-dichloroethlene (1, 2-DCE) and chloroethene in contaminated groundwater migrating from the facility. Figure 1 (a, b) gives a plan and cross sectional view of the site. The PRB was constructed as a continuous 40 m (130 ft) long, 1.8 m (6 ft) wide trench. Alluvial sediments underlie the site, primarily silty clay overlying basal gravel. These alluvial sediments are underlain by bedrock shale. The PRB was constructed by filling the first 1.8 m (6 ft) of the trench with 100% iron such that the base of this section was in contact with bedrock. The remainder of the trench was then filled with 0.6 m (2 ft) of iron and 1.2 m (4 ft) of sand (Figure 1b). The thicker lower unit was designed to compensate for higher flow-through velocities associated with hydraulically conductive basal gravel resting on bedrock (Figure 1b).

The performance of the KCP PRB has been adversely affected by alteration to groundwater flow resulting from the PRB structure itself (25). Hydraulic heads measured at the site show that flow is bypassing the southern end of the barrier. Geochemical measurements show incomplete reduction of organic compounds in monitoring wells on the outflow side of the barrier towards its southern end (25).

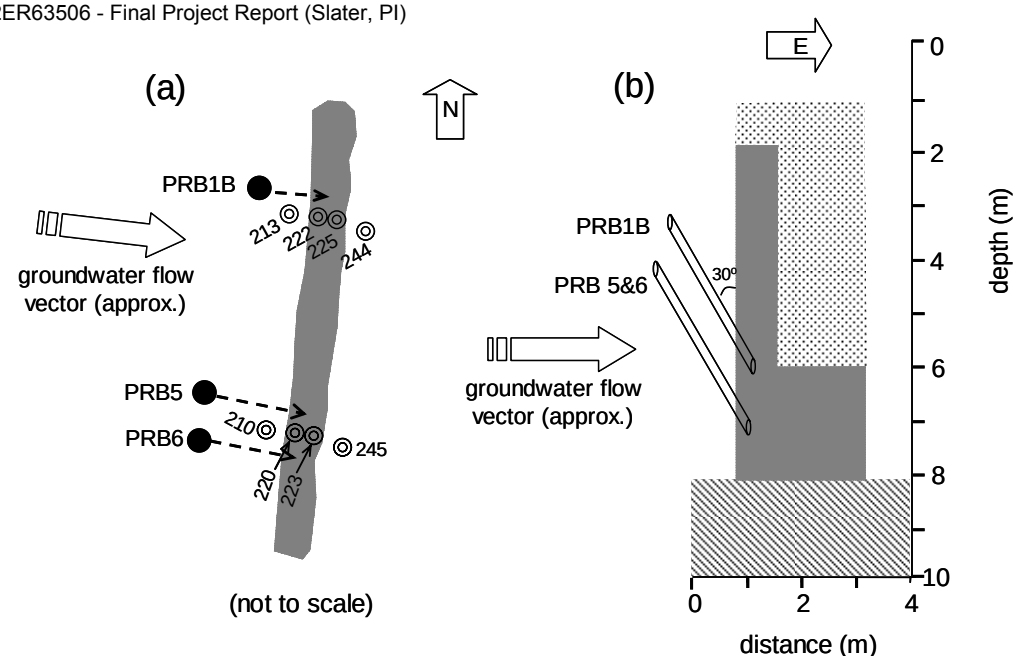

Figure 1. (a) Plan view and (b) cross section of KCP Fe^0 barrier showing the outline of the barrier (Fe^0 (▩)), basic geology (sand (⊡), shale (▧)), position of groundwater monitoring wells (◎) and cores (●).

Material acquisition. Three angle cores were recovered by driving a geoprobe containing plastic sleeves into the up gradient interface of the barrier at 30° off normal. Figure 1 shows the coring configuration. Core PRB1B penetrated the soil/iron interface at a depth of approximately 3.6 m and went into the barrier for approximately 30 cm; PRB5 and PRB6 penetrated the interface at about 7 m and went into the barrier about 22 cm. Immediately following extraction, natural soil was removed, cores were bathed in Argon to limit air oxidation and then sealed with plastic end caps. Visual observation showed that cores were generally black throughout with material closest to the upgradient soil/iron interface seemingly cemented and of finer particle size. A section of sand was encountered in the middle section of core PRB1B (Figure S1).

Electrical measurements. Figure S1 in supporting information illustrates the measurement setup. Cores comprised the upgradient soil/iron interface, the cemented and finer material representing reacted iron on the upgradient edge of the barrier as well as less reacted iron deeper within the barrier. A gradual change from reacted to less reacted iron was observed and no distinct interface

identified. SEM images (described later) suggest that the transition to pure unreacted Fe^0 was captured in PRB5 but it was not fully captured in PRB1B and PRB6.

Core holders were modified in an anaerobic chamber to permit electrical measurements. A stainless steel mesh was housed within the cap for current injection. Measuring (potential) electrode ports were installed at 3 cm intervals along the cores with the first port (port1) just inside the Fe^0 at the upgradient soil/iron interface. The total number of ports varied according to the length of each core. Core PRB1B had eight ports, core PRB5 had six ports and core PRB6 had five ports. Cores were re-saturated with deoxygenated KCP groundwater (fluid conductivity (σ_w) = 0.073 ± 0.004 S/m) prior to electrical measurements. Electrical measurements were made between each pair of adjacent ports to acquire a sequence of electrical signatures from the soil/iron interface into the barrier.

The phase shift (ϕ) and conductivity magnitude ($|\sigma|$) for each section were recorded relative to a reference resistor (Supporting information, Figure S1) for forty frequencies spaced at equal logarithmic intervals from 0.1 to 1000 Hz. The real and imaginary parts of the complex conductivity were determined from the following equations,

$$\sigma'' = |\sigma| \times \sin\phi \tag{2}$$

$$\sigma' = |\sigma| \times \cos\phi \tag{3}$$

Electrical data modeling. Physically-based models to describe $\sigma^*(\omega)$ of soils are lacking and macroscopic representations, such as the Cole-Cole model (26), are typically adopted (see for review (27)). The dependence of complex conductivity with frequency was modeled as (28),

$$\sigma^* = \sigma_0 \left[1 + m \left(\frac{(i\omega\tau)^c}{1 + (i\omega\tau)^c (1-m)} \right) \right] \tag{4}$$

where σ_0 is the conductivity at DC frequency, τ is the mean relaxation time, c is a shape exponent (typically 0.1-0.6) and m is the chargeability ($m = 1 - \sigma_0 / \sigma_\infty$, where σ_∞ is the conductivity at high frequency). The two model parameters of interest here are σ_0 and $m_n = m \times \sigma_0$, representing global

measures of conduction and interfacial polarization respectively (29). We inverted electrical data using an algorithm based on a least-squares approach with Marquardt regularization (30).

Corrosion assessment. Samples for solid phase analysis were extracted from cores after completion of electrical measurements. Cross sectional Scanning Electron Microscopy (SEM) imaging and S_s measurements were used to characterize changes in corrosion and precipitation along each core. One sample was acquired between each pair of adjacent ports and split into two subsamples for SEM imaging and S_s measurements. Samples were transported onto filter paper and gently washed with deoxygenated acetone/water solution (1:1 volume ratio) for approximately 2 minutes to eliminate residual solution. Samples were then left to dry in the anaerobic chamber for 4 hours. Surface and cross-sectional SEM imaging was conducted for each sample to acquire a sequence of morphological changes along each core following the same procedure described in (22).

The S_s of each sample was measured in triplicate with a five point Brunauer, Emmett and Teller (BET) (31) method using a high speed nitrogen sorption analyzer model NOVA 3000 from Quantachrome instruments (Boynton Beach, Florida). The uncertainty of the measurements, based on the standard deviation of repeat measurements on a single sample, is less than 3%.

Mineral phase analysis. X-ray diffractometry (XRD), supported by SEM imaging was used for mineral phase identification. Ten grams of each sample were ground with an agate mortar and pestle to acquire fine grains. A Philips PW3040 powder X-ray diffractometer was employed following the same procedure described in (22). Scans of 2θ = 15 - 90º were acquired (scan rate of 0.02º per step). X'pert highscore was used for mineral phase identification.

Results and discussion

Complex conductivity. Figure 2 shows the changes of σ' and σ'' as a function of frequency for all three cores. The distance in the legend refers to the position of the midpoint of any two consecutive

potential electrodes from the upgradient soil/iron interface (e.g. subsection between port 1 and 2 is represented as “1.5 cm”).

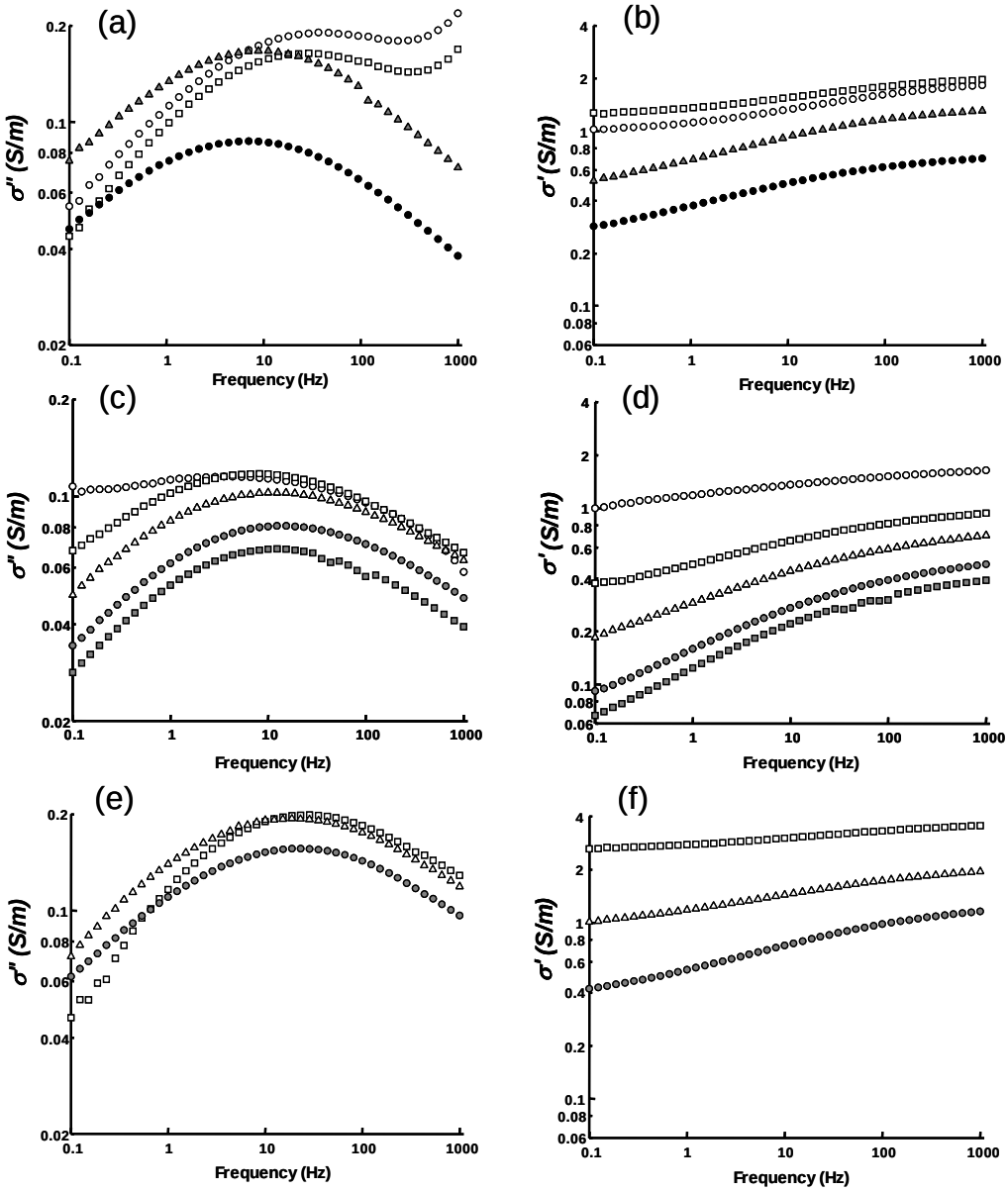

Figure 2. Spectral electrical data of three cores at different locations (1.5 (○), 4.5 (▫), 7.5 (△), 10.5 (◍), 13.5 (▪), 16.5 (▲) and 19.5 (●) cm): (a) σ'' of core PRB1B; (b) σ' of core PRB1B; (c) σ'' of core PRB5; (d) σ' of core PRB5; (e) σ'' of core PRB6; (f) σ' of core PRB6. Data are plotted on logarithmic scale. The three measurements from 7.5 – 13.5 cm for PRB1B and that from 1.5 cm for PRB6 are not plotted as they were not 100% PRB material (Figure S1).

We excluded the following measurements from the plot in order to emphasize the differences in

the electrical measurements that result exclusively from iron mineral alteration: (1) 1.5 cm in PRB6 as small portions of native soil were visually observed in the region 0-1 cm along this core (2) 7.5, 10.5 and 13.5 cm in PRB1B as a sand inclusion was encountered between 8-13 cm from the interface in this core (Figure S1). Figure 2 (a, c and e) shows a continuous decrease of σ'' away from the soil/iron interface into each core. Figure 2 (b, d and f) illustrates that a reduction in σ' also occurs with greater distance from the upgradient soil interface.

Figure 3 shows the variation of Cole-Cole model parameters m_n (Figure 3a) and σ_0 (Figure 3b) along the three cores.

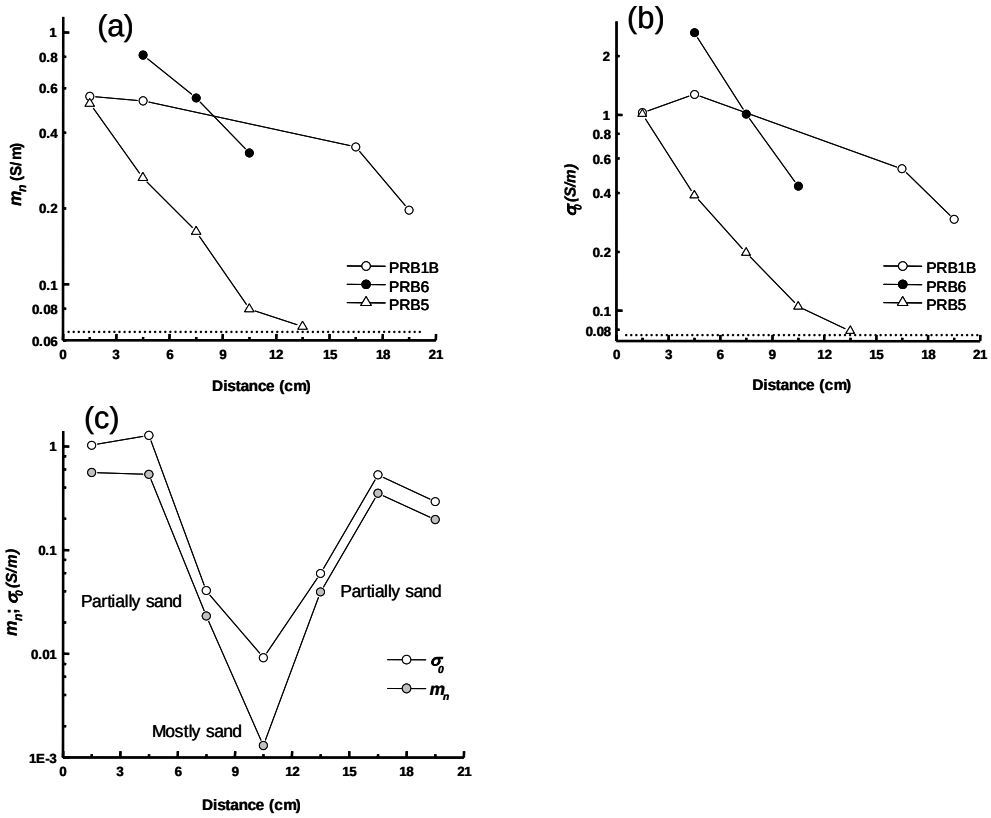

Figure 3. Cole-Cole model parameters m_n and σ_0 as a function of distance from the soil/iron interface for three cores (a) m_n (b) σ_0 ((PRB1B (○), PRB5 (△), PRB6 (●)).The dashed lines in (a) and (b) represent the values of unreacted iron. Each plot has a logarithmic y-axis and linear x-axis. (c) PRB1B replotted to include the samples affected by the sand encountered in this core from 8 - 13 cm (σ_0 (○), m_n (●)).

The modeling results are consistent with the behavior inferred from spectral data (Figure 2): m_n and σ_0 consistently decrease with distance from the upgradient soil interface. The model parameters are approximately 10 times higher at the interface in PRB5 relative to the last measurement at 13.5 cm on this core. For PRB1B and PRB6 the parameters are 2-4 times higher at the interface relative to the least reacted Fe^0 in each core (i.e. the last point on each of these cores). Figure 3c shows m_n and σ_0 for PRB1B replotted to include those locations where sand was sampled (7.5 cm, 10.5 cm and 13.5 cm) in order to illustrate the dramatic decrease in m_n and σ_0 as a result of the sand inclusion.

Corrosion level analysis. Cross sectional SEM imaging indicates a decrease in the amount of surface corrosion with distance from the soil/iron interface into the barrier. Figure 4 shows selected SEM images for PRB1B and PRB5. Images for PRB6 are available in figure S3 of supporting information. The images suggest that the amount of surface corrosion differs between cores, being greatest in PRB1B.

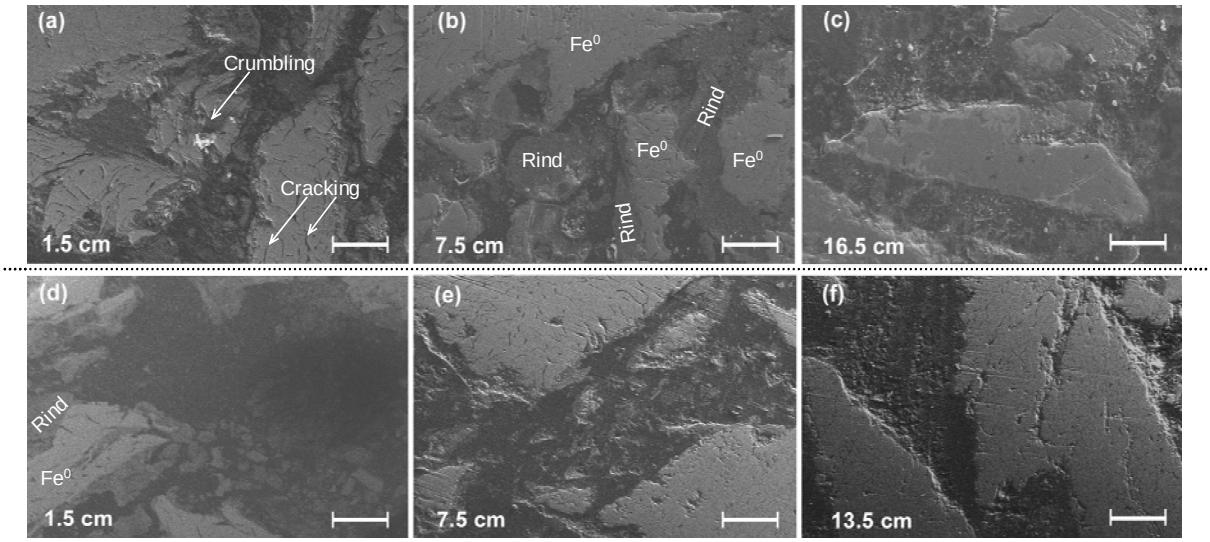

Figure 4. Cross sectional SEM image sequences of PRB1B and PRB5: (a) PRB1B 1.5 cm; (b) PRB1B 7.5 cm; (c) PRB1B 16.5 cm; (d) PRB5 1.5 cm; (e) PRB5 7.5 cm and (f) PRB5 13.5 cm. Bar: 200 μm.

For example, the image of PRB1B 1.5 cm (Figure 4a) reveals severe corrosion, with crumbling and cracking of iron particles. Further into the core at PRB1B 7.5 cm (Figure 4b), iron particles

retain a thick corrosion rind, but crumbling and cracking is absent. PRB1B 16.5 cm (Figure 4c) shows only a thin and discontinuous corrosion rind suggesting minor corrosion; PRB1B 19.5 cm (image not presented for brevity) showed little evidence of corrosion rind.

Images of PRB5 1.5 cm (Figure 4d) also reveal a thick, continuous corrosion rind although there is no visible crumbling or cracking of iron materials, suggesting less corrosion compared with the same location in PRB1B; PRB5 7.5 cm (Figure 4e) shows a discontinuous, thin corrosion rind whereas PRB5 13.5 cm (Figure 4f) shows no corrosion rind. These results suggest that the corrosion front in PRB1B (collected at the northern end of the barrier) (≥16.5 cm) is considerably wider than in PRB5 (collected at the southern end of the barrier) (≤13.5 cm). PRB6 similarly showed a pattern of corrosion rind development with samples close to the soil/iron interface showing more severe corrosion than samples far from it (Figure S3). The sample captured furthest from the soil/iron interface in this core (PRB6 10.5 cm) still showed a corrosion rind, particularly on smaller particles.

BET surface area measurements revealed a continuous decrease of S_s (from 10.9 m^2/g to 4.9 m^2/g in PRB1B, from 6.3 m^2/g to 4.0 m^2/g in PRB5 and from 13.3 m^2/g to 4.5 m^2/g in PRB6) from the most reacted (closest to soil/iron interface) to the least reacted iron (furthest to soil/iron interface) (Table S1). The high S_s at the soil/iron interface is consistent with surface complexity and a high fraction of fine mineral precipitates resulting from severe iron corrosion and mineral precipitation. Among the three cores, PRB1B had the largest S_s at each location, indicating the most severe corrosion.

Mineral precipitation analysis. XRD scans and SEM equipped with energy dispersive X-ray spectroscopy (EDX) provided qualitative information on likely mineral phases; these included iron oxide/hydroxide, carbonate minerals, sulfide minerals, green rusts and quartz. All three cores exhibit similar XRD characteristics with mineralogical complexity decreasing with distance from the soil/iron interface into the core. XRD scans for core PRB5 are presented in figure 5, and scans for

PRB1B (Figure S5) and PRB 6 (Figure S6) are available in supporting information.

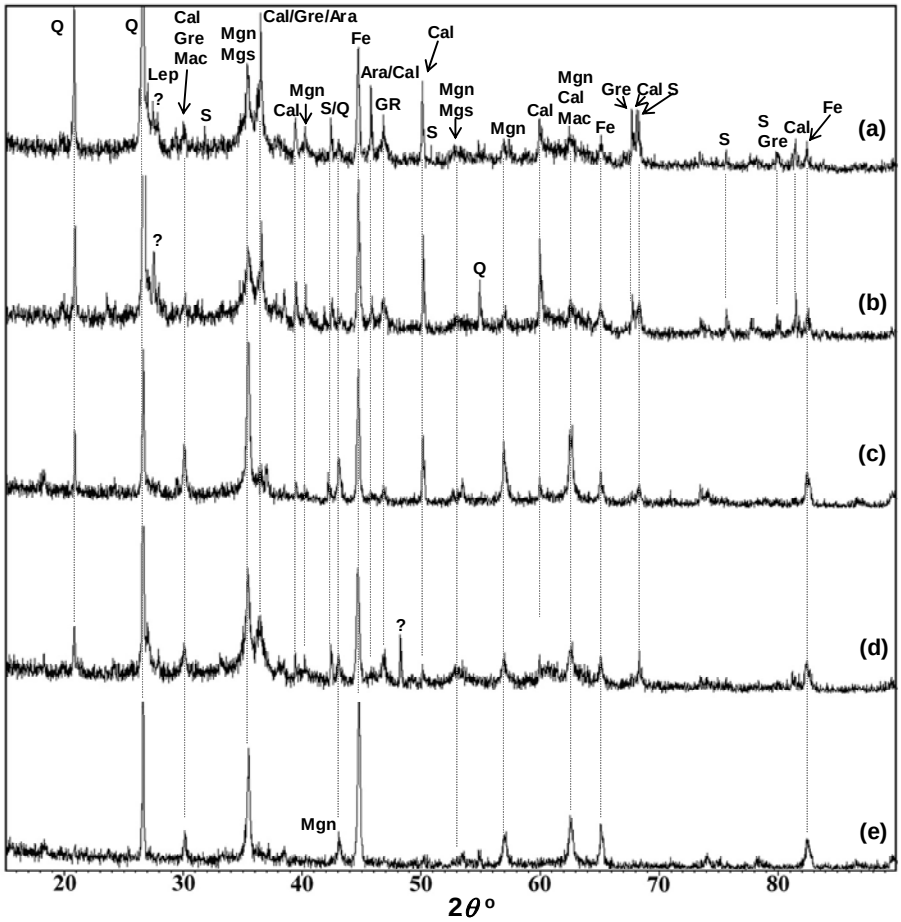

Figure 5. X-ray diffractograms of samples from PRB5 at locations: (a) 1.5 cm; (b) 4.5 cm; (c) 7.5 cm; (d) 10.5 cm; (e) 13.5 cm. (Mgh-maghemite, Mgn-magnetite, Cal-calcite, Ara-aragonite, S-siderite, Mgs-magnesite, Gre-greigite, Mac-mackinawite, Lep-lepidocrocite, GR-green rusts, Fe-Fe^0, Q-quartz).

All cores show evidence of iron oxide/hydroxide mineral phases. Magnetite (Fe_3O_4) was identified as the dominant iron oxide in all cores consistent with the reductive environment within the barrier (pH = 9-10 and Eh = -120 - -210 mV, Table 1a). Geochemical modeling with PHREEQC confirmed that magnetite is the major iron oxide forming under this pH-Eh range. The black color of the cores supports widespread existence of magnetite.

Siderite ($FeCO_3$), calcite (α-$CaCO_3$), aragonite (β-$CaCO_3$) as well as magnesite ($MgCO_3$) were

identified as major carbonate minerals (Figure 5, S5 and S6), calcite being the dominant phase. The characteristic triagonal crystalline structure of calcite was identified in SEM images (Figure S4b). Aragonite and siderite were identified in all cores. Geochemical modeling with PHREEQC showed that iron carbonate and calcium carbonate are oversaturated in the barrier and can precipitate under the given geochemical conditions (Table 1a). Moreover, groundwater geochemical analysis (Table 1a) suggests significant removal of Ca, Fe, Mg and reduced alkalinity in the barrier, providing evidence for iron/calcium/magnesium carbonate mineral precipitation. Core material elemental analysis (Table 1b) showed precipitation of Ca and Inorganic Carbon (IC) further supporting carbonate mineral precipitation. Note that concentrations of Ca and C were higher in PRB1B than in PRB5 and PRB6, indicating more intensive iron corrosion and mineral precipitation at the north end of the barrier.

Table 1: KCP barrier groundwater geochemistry and core material elemental analysis

(a) Groundwater geochemistry data (unit: ppm for alkalinity and ion concentrations)

	Location	Well #	pH	Eh	Alkalinity	Ca	Mg	Mn	silica	Fe	SO_4
PRB1B	Upgradient	213	6.6	-105.2	553	207	18.7	3.86	45.5	41.5	9.18
	In barrier	222	9.8	-170	49	13.9	0.07	0	1.69	0	0
		225	10	-213.6	47	5.64	0.23	0	2.88	0.053	1.9
	Downgradient	244	9.3	-129.8	30	37.8	1.35	0.01	1.7	0.0525	85.8
PRB5&6	Upgradient	210	6.8	-118	452	181	16.4	3.55	36.8	25	25.8
	In barrier	220	9	-182.9	34	36.2	1.89	0	0	0	0
		223	9.7	-119.9	36	31.8	2.76	0.007	0		0
	Downgradient	245	7.2	-124.9	422	178	15.5	4.24	45.9	25.3	34.8

(b) Core material elemental analysis data (unit: ppm)

Name	**PRB1B**							**PRB5**					**PRB6**			
	1.5	4.5	7.5	10.5	13.5	16.5	19.5	1.5	4.5	7.5	10.5	13.5	1.5	4.5	7.5	10.5
IC	367	269	373	634	11	168	246	25	110	128	228	252	128	17	116	60
Ca	119	nd	nd	1580	526	nd	nd	295	998	276	263	248	nd	nd	nd	nd
S	49	59	161	81	77	63	31	1	50	40	56	68	39	38	54	24

Iron sulfides (greigite (Fe_3S_4) and mackinawite (FeS)) were also identified by XRD (Figure 5, S5 and S6). SEM/EDX revealed that Fe and S are major elements of elongated circular-shaped mineral aggregates (Figure S4c), possibly being sulfate reducing bacteria covered by iron sulfide. Groundwater geochemical analysis (Table 1a) revealed a decrease of SO_4^{2-} from 10-25 mg/L outside

of the barrier to below 2 mg/L within the barrier. Sulfur was also identified in core material elemental analysis at higher concentrations in PRB1B than in PRB5 and PRB6 (Table 1b) further suggesting greater reactivity towards the north of the barrier.

Green rusts (mineral phases of mixed Fe^{2+}/Fe^{3+} oxy (hydroxide) layers with anions (i.e. Cl^-, CO_3^{2-}, SO_4^{2-}) frequently incorporated into inner-layer spaces (32)) were identified by XRD in all cores (Figure 5, S5 and S6) and a characteristic hexagonal platelet morphology observed with SEM surface imaging (Figure S4a) (32,33). Quartz was identified in most of the samples, probably due to both Si impurities (2%) in peerless iron and partial incorporation of natural soil or sand into the barrier. Geochemical monitoring also revealed significant reduction of silica in the barrier (Table 1a).

Interpretation of electrical measurements. Our geochemical analyses indicate that the complex conductivity variation in these cores is directly related to Fe^0 corrosion and mineral precipitation. The gradual decrease in the real and imaginary parts of the complex conductivity and equivalent Cole-Cole model parameters with distance into the barrier coincides with the gradual decrease in surface morphological and mineralogical alteration due to corrosion and precipitation with distance from the upgradient soil/iron interface. The gradients of the m_n and σ_0 curves of PRB1B (Figure 3a and b) are less than those of PRB5 and PRB6, indicating a wider interface of corrosion at PRB1B. This is consistent with the cross sectional SEM imaging, which clearly shows that PRB1B exhibits a wider zone of corrosion and precipitation relative to the other cores. Furthermore, aqueous geochemistry suggests that preferential flow close to PRB1B results in greater precipitation of carbonates and sulfides at this end of the barrier.

Cole-Cole modeling of electrical measurements on unreacted peerless iron (obtained directly from the supplier) saturated with KCP groundwater resulted in values of m_n and σ_0 of 0.06 S/m and 0.07 S/m respectively (Figure 3). The respective values at 13.5 cm in PRB5 are m_n = 0.068 S/m and σ_0 =

0.079 S/m, suggesting that the sample obtained here is essentially unreacted Fe^0. The core for PRB5 therefore probably captured the full interface of reacted/unreacted iron. However, m_n and σ_0 are much higher at 19.5 cm in PRB1B and 10.5 cm in PRB6, indicating some reacted iron at these locations and implying that the interface of reacted/unreacted iron in these cores was not fully captured. This conclusion is again well supported by SEM imaging. For example, the image at 10.5 cm for PRB6 exhibits a clear corrosion rind (Figure S3d) whereas the image at 13.5 cm in PRB5 shows little evidence of corrosion (Figure 4f).

We attribute the increased complex conductivity associated with increasing corrosion and precipitation to the combined effects of Fe^0 surface morphological change and mineralogical alteration, consistent with laboratory experiments (22). The increase of S_s due to iron corrosion and mineral precipitation increases the metal/electrolyte contact area and thus enhances interfacial polarization; it also increases conduction as there are more sites for redox-driven charge transfer across the metal/electrolyte interface. This is supported by EIS results showing that corrosion reduces the charge transfer resistance across the metallic mineral/electrolyte interface (20,21). Under the condition of minimally altered metallic mineral phase a near-linear correlation between m_n and BET estimated S_s has been observed (24). However, significant mineral phase changes, as observed in these cores, prevent establishment of a simple quantitative relationship between m_n and BET estimated S_s (22).

Our results suggest that conduction increases more than polarization in response to mineralogical alteration and corrosion and the formation of secondary mineral phases in these cores. We attribute this to the nature of the mineralogical alteration of the iron surface. Nanoporous precipitates that still allow charge transfer between Fe^0 redox sites and electrolyte, as well as nonporous, electroactive precipitates, can both provide electron pathways between Fe^0 and electrolyte that enhance redox reactions and thus electronic conduction by facilitating charge transfer from the Fe^0 surface to

oxidants in electrolyte (20). Magnetite, the dominant mineral phase in these cores, is particularly effective at facilitating such charge transfer (34) such that magnetite precipitation improves conduction in metallic minerals (21).

Research on iron corrosion has shown that minerals precipitate either as an iron surface coating, increasing surface complexity (hence surface area), or as discrete mineral clusters infilling pores that can reduce surface area under severe clogging (8,9,17). Only mild clogging by iron minerals close to the soil/iron interface was observed in cores during sample preparation. Research shows that major mineral phases contributing to porosity loss are $CaCO_3$ > Fe_3O_4 (10). Core material elemental analysis was used to estimate porosity loss due to $CaCO_3$ precipitation (Table 1b) applying the standard used in (33) that 3.2 mg of C per g of Fe could account for a void volume reduction of ~5%. A 3.2% porosity loss was calculated at the soil/iron interface, decreasing into the cores. This small porosity loss is consistent with our results in that conduction and polarization both increase as expected following precipitation of surface coatings and discrete fine particles.

Our previous results on synthetic laboratory Fe^0 columns revealed 23-35% increases of m_n and 25-45% increases of σ_0 resulting from short term iron corrosion and mineral precipitation (22). The field cores exhibit much greater changes in electrical properties (Figure 3) between the most and least reacted zones. This is expected as the corrosion and precipitation observed after eight years of operation of the Kansas City Plant PRB is much greater than that generated in our synthetic studies (as apparent from SEM). Thus it is clear that geoelectrical measurements have adequate sensitivity to detect mineralogical alteration within field PRB installations. Furthermore, results for core PRB1B (Figure 3c, S1) demonstrate that electrical measurements are very sensitive to contamination of the Fe^0 by non-metallic minerals (in this case sand) and could therefore be applied for detecting flaws in the construction and installation of a PRB.

The clear relationship between low frequency electrical measurements and degree of corrosion in

cores from a field PRB has confirmed that low frequency electrical methods could be used to non-invasively evaluate iron corrosion and mineral precipitation in field PRB installations. The four-electrode measurement used here is readily up-scalable to a downhole measurement or even to electrical imaging (over a narrower range of low frequencies) using electrodes placed around the edge of the barrier (14). Long term monitoring of indicators of performance reduction in PRBs using geoelectrical tools applied in the field therefore appears possible and should be encouraged.

Acknowledgements. This research was supported by the Environmental Management Science Program (EMSP) of the Office of Science, U.S. Department of Energy, grant DE-FG07-02ER63506. Andreas Kemna (Institute of Chemistry and Dynamics of the Geosphere, Forschungszentrum Jülich) provided Cole-Cole relaxation modeling support. The support of Joe Baker (Honeywell FM&T) for site logistics and sampling, and from Rick Wilkin (U.S. Environmental Protection Agency) and Robert S. Kerr Laboratory, Ada, Oklahoma for core analysis, is gratefully acknowledged.

Supporting information available. Schematic of the cores and electrical measurement setup; cross sectional SEM images of samples from PRB6; Surface SEM imaging of selected precipitates; XRD scans for samples from PRB1B showing identified phases; XRD scans for samples from PRB6 showing identified phases. This material is available free of charge via the internet at http://pubs.acs.org.

Literature cited

(1) Gu, B.; Liang, L.; Dickey, M. J.; Yin, X.; Dai, S. Reductive precipitation of uranium(VI) by zero-valent iron. *Environ. Sci. Technol.* **1998**, *32*, 3366-3373.

(2) Su, C. M.; Puls, R. W. In situ remediation of arsenic in simulated groundwater using zerovalent iron: Laboratory column tests on combined effects of phosphate and silicate. *Environ. Sci. Technol.* **2003**, *37*, 2582-2587.

(3) Blowes, D. W.; Ptacek, C. J.; Benner, S. G.; McRae, C. W. T.; Bennett, T. A.; Puls, R. W. Treatment of inorganic contaminants using permeable reactive barriers. *J. Contam. Hydrol.* **2000**, *45*, 123-137.

(4) Morrison, S. J.; Metzler, D. R.; Carpenter, C. E. Uranium precipitation in a permeable reactive barrier by progressive irreversible dissolution of zerovalent iron. *Environ. Sci. Technol.* **2001**, *35*, 385-390.

(5) Cantrell, K. J.; Kaplan, D. I.; Wietsma, T. W. Zero-Valent Iron for the in-Situ Remediation of Selected Metals in Groundwater. *J. Hazard. Mater.* **1995**, *42*, 201-212.

(6) Gandhi, S.; Oh, B. T.; Schnoor, J. L.; Alvarez, P. J. J. Degradation of TCE, Cr(VI), sulfate, and nitrate mixtures by granular iron in flow-through columns under different microbial conditions. *Water Res.* **2002**, *36*, 1973-1982.

(7) Kreuzer, H. Treating metal-contaminated groundwater - Permeable reactive barrier cleans superfund site. *Pollut. Eng.* **2000**, *32*, 12-14.

(8) Liang, L. Y.; Korte, N.; Gu, B. H.; Puls, R.; Reeter, C. Geochemical and microbial reactions affecting the long-term performance of in situ 'iron barriers'. *Adv. Environ. Res.* **2000**, *4*, 273-286.

(9) Liang, L. Y.; Sullivan, A. B.; West, O. R.; Moline, G. R.; Kamolpornwijit, W. Predicting the precipitation of mineral phases in permeable reactive barriers. *Environ. Eng. Sci.* **2003**, *20*, 635-653.

(10) Kamolpornwijit, W.; Liang, L.; West, O. R.; Moline, G. R.; Sullivan, A. B. Preferential flow path development and its influence on long-term PRB performance: column study. *J. Contam. Hydrol.* **2003**, *66*, 161-178.

(11) Wilkin, R. T.; Puls, R. W.; Sewell, G. W. Long-term performance of permeable reactive barriers using zero-valent iron: Geochemical and microbiological effects. *Ground Water.* **2003**, *41*, 493-503.

(12) Odziemkowski, M. S.; Schuhmacher, T. T.; Gillham, R. W.; Reardon, E. J. Mechanism of oxide film formation on iron in simulating groundwater solutions: Raman spectroscopic studies. *Corros. Sci.* **1998**, *40*, 371-389.

(13) Benner, S. G.; Blowes, D. W.; Molson, J. W. H. Modeling preferential flow in reactive barriers: Implications for performance and design. *Ground Water.* **2001**, *39*, 371-379.

(14) Slater, L.; Binley, A. Evaluation of permeable reactive barrier (PRB) integrity using electrical imaging methods. *Geophysics.* **2003**, *68*, 911-921.

(15) Reardon, E. J. Anaerobic Corrosion of Granular Iron - Measurement and Interpretation of Hydrogen Evolution Rates. *Environ. Sci. Technol.* **1995**, *29*, 2936-2945.

(16) Farrell, J.; Kason, M.; Melitas, N.; Li, T. Investigation of the long-term performance of zero-valent iron for reductive dechlorination of trichloroethylene. *Environ. Sci. Technol.* **2000**, *34*, 514-521.

(17) Mackenzie, P. D.; Horney, D. P.; Sivavec, T. M. Mineral precipitation and porosity losses in granular iron columns. *J. Hazard. Mater.* **1999**, *68*, 1-17.

(18) Phillips, D. H.; Gu, B.; Watson, D. B.; Roh, Y.; Liang, L.; Lee, S. Y. Performance evaluation of a zerovalent iron reactive barrier: Mineralogical characteristics. *Environ. Sci. Technol.* **2000**, *34*, 4169-4176.

(19) Melitas, N.; Conklin, M.; Farrell, J. Electrochemical Study of Arsenate and Water Reduction on Iron Media Used for Arsenic Removal from Potable Water. *Environ. Sci. Technol.* **2002**, *36*, 3188-3173.

(20) Melitas, N.; Farrell, J. Understanding Chromate reaction kinetics with corroding iron media using Tafel analysis and Electrochemical Impedance Spectroscopy. *Environ. Sci. Technol.* **2002**, *36*, 5476-5482.

(21) Mishra, D.; Farrell, J. Understanding nitrate reactions with zerovalent iron using tafel analysis and electrochemical impedance spectroscopy. *Environ. Sci. Technol.* **2005**, *39*, 645-650.

(22) Wu, Y.; Slater, L. D.; Korte, N. Effect of precipitation on low frequency electrical properties of zero valent iron columns. *Environ. Sci. Technol.* **2005**, *Accepted*.

(23) Wong, J. An electrochemical model of the induced-polarization phenomenon in disseminated sulfide ores. *Geophysics.* **1979**, *44*, 1245-1265.

(24) Slater, L. D.; Choi, J.; Wu, Y. Electrical properties of iron-sand columns: Implications for induced polarization investigation and performance monitoring of iron-wall barriers. *Geophysics.* **2005**, *70*, G87-G94.

(25) Laase, A.; Korte, N.; Baker, J.; Dieckmann, P.; Vogan, J.; Focht, R. In *2nd International Conference on Remediation*; Wickramanavake, G., Gavaskar, A., Chen, A., Eds.: Columbus, Ohio, 2000; pp 417-424.

(26) Pelton, W. H., Sill, W.R., Smith, B.D. Interpretation of complex resistivity and dielectric data. Part I. *Geophysical Transactions.* **1978**, *29*, 297-330.

(27) Dias, C. Developments in a model to describe low-frequency electrical polarization in rocks. *Geophysics.* **2000**, *65*, 437-451.

(28) Jones, D. P.; Department of geophysics, Colorado School of Mines, 2002; p 403.

(29) Lesmes, D. P.; Frye, K. M. Influence of pore fluid chemistry on the complex conductivity and induced polarization responses of Berea sandstone. *J. Geophys. Res-Sol. Ea.* **2001**, *106*, 4079-4090.

(30) Kemna, A. *Tomographic inversion of complex resistivity - theory and application*; Der Andere Verlag: Osnabrück, Germany, 2000.

(31) Brunauer, S. E.; P. H.; Teller, E. Adsorption of gases in multimolecular layers. *Journal of the American Chemical Society.* **1938**, *60*, 309-319.

(32) Legrand, L.; Savoye, S.; Chausse, A.; Messina, R. Study of oxidation products formed on iron in solutions containing bicarbonate/carbonate. *Electrochim. Acta.* **2000**, *46*, 111-117.

(33) Gu, B.; Phelps, T. J.; Liang, L.; Dickey, M. J.; Roh, Y.; Kinsall, B. L.; Palumbo, A. V.; Jacobs, G. K. Biogeochemical dynamics in zero-valent iron columns: Implications for permeable reactive barriers. *Environ. Sci. Technol.* **1999**, *33*, 2170-2177.

(34) Simard, S.; Odziemkowski, M.; Irish, D. E.; Brossard, L.; Menard, H. In *191st Meeting of the Electrochemical Society*: Montreal, Quebec, 1997; Vol. 97, pp 279-280.

One sentence synopsis:

Electrical measurements are indicative of the level of corrosion and precipitation in cores obtained from a field permeable reactive barrier (PRB) installation in operation for eight years, demonstrating the applicability of electrical geophysical methods for monitoring corrosion in reactive barriers.

Supporting Information

Low Frequency Electrical Properties of Corroded Iron Barrier Cores

Yuxin Wu, Lee D Slater, Nic Korte

Pages: 6
Contents: 5 figures (S1-S5)
1 table (S1)

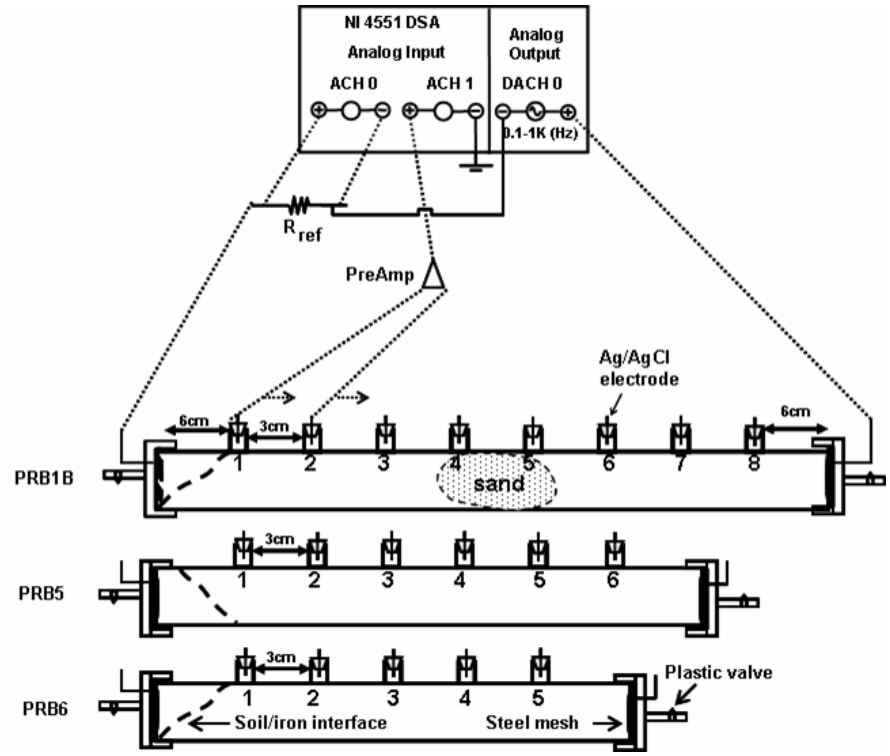

Figure S1. Schematic diagram of the cores and electrical measurement setup. Core PRB1B had 8 electrode housing ports installed with an interval of 3 cm, PRB5 had 6 ports and PRB6 had 5 ports. Note that a section of sand from 8 – 13 cm of PRB1B was included in PRB1B. Electrical measurements were measured between each pair of adjacent ports along the cores using a National Instruments (NI) Dynamic Signal Analyzer (DSA).

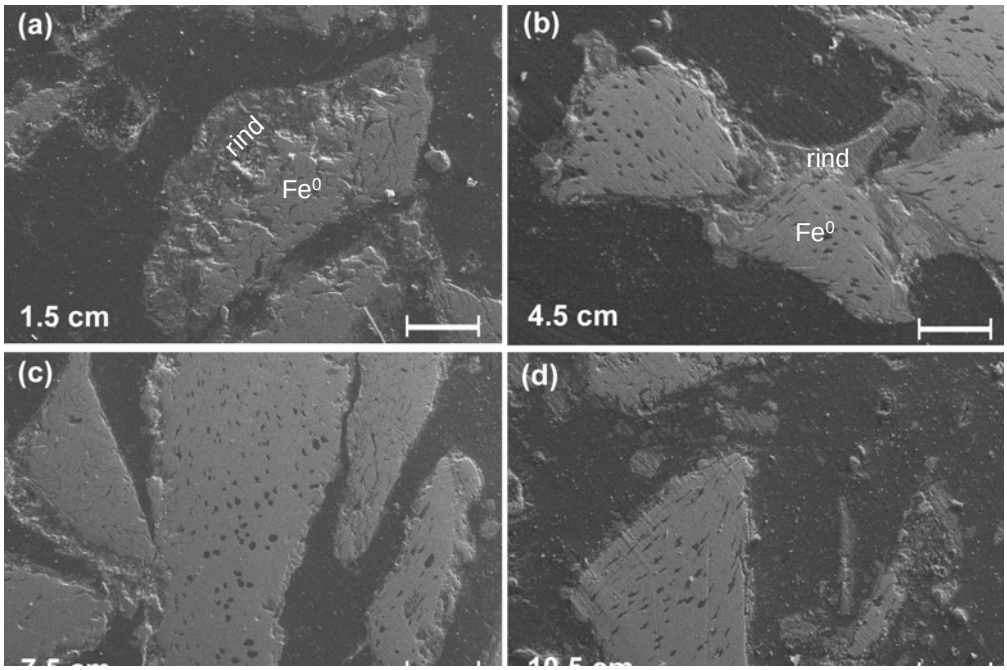

Figure S2. Cross sectional SEM images of samples from PRB6: (a) image from section 1.5 cm; (b) image from section 4.5 cm; (c) image from section 7.5 cm; (d) image from section 10.5 cm. Bar: 200 μm.

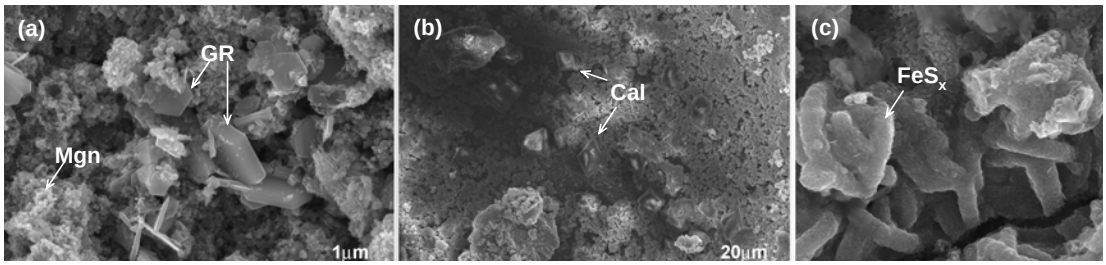

Figure S3. Surface SEM imaging of selected precipitates. (a) Magnetite and green rusts from PRB1B section 16.5 cm, (b) crystalline Calcite from PRB5 7.5 cm, (c) iron sulfide minerals from PRB6 4.5 cm. (Mgn-magnetite, GR-green rusts, Cal-calcite, FeS_x-iron sulfide).

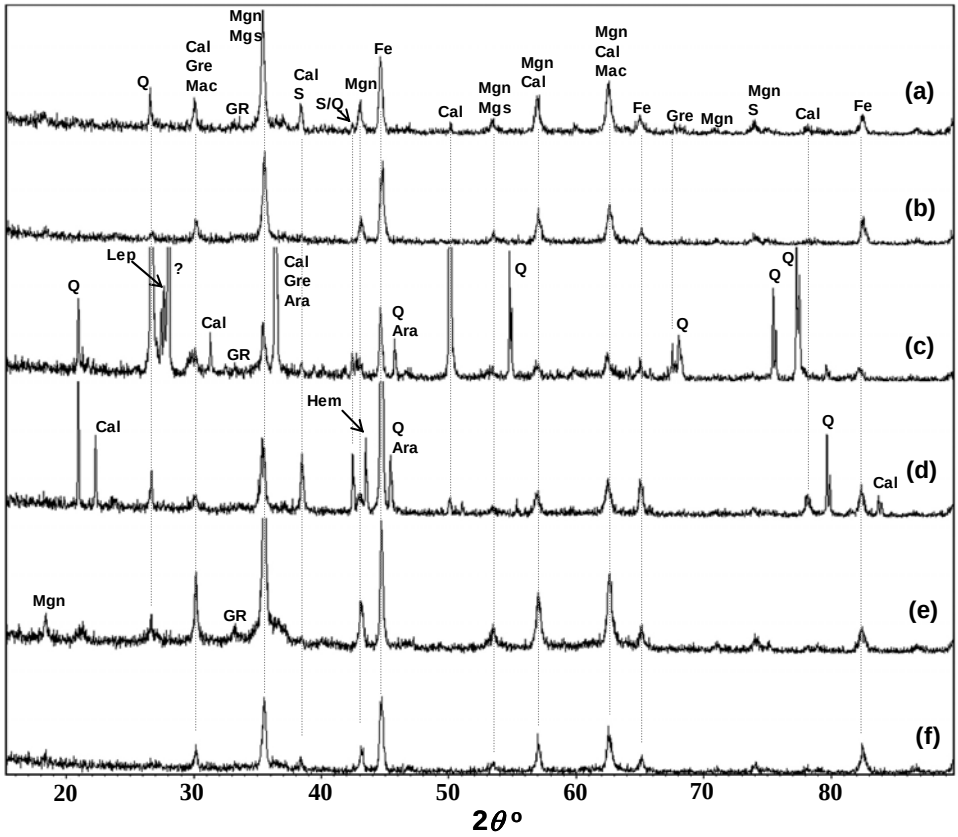

Figure S4. X-ray diffractograms of samples from PRB1B at locations: (a) 1.5 cm; (b) 4.5 cm; (c) 7.5 cm; (d) 13.5 cm; (e) 16.5 cm; (f) 19.5 cm. (Mgh-maghemite, Mgn-magnetite, Cal-calcite, Ara-aragonite, S-siderite, Mgs-magnesite, Gre-greigite, Mac-mackinawite, Lep-lepidocrocite, GR-green rusts, Fe-Fe^0, Q-quartz).

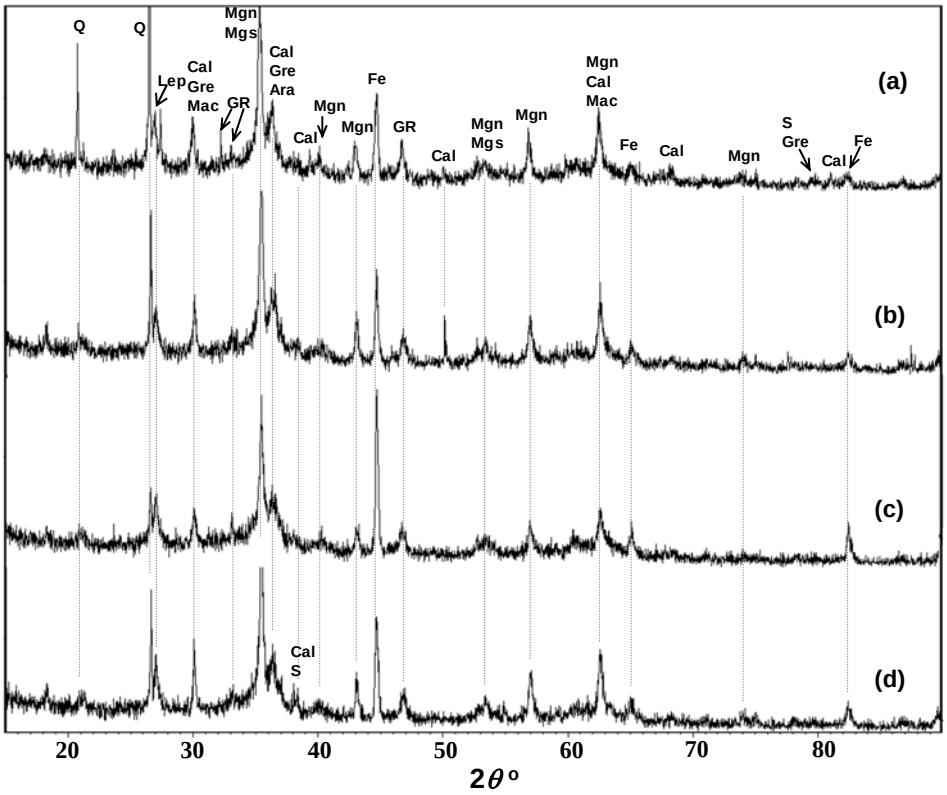

Figure S5. X-ray diffractograms of samples from PRB6 at locations: (a) 1.5 cm; (b) 4.5 cm; (c) 7.5 cm; (d) 10.5 cm. (Mgh-maghemite, Mgn-magnetite, Cal-calcite, Ara-aragonite, S-siderite, Mgs-magnesite, Gre-greigite, Mac-mackinawite, Lep-lepidocrocite, GR-green rusts, Fe-Fe^0, Q-quartz).

Table S1: Surface area measurements for three cores (unit: m^2/g)

Location	1.5 cm	4.5 cm	7.5 cm	10.5 cm	13.5 cm	16.5 cm	19.5 cm
PRB1B	10.9	8.26	5.62		4.56	6.32	4.89
PRB5	6.26	6.04	5.52	4.32	4		
PRB6	5.36	13.25	4.56	4.53			

Supporting Information

Low Frequency Electrical Properties of Corroded Iron Barrier Cores

Yuxin Wu, Lee D Slater, Nic Korte

Pages: 6

Contents: 5 figures (S1-S5)

1 table (S1)

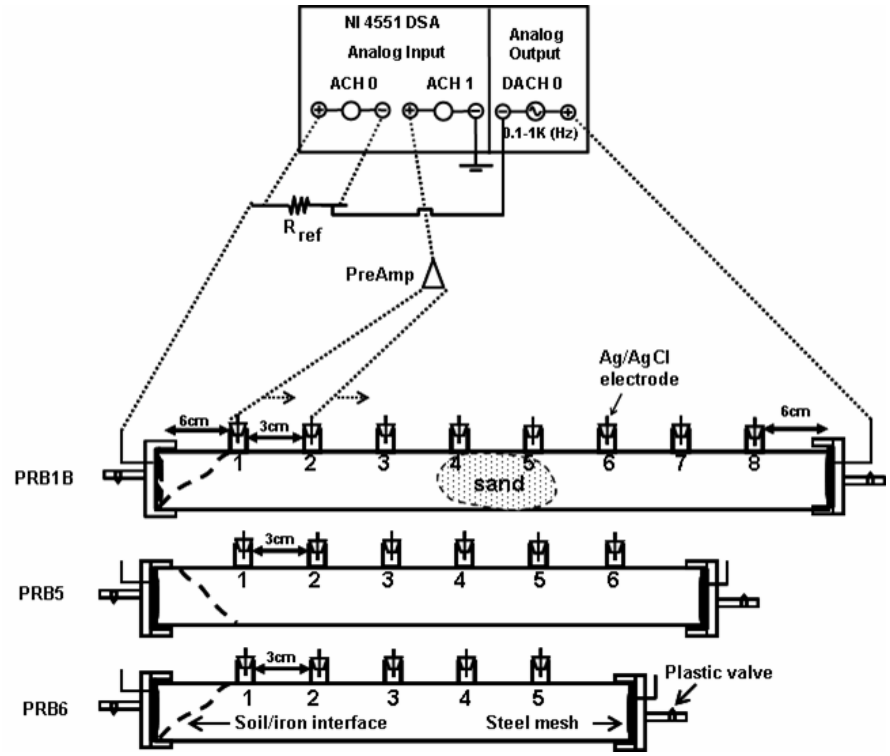

Figure S1. Schematic diagram of the cores and electrical measurement setup. Core PRB1B had 8 electrode housing ports installed with an interval of 3 cm, PRB5 had 6 ports and PRB6 had 5 ports. Note that a section of sand from 8 – 13 cm of PRB1B was included in PRB1B. Electrical measurements were measured between each pair of adjacent ports along the cores using a National Instruments (NI) Dynamic Signal Analyzer (DSA).

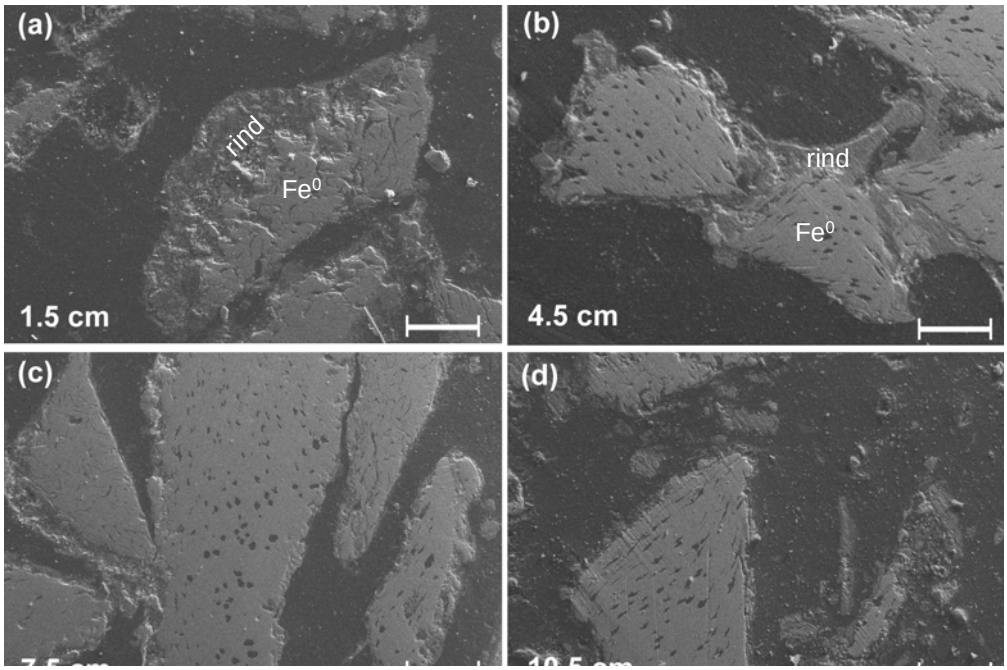

Figure S2. Cross sectional SEM images of samples from PRB6: (a) image from section 1.5 cm; (b) image from section 4.5 cm; (c) image from section 7.5 cm; (d) image from section 10.5 cm. Bar: 200 μm.

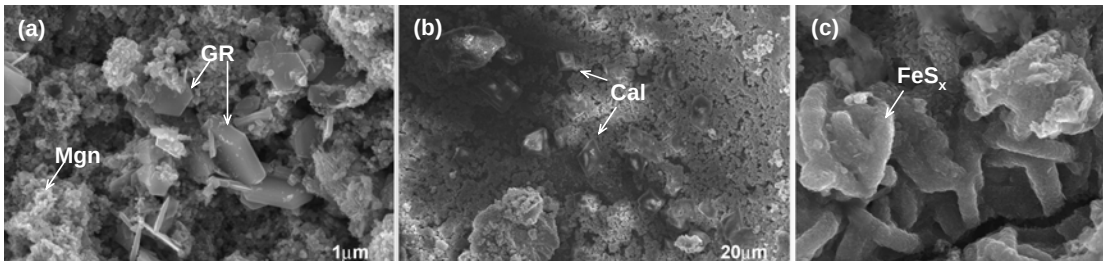

Figure S3. Surface SEM imaging of selected precipitates. (a) Magnetite and green rusts from PRB1B section 16.5 cm, (b) crystalline Calcite from PRB5 7.5 cm, (c) iron sulfide minerals from PRB6 4.5 cm. (Mgn-magnetite, GR-green rusts, Cal-calcite, FeS_x-iron sulfide).

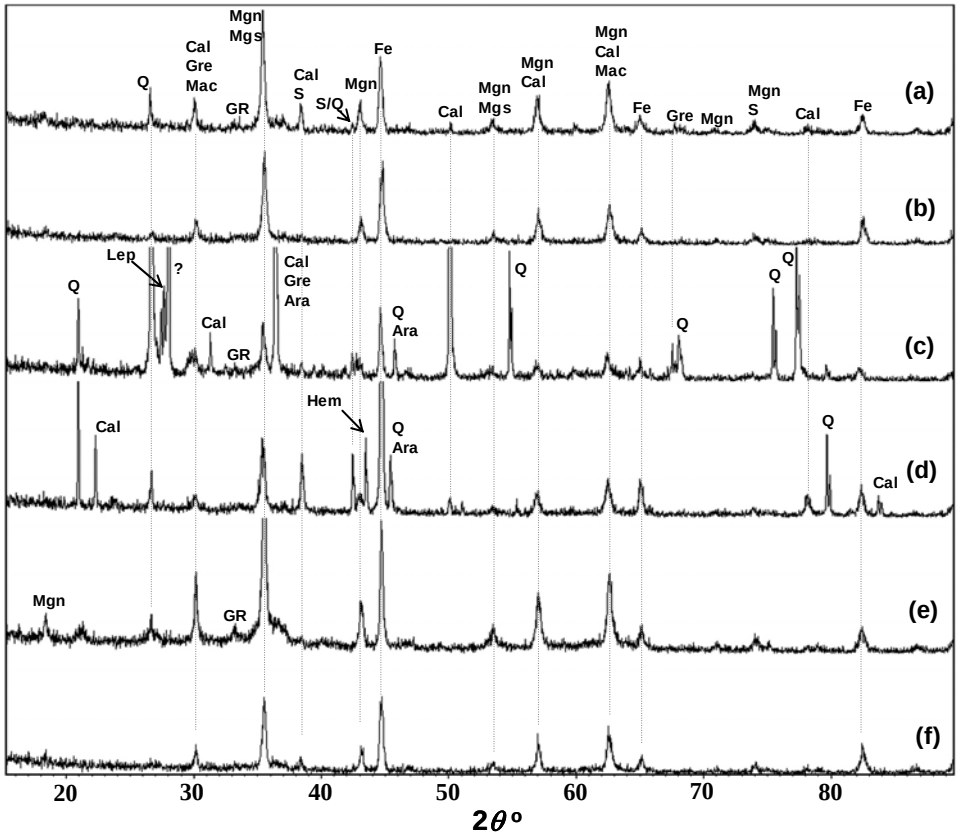

Figure S4. X-ray diffractograms of samples from PRB1B at locations: (a) 1.5 cm; (b) 4.5 cm; (c) 7.5 cm; (d) 13.5 cm; (e) 16.5 cm; (f) 19.5 cm. (Mgh-maghemite, Mgn-magnetite, Cal-calcite, Ara-aragonite, S-siderite, Mgs-magnesite, Gre-greigite, Mac-mackinawite, Lep-lepidocrocite, GR-green rusts, Fe-Fe^0, Q-quartz).

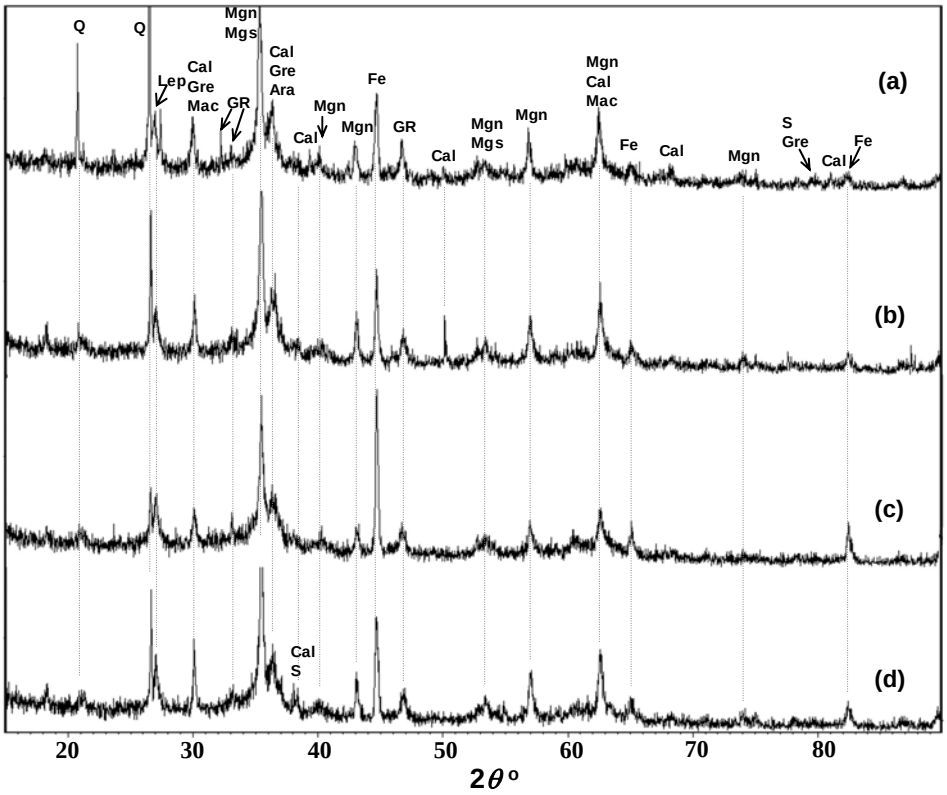

Figure S5. X-ray diffractograms of samples from PRB6 at locations: (a) 1.5 cm; (b) 4.5 cm; (c) 7.5 cm; (d) 10.5 cm. (Mgh-maghemite, Mgn-magnetite, Cal-calcite, Ara-aragonite, S-siderite, Mgs-magnesite, Gre-greigite, Mac-mackinawite, Lep-lepidocrocite, GR-green rusts, Fe-Fe^0, Q-quartz).

Table S1: Surface area measurements for three cores (unit: m^2/g)

Location	1.5 cm	4.5 cm	7.5 cm	10.5 cm	13.5 cm	16.5 cm	19.5 cm
PRB1B	10.9	8.26	5.62		4.56	6.32	4.89
PRB5	6.26	6.04	5.52	4.32	4		
PRB6	5.36	13.25	4.56	4.53			

APPENDIX 4

Slater, L. and Binley, A., 2005, Case history - synthetic & field based electrical imaging of a zerovalent iron barrier: implications for monitoring long-term barrier performance, **Geophysics**, Submitted 08/18/05.

CASE HISTORY - SYNTHETIC & FIELD BASED ELECTRICAL IMAGING OF A ZEROVALENT IRON BARRIER: IMPLICATIONS FOR MONITORING LONG-TERM BARRIER PERFORMANCE

(short title to appear as running head: Electrical monitoring of barriers)

Lee Slater[1] and Andrew Binley[2]

1. Department of Earth & Environmental Sciences, Rutgers University, 195 University Ave., Newark, NJ 07102, USA*

2. Department of Environmental Science, Lancaster University, Lancaster, LA1 4YQ, England

Corresponding author:

Lee Slater

Fax: 973-353-1965, Email: LSlater@andromeda.rutgers.edu

ABSTRACT

We performed a study of the sensitivity of electrical imaging to geochemical alteration of a zerovalent iron permeable reactive barrier (PRB) over time. Complex resistivity measurements on laboratory cores from an operational PRB defined the electrical properties of both unreacted and geochemically altered (reacted) iron as well as the growth rate of the reacted front on the up-gradient edge of the barrier. Laboratory results were used to generate models of the electrical structure of the PRB at 0, 15 and 30 years of operation. Synthetic cross-borehole resistivity and induced polarization data were generated and perturbed with errors representative of noise at the site. In order to generate reliable images of the engineered structure, a complex resistivity inversion was employed with a 'disconnect' in the regularization between the part of the finite element mesh (FEM) representing the internal structure of the barrier and the remainder of the FEM mesh. Synthetic results show that, although the internal structure of inverted images at 15 and 30 years does not accurately reflect the width of the reacted front modeled along the up-gradient edge of the barrier, perturbations to the internal structure of the imaged PRB are diagnostic of the growth of the reacted front. Cross-borehole electrical data obtained at the field site over a 15 month period demonstrate that the complex resistivity algorithm can reliably resolve the PRB target. Both resistivity and induced polarization reciprocal errors are low and the induced polarization data highly repeatable over this period. Changes in the electrical properties of the PRB over time were small, but consistent with growth of a reacted front based on the synthetic study.

INTRODUCTION

The permeable reactive barrier (PRB) is an innovative *in-situ* technology for the remediation of chlorinated hydrocarbon, heavy metal or radionuclide contaminated groundwater (Gilham and O'Hannesin, 1994; Gu et al., 1998; Vogan et al., 1999). The reactive material of the barrier participates in a redox reaction with the contaminant, resulting in the conversion of the contaminant into inorganic, non-toxic compounds. The reactive zerovalent iron (Fe^0) barrier is the most established PRB technology for the *in situ* remediation of chlorinated solvents, as well as heavy metals. As an example, degradation of trichloroethylene (TCE) by Fe^0 is generally assumed to result in ethene and chloride as the primary end products (Gavaskar et al., 1998).

As of 2002, eighty Fe^0 barriers were identified as operating worldwide (Carey et al., 2002). Although many of these barriers currently meet design specifications, concern exists regarding long-term (decade scale) performance reduction as a result of oxidation and precipitation at the zerovalent iron (Fe^0) surface (Liang et al., 2000; Phillips et al., 2000; Furukawa et al., 2002; Kohn et al., 2005), as well as clogging of the pore space (Mackenzie et al., 1999). Laboratory and field experiments have investigated the nature of, and rates of, corrosion, precipitation and/or clogging in Fe^0 barriers (Gu et al., 1999; Liang et al., 2000; Phillips et al., 2000; Furukawa et al., 2002; Klausen et al., 2003; Liang et al., 2003; Kohn et al., 2005). It is well recognized that field-scale technologies are required to monitor and provide warning of performance reduction, permitting remedial measures to reduce contaminant concentrations at locations down-gradient from the barrier site.

Previous workers have recognized the potential of geophysical tools to assist in the investigation of PRBs installed at contaminated sites. Geophysical imaging methods can potentially provide *in situ* information on the internal properties of the barrier without compromising the integrity of the engineered structure. Joesten et al. (2001) conducted cross-hole radar imaging of pilot-scale testing of a hydraulic fracture method of PRB installation in unconsolidated sediments at depth. Cross-hole radar amplitude measurements between fourteen boreholes were combined to define variability in cross-sectional amplitude attenuation along the length of the two walls. Small scale structures were tentatively interpreted as stringers of iron possibly attributable to iron particles moving into higher permeability formations. More recently, Slater and Binley (2003) describe an application of electrical imaging at a Fe^0 PRB installation in Kansas City, Missouri. They showed that electrical imaging could visualize the structure of this PRB after installation. Variations in electrical images along the length of the barrier were interpreted as evidence for flaws originating during the construction and emplacement of the barrier.

The focus of this paper is to expand upon a concept noted by Slater and Binley (2003), being that electrical imaging might be used to monitor the long-term health of a permeable reactive barrier. The basis of this argument is that corrosion/precipitation and/or clogging will alter the electrical properties of the PRB. Slater et al. (2005) reported laboratory experiments on Fe^0 columns in support of this concept; the complex conductivity of Fe^0columns showed a significant change (increase in both real and imaginary parts of the complex conductivity) following precipitation of iron hydroxides and iron carbonates (see FIGURE 7 of Slater et al., 2005). In this paper, we utilize the results of laboratory geochemical and geophysical measurements on cores obtained from the Kansas City PRB to determine the likely changes in the electrical properties of this barrier associated with alteration of the iron surface

over time. This information is used to generate synthetic realizations of the modified PRB structure upon installation and at fifteen and thirty years after completion. These datasets are inverted using a regularization constraint that satisfies the structure of the PRB (from design specifications) and results in plausible geophysical images of the electrical changes inside the PRB with time. The synthetic runs are compared with the results of 15 months of monitoring at the Kansas City site.

ELECTRICAL IMAGING

Tomographic electrical imaging is an established technology for visualizing the geoelectrical structure of the subsurface (see as examples, Daily and Owen, 1991; Park and Van, 1991; Shima, 1992; Oldenburg and Li, 1994; LaBrecque et al., 1996). Numerous environmental applications of the technology are reported, including monitoring of leaks from underground storage tanks (Ramirez et al., 1996), detection of unexploded ordinance (Daily et al., 2000) and imaging hydraulic barriers (Daily and Ramirez, 2000). Apparent conductivity and IP measurements are made for a large number of sets of four electrodes placed in boreholes or at the surface. Given these measurements, it is possible to solve numerically for conductivity and IP distributions that result in a set of calculated measurements best fitting with the measured response. The numerical calculations involve 2-D or 3-D forward modeling (in this work using the finite element (FE) method). In the case of a 2-D model, it is implicitly assumed that the electrical structure in the third dimension is constant. A 2-D model was used in this study as the barrier essentially represents a 2-D target at the image planes shown in FIGURE 1 (i.e. the cross-sectional PRB structure is continuous along the length of the barrier).

The inversion algorithm utilized in this study is based on an Occam's type procedure (de Groot Hedlin and Constable, 1990) with one significant modification (noted below). To perform the IP inversion, we utilize a complex conductivity algorithm first outlined by Kemna and Binley (1996) and described in detail by Kemna (2000). This algorithm requires measurements of conductivity magnitude ($|\sigma|$) and ϕ as input data. However, due to the equivalence between field and normalized IP parameters we can substitute field measures of M for ϕ, obtaining images of ϕ and imaginary conductivity scaled by a constant (for full details see Slater and Binley, 2003). Inversion of the ratio of two electrical datasets scaled by a numerical forward solution based on a homogeneous model is a technique for imaging changes over time that avoids the large propagation of error resulting when inverted datasets from two times are directly subtracted (e.g. Slater et al., 2000). This ratio approach was applied here.

In this work we incorporate a regularization constraint to satisfy the structure of the PRB (from design specifications) and help the inversion to find plausible geophysical images of the internal structure of the PRB at different times. The outline of the barrier (FIGURE 2) is used to define a 'disconnect' in the regularization (spatial smoothing) between the part of the finite element mesh (FEM) representing the internal structure of the barrier and the remainder of the FEM mesh. This means that the regularization (essential for stability of the inversion) does not introduce any smoothing across the boundary of the barrier. Therefore, the values of the inversion parameters representing the internal structure of the barrier cannot be influenced (through the regularization) by the values of the inversion parameters making up the remainder of the image. We note that the effectiveness of this approach relies on accurate ground-truth information on the shape of the barrier i.e. that the design specifications were achieved during installation. This is justified here as we are concerned with imaging changes in the internal properties of an established structure over time.

STUDY SITE

The PRB under study was installed in April 1998 at the U.S. Department of Energy's Kansas City Plant in Kansas City, MO (DOE, 2003). It was designed to remediate 1,2-dichloroethylene (1,2-DCE) and vinyl chloride (VC) in contaminated groundwater migrating from the facility. FIGURE 1 is a plan view of the site showing the outline of the PRB, location of electrical imaging boreholes (BH), vertical and angle coring locations and groundwater monitoring wells. The PRB was constructed as a continuous 40 m (130 ft) long, 1.8 m (6 ft) wide trench. FIGURE 2 shows a cross-sectional view of the barrier geometry, site geology and the location of electrodes in the plane BH4-BH1-BH5. Alluvial sediments underlie the site, primarily silty clay overlying basal gravel. These alluvial sediments are underlain by bedrock shale. The PRB was constructed by filling the first 1.8 m (6 ft) of the trench with 100 % zerovalent granular iron such that the base of this section was in contact with bedrock. The remainder of the trench was then filled with 0.6 m (2 ft) of zerovalent iron and 1.2 m (4 ft) of sand (FIGURE 2). The thicker lower unit was designed to compensate for the higher flow-through velocities associated with hydraulically conductive basal gravel that rests on bedrock (FIGURE 2).

The performance of the Kansas City PRB has been adversely affected by alteration to groundwater flow within the vicinity of the PRB resulting from the installation of the PRB structure itself (DOE, 2003). Hydraulic head measured at the network of twenty-seven monitoring wells at the site (FIGURE 1) shows that flow is bypassing the southern end of the barrier (FIGURE 1). This is supported by geochemical measurements that show incomplete reduction of organic compounds in monitoring wells on the outflow side of the barrier towards its southern end (DOE, 2003). These issues

influenced the design of the electrical imaging experiments conducted at the site. Twelve electrode arrays were installed at the site during January 2003. Boreholes (BH) 1-7 were installed at the location where groundwater flow through the barrier is concentrated and the greatest changes in electrical properties should be expected. BH4-BH1-BH5 defines the primary 2D image plane for monitoring; the additional boreholes were installed at this site to test imaging of the barrier structure in three dimensions. A second 2D image plane (BH8-BH10-BH9) was established for comparative purposes towards the southern end of the barrier where groundwater flow through the PRB is reduced. Image plane BH11-BH12 was established as a control off the barrier.

Each borehole consisted of twenty electrodes spanning the height of the barrier plus one electrode placed at the ground surface. Boreholes 1 and 10 were drilled at the center of image planes BH4-BH1-BH5 and BH8-BH10-BH9 and therefore penetrate the lower segment of the PRB (FIGURE 2). Lead electrodes were used in this study. Ideally, we would have used a non-polarizing electrode such as a Pb-PbCl junction but excessive costs and awkward implementation in boreholes ruled against this approach. Regular metal electrodes can give IP measurements of similar quality to that obtained with metal-electrolyte junction electrodes when the instrumentation (such as used here) incorporates data processing to remove electrode polarization at the potential electrodes (Dahlin et al., 2002). Reciprocity checks reported later testify to high data quality achieved with these electrodes. Electrical measurements were made on image planes BH4-BH1-BH5 and BH8-BH10-BH9 on seven occasions over a twenty-nine month period (January 03, July 03, November 03, March 04, July 04, January 05 and May 05). Measurements utilizing additional electrode pairs were made less frequently; measurements on control panel BH11-BH12 were obtained on three occasions (July 03, November 03 and May 05).

SUPPORT DATA

Immediately following completion of the May 05 dataset, vertical and angle borings were conducted at the site in an effort to retrieve samples of zerovalent iron for geochemical and geophysical laboratory analyses. The primary objective was to determine the width of the reacted zone on the up-gradient edge of the barrier and its electrical signature relative to unreacted zerovalent iron. Three vertical borings were conducted at the up-gradient edge of the barrier at the locations shown in FIGURE 1. Six angle borings (the angle of the drill bit was 30± from vertical) were also conducted (locations in plan again shown in FIGURE 1). The angle borings provided a sequence of core through the up-gradient interface of the barrier and into its center.

Laboratory analyses were conducted on angle borings (AB) 1, 5 and 6 as the cores retrieved from AB 2-4 were cut close to the up-gradient interface, preventing accurate laboratory electrical measurements on this critical section of the core. The laboratory measurements included (1) complex conductivity measurements from 0.1-1000 Hz of 3 cm sections along the core; (2) scanning electron microscopy (SEM) imaging of samples along the core; (3) x-ray diffraction measurements along the core; (4) sulfur and carbonate analysis along the core. The details of this laboratory work form the focus of a paper in preparation. However, we report here three important findings required to conduct our synthetic modeling. Ideally, we would illustrate results for AB 1 as it is the closest (of the three cores analyzed) to our primary image plane. However, we show results obtained for AB 5 as AB 1 contained an anomalous zone of sand at about 20 cm into the core (results obtained for AB 6 are consistent with AB 5).

Firstly, SEM images confirm the presence of a reacted zone developing from the up-gradient edge of the Kansas City PRB. FIGURE 3a shows an SEM image for a sample extracted 50 cm (i.e. towards the end) along AB 5 (FIGURE 2). The image is consistent with unreacted zerovalent iron within the barrier and away from the up-gradient edge. FIGURE 3b shows the SEM image for sample extracted at 7.5 cm along PRB 5. Here the SEM image reveals heavy precipitates formed on the iron surface. The results of X-ray diffractometry, as well as the hexagonal platelet structure observed with SEM here, suggest that these precipitates are a mixture of green rusts (a mineral phase of mixed Fe^{2+}/Fe^{3+} oxy (hydroxide) layers with anions (i.e. Cl^-, CO_3^{2-}, SO_4^{2-}) incorporated into inner-layer spaces) and iron oxhydroxides. Such minerals have been identified as precipitates in other zerovalent iron barriers (Legrand et al., 2001; Su and Puls, 2004).

Secondly, complex conductivity data illustrate the magnitude of change in electrical measurements that can be expected as a result of the mineralogical alteration identified in FIGURE 3. FIGURE 4 shows the complex conductivity response from 0.1-1000 Hz at two locations along AB 5: (a) SIP1 is within the reacted zone, 7.5 cm from the up-gradient interface and coincident with the location of SEM1; (b) SIP2 is from deeper within the barrier (50 cm from the up-gradient interface), coincident with SIP2 and representing unreacted zerovalent iron. Both samples were fully re-saturated with site groundwater (σ_w = 0.81 mS/cm); in each case the sample length is 3 cm and the sample diameter is 2.14 cm. These measurements show that the mineralogical alteration in the reacted zone increases the real and imaginary parts of the complex conductivity. Results obtained on AB 6 confirm this finding; furthermore we have observed similar changes in laboratory cores treated with synthetic groundwater to induce accelerated ageing (Slater et al., 2005). Modeling of these complex conductivity datasets and

detailed discussion of the electrochemical mechanisms causing the increase in complex conductivity is the subject of a separate paper. For our current work, we are most interested in defining the likely change in the measured real and imaginary conductivity at low frequencies (representative of single frequency, field-scale induced polarization measurements) as a result of the mineralogical alteration associated with ageing. Arbitrarily assigning a 1 Hz measurement frequency, FIGURE 4 shows that the real conductivity increases by approximately one order of magnitude from 0.1 S/m to 1.0 S/m and the imaginary conductivity increases from about 0.04 S/m to about 0.1 S/m within the reacted zone.

Thirdly, the angle borings were used to assess the width of the reacted zone at the Kansas City barrier. From SEM analyses and visual inspection of the bores, the average horizontal width of the reacted zone at the time of sampling in May 2005 was found to be approximately 10 cm.

SYNTHETIC STUDIES

FIGURE 5 shows three synthetic models and corresponding inversion results designed to test our concept of long-term monitoring of PRBs for signs of reduced barrier performance based on the KC PRB. The structure (outline) of the barrier is based on the PRB design specifications given in FIGURE 2. Representative values for σ' and σ'' within the barrier are derived from the laboratory measurements on the angle borings discussed previously. Using FIGURE 4, we assigned $\sigma' = 0.1$ S/m and $\sigma'' = 0.05$ S/m for unreacted Fe^0 saturated with *in situ* groundwater. We assigned the respective values for the reacted front at the up-gradient edge of the barrier as $\sigma' = 1.0$ S/m and $\sigma'' = 0.1$ S/m (again from FIGURE 4). The width of the reacted front forming on the up-gradient edge of the barrier was calculated based on our laboratory observation that the reacted front at the KC PRB is

approximately 10 cm wide after 8 years of operation. We assumed a constant rate of propagation of this reacted front to model the barrier at time (t) = 0 yrs (FIGURE 5a), t = 15 yrs (FIGURE 5b) and t = 30 yrs (FIGURE 5c) after inception. These times were selected to represent the long-term (decadal) scale of anticipated PRB operation (Gavaskar et al., 1998).

All inversions were performed on synthetic data based on the measurement scheme that was applied in the field monitoring at the Kansas City site. The complete dataset consisted of 3744 measurements in which current and voltage dipoles were split between BH4, BH1 and BH5 (1248 measurements using BH4-BH1, 1248 measurements using BH1-BH5 and 1248 measurements using BH4-BH5). In order to make the synthetic tests as consistent with the field data as possible, we used only the measurements that were retained in the field dataset after removal of outliers based on strict reciprocity criteria (defined in the following section). The dataset was also filtered to remove any measurement configurations characterized by a greater than 2% error in a forward model calculation for a homogenous medium. The final dataset consisted of 2223 measurements that were contaminated with random noise representative of error levels encountered in the retained field data, being a standard deviation of 0.05 (fractional error) in the resistance and a standard deviation of 1 mV/V (absolute error) in the chargeability.

FIGURE 5a illustrates that the unreacted, homogeneous Kansas City PRB at the time of installation is well resolved by the inversion. The real and imaginary conductivity images both accurately reproduce the model structure and the inverted images are devoid of significance artifacts. The inversion is unable to accurately resolve the heterogeneous PRB modeled at t = 15 yrs and artifacts appear in the inverted image. Considering first the σ' image, the 20 cm wide strip (σ' = 1.0 S/m)

representing the reacted zone on the up-gradient edge of the barrier is imaged as an approximately 80 cm wide strip of variable σ' (approximately 0.2-0.4 S/m). No evidence for the reacted zone (σ'' = 0.1 S/m) is apparent in the σ'' image. Both the σ' and σ'' images at t = 15 yrs contain artifacts whereby high values representative of the PRB are reconstructed immediately outside of the PRB structure. The results at t = 30 yrs are similar to those at t = 15 yrs except that the wider (40 cm) strip representing the reacted front in the model results in higher σ' (approximately 0.2-0.6 S/m) in the approximately 80 cm wide strip reconstructed by the inversion. Again, evidence for the reacted front is absent in the σ'' inversion. Artifacts, whereby high values representative of the PRB are reconstructed immediately outside of the PRB structure, are suppressed relative to those in FIGURE 5b. Artifacts along the up-gradient edge just inside the PRB (lower σ'') appear in the σ'' image.

FIELD STUDIES

The measurement scheme used in the field monitoring was described in the previous section. The current waveform used consisted of 1 s injection/1 s off cycle; the chargeabilty was calculated from the integral of the decay curve between 0.02 s and 0.83 s during the off cycle. We limit ourselves to presentation of results from image plane BH4-BH1-BH5 as changes over the duration of the monitoring period are very small but most pronounced on this image plane where flow through the barrier is focused (FIGURE 1). FIGURE 6 (a-b) and (d-e) shows histograms of the resistance and chargeability reciprocal errors (after removal of outliers in the data) in the March 04 and May 05 datasets for image plane BH4-BH1-BH5 respectively. Outliers were defined based on the following criteria: (1) measurements that exceed a 0.05 fractional resistance error; (2) for chargeability less than 10 mV/V measurements that exceed an absolute error of 1 mV/V; (3) for chargeability greater than 10

mV/V measurements that exceed a fractional error of 0.1. The resistance errors in FIGURE 6 are plotted as a fractional error whereas the IP errors are plotted as absolute values of chargeability. The mean (μ) and standard deviation (σ_d) of the datasets calculated assuming a normal distribution (superimposed on the data in FIGURE 6) are shown as annotations on the histograms plotted in FIGURE 6. These plots indicate that 95% of the measurements in the March 04 and May 05 datasets have a fractional resistance error less than or equal to 0.016 and an absolute chargeability error less than or equal to 0.98 mV/V. FIGURE 6 also shows the differences in the resistance (FIGURE 6c) and chargeability (FIGURE 6f) measurements between the March 04 and May 05 datasets (for all common measurements). The scale of FIGURE 6c is different to that of FIGURES 6a and b as the difference between the datasets is significantly greater than the reciprocal errors within the individual datasets. Approximating the normal distribution, 60% of the fractional differences between the resistance datasets exceed 0.016. However, the differences in the chargeability measurements between the two datasets are not significantly greater than the reciprocal errors within each dataset (compare histogram and normal distribution statistics for FIGURE 6f with those of Figure 6d and e).

Noise parameters in the inversion were again specified as a standard deviation of 0.05 (fractional error) in the resistance and a standard deviation of 1 mV/V (absolute error) in the chargeability. Inverted electrical images for the field data are shown in FIGURE 7. The complex conductivity inversion for the March 2004 dataset is shown as (a) phase angle (FIGURE 7a), and (b) real and imaginary parts of the complex conductivity (FIGURE 7b). As previously explained, there is a linear scaling applied to σ'' and ϕ images here due to the use of chargeability in the complex inversion. The PRB structure is generally well resolved by the inversion although an artifact exists outside of the barrier between 3 and 6 m depth towards the center of the image plane. All three electrical parameters

reveal a generally uniform PRB structure, although there is greater variation in the σ' than σ'' inside the barrier.

FIGURE 7c shows a ratio image in terms of a percentage change in real conductivity between the May 2005 and March 2004 datasets. A positive percentage change indicates an increase in conductivity in May 2005 relative to March 2004. As shown in FIGURE 6, the differences in the phase between these two times (FIGURE 6f) are not significantly greater than the errors within each dataset (FIGURE 6d and 6e). Consequently a ratio image for the imaginary conductivity is not shown. The small difference between the measured resistances for the two datasets (FIGURE 6c) is manifested as a slight increase in real conductivity (less than 10%) that is focused within the uppermost section of the barrier on its up-gradient side.

DISCUSSION AND CONCLUSIONS

Our synthetic studies guided by laboratory measurements on cores of the Kansas City PRB illustrate that it is feasible to use electrical imaging as a long-term, non-invasive monitoring tool for detecting precipitation that typically causes barrier performance reduction. The 15 and 30 year simulations conducted here reveal that it is not possible to accurately resolve the geometry of the reacted front that develops on the up-gradient face of the barrier as it is too thin. However, there is a detectable anomaly in the image structure inside the barrier that essentially represents a blurred (smoothed) depiction of the model for the reacted front.

Our field studies demonstrate how well the structure of the PRB is resolved when using a 'disconnect' in the regularization between the part of the finite element mesh (FEM) representing the internal structure of the barrier and the remainder of the FEM mesh. The inverted field data produce a surprisingly uniform PRB structure with only minor artifacts. This regularization disconnect is critical to accurately resolving the PRB structure. Without this constraint, the inversion is unable to accurately resolve the image structure, particularly in the phase data. For the sake of brevity we have not shown images obtained without this disconnect threshold. However, such images are shown in our earlier work on the same barrier (Slater & Binley, 2003, FIGURES 5 & 7). This disconnect method is similarly appropriate for imaging other types of engineered structures such as containment walls or buried tanks where the outline of the engineered structure is precisely known and internal variability is of interest.

Predictably, the field data show little evidence for change in the electrical properties of the PRB over our limited monitoring period. Laboratory measurements on cores from the PRB indicate that the 14 month sampling interval in the field is too small to expect any significant growth in the reacted front that would be detectable with electrical imaging. However, it is interesting to note that ratio images do show a small increase in conductivity inside the PRB with time (over 14 months) that occurs at a location consistent with where the synthetic images exhibit changes when modeling a reacted front on the up-gradient edge of the PRB (compare FIGURES 5 and 7). It is also noteworthy that the laboratory and field results both suggest that changes in the real conductivity due to development of a reacted front are greater than changes in imaginary conductivity. The increase in real conductivity is attributed to an increase in electronic conduction through the granular iron mix that develops as a result of the extensive iron mineral precipitation exhibited in FIGURE 3b. This implies

that resistivity imaging alone may be sufficient for long term monitoring of precipitation leading to reduced PRB performance.

It is still often assumed that induced polarization measurements can only be made using non polarizing electrodes composed of a metal in contact with an electrolyte of the same metal. Our error analyses and repeat measurements over a 15 month period show that it is possible to obtain surprisingly high quality IP data from fieldscale cross-borehole surveys using simple metal (in this case lead) electrodes. This high accuracy in the IP measurement is obtained as the resistivity instrument employed has high input impedance and incorporates signal processing to estimate and remove electrode polarization at the potential electrodes prior to current injection. Simple metal electrodes are readily deployed in cross-borehole studies and are more amenable to long term monitoring applications. We consider the present constraints on adopting electrical imaging for long-term monitoring to include such issues as long-term durability of the deployed electrode arrays and long-term electrode stability under changing geochemical conditions. Other factors include adequately accounting for changes in aqueous geochemistry that may occur over decadal timescales thus affecting the electrical measurements.

In summary, we conclude that electrical imaging is a viable technology for monitoring the long-term (decadal) scale changes in the electrical properties of a PRB that result from corrosion and precipitation. As precipitation is a major cause of performance reduction, electrical imaging thus appears a viable technology for detecting and/or predicting when the PRB will fail to meet design standards for contaminant treatment. As over eighty PRBs are now in operation worldwide, application of this geophysical technology could have a significant impact on groundwater cleanup operations.

REFERENCES

Carey, M. A., B. A. Fretwell, N. G. Mosley and J. W. N. Smith, 2002, Guidance on the design, construction, operation and monitoring of permeable reactive barriers, NC/01/51, Environment Agency, Bristol, UK.

Dahlin, T., V. Leroux and J. Nissen, 2002, Measuring techniques in induced polarisation imaging: Journal of Applied Geophysics, **50**, 279-298.

Daily, W. and E. Owen, 1991, Cross-borehole resistivity tomography: Geophysics, **56**,1228-1235.

Daily, W. and A. Ramirez, 2000, Electrical imaging of engineered hydraulic barriers: Geophysics, **65**, 83-94.

Daily, W., Ramirez, A., Newmark, R. and V. George, 2000, Imaging UXO using electrical impedance tomography: Journal of Environmental & Engineering Geophysics, **5**, 11-24.

de Groot Hedlin, C. and S. Constable, 1990, Occam's inversion to generate smooth, two dimensional models from magnetotelluric data: Geophysics, **55**, 1613-1624.

DOE, 2003, Annual Groundwater Corrective Action Report, United States Department of Energy (DOE), Kansas City Office, Kansas City Missouri. Honeywell Federal Manufacturing & Technologies.

Furukawa, Y., Kim, J. W., Watkins, J. and R. T. Wilkin, 2002, Formation of ferrihydrite and associated iron corrosion products in permeable reactive barriers of zero-valent iron: Environmental Science & Technology, **36**, 5469-5475.

Gavaskar, A. R., Gupta, N., Sass, B. M., Janosy, R. J. and D. O'Sullivan, 1998, Permeable reactive barriers for groundwater remediation, Batelle Press, Columbus.

Gilham, R. W. and S. F. O'Hannesin, 1994, Enhanced degradation of halogenated alophatics by zero valent iron: Ground Water, **32**, 958-967.

Gu, B., Liang, L., Dickey, M. J., Yin, X. and S. Dai, 1998, Reductive precipitation of uranium(VI) by zero-valent iron: Environmental Science & Technology, **32**, 3366-3373.

Gu, B., Phelps, T. J., Liang, L., Dickey, M. J., Roh, Y.. L. Kinsall, B. L., Palumbo, A. V. and G. K. Jacobs, 1999, Biogeochemical dynamics in zero-valent iron columns: Implications for permeable reactive barriers: Environmental Science & Technology, **33**, 2170-2177.

Joesten, P. K., Lane, J. W., Savoie, J. G. and Versteeg, R. J., 2001, Application of borehole-radar methods to image two permeable reactive-iron walls at the Massachusetts Millitary Reservation, Cape Cod: Massachusetts, Proceedings of the Symposium on the Application of Geophysics to Engineering and Environmental Problems (SAGEEP), 10pp.

Kemna, A, 2000, Tomographic inversion of complex resistivity - theory and application: Der Andere Verlag, Osnabrück, Germany.

Kemna, A. and A. Binley, 1996, Complex electrical resistivity tomography for contaminant plume delineation: Proceedings of the 2nd Meeting of Environmental and Engineering Geophysics, 196-199.

Klausen, J.,. J. Vikesland, P. J., Kohn, T., Burris, D. R., Ball, W. P. and A. L. Roberts, 2003, Longevity of granular iron in groundwater treatment processes: Solution composition effects on reduction of organochlorides and nitroaromatic compounds: Environmental Science & Technology, **37**, 1208-1128.

Kohn, T., Livi, K. J. T., Roberts, A. L. and P. J. Vikesland, 2005, Longevity of granular iron in groundwater treatment processes: corrosion product development: Environmental Science & Technology, **39**, 2867-2879.

LaBrecque, D. J., Miletto, M., Daily, W. Ramirez, A. and E. Owen, 1996, The effects of noise on Occam's inversion of resistivity tomography data: Geophysics, **61**, 538-548.

Legrand, L., Abdelmoula, M., Gehin, A., Chausse, A. and J. M. R. Genin, 2001, Electrochemical formation of a new Fe(II)-Fe(III) hydroxy-carbonate green rust: characterisation and morphology: Electrochimica Acta, **46**, 1815-1822.

Liang, L. Y., Korte, N., Gu, B. H., Puls, R. and C. Reeter, 2000, Geochemical and microbial reactions affecting the long-term performance of in situ 'iron barriers': Advances in Environmental Research, **4**, 273-286.

Liang, L. Y., Sullivan, A. B., West, O. R., Moline, G. R. and W. Kamolpornwijit, 2003, Predicting the precipitation of mineral phases in permeable reactive barriers: Environmental Engineering Science, **20**, 635-653.

Mackenzie, P. D., D. P. Horney and T. M. Sivavec. 1999. Mineral precipitation and porosity losses in granular iron columns: Journal of Hazardous Materials, **68**, 1-17.

Oldenburg, D. W. and Y. Li, 1994, Inversion of induced polarization data: Geophysics, **59**, 1327-1341.

Park, S. K. and G. P. Van, 1991, Inversion of pole-pole data for 3-d resistivity structure beneath arrays of electrodes: Geophysics, **56**, 951-960.

Phillips, D. H., B. Gu, D. B. Watson, Y. Roh, L. Liang, and S. Y. Lee, 2000, Performance evaluation of a zerovalent iron reactive barrier: Mineralogical characteristics: Environmental Science & Technology, **34**, 4169-4176.

Ramirez, A., W. Daily, A. Binley, D. LaBrecque, and D. Roelant, 1996, Detection of leaks in underground storage tanks using electrical resistance methods: Journal of Environmental & Engineering Geophysics, **1**, 189-203.

Shima, H, 1992, 2-D and 3-D resistivity image reconstruction using crosshole data: Geophysics **57**, 1270-1281.

Slater, A. Binley, W. Daily, and R. Johnson, 2000, Cross-hole ERT imaging of a controlled tracer injection: Journal of Applied Geophysics, **44,** 85-102.

Slater, L., and A. Binley, 2003, Evaluation of permeable reactive barrier (PRB) integrity using electrical imaging methods, Geophysics, **68**, 911-921.

Slater, L., J. Choi, and Y. Wu, 2005, Electrical properties of iron-sand columns: implications for induced polarization investigation and performance monitoring of iron-wall barriers: Geophysics, **70**, G87-G94.

Su, C., and R. Puls, 2004, Significance of Iron(II,III) hydroxycarbonate green rust in arsenic remediation using zerovalent iron in laboratory column tests: Environmental Science & Technology, **38**, 5224-5231.

Vogan, J. L., R. M. Focht, D. K. Clark, and S. L. Graham, 1999, Performance evaluation of a permeable reactive barrier for remediation of dissolved chlorinated solvents in groundwater: Journal of Hazardous Materials, **68**, 97-108.

FIGURE CAPTIONS

FIGURE 1: Plan view of Kansas City PRB site showing the outline of the PRB, location of electrical imaging boreholes (BH), 30± (from vertical) angle borings (with direction), vertical borings, groundwater monitoring wells and the approximate groundwater flow vector. BH11 and BH12 are located off the barrier and form a control image panel.

FIGURE 2: Cross-section of image plane BH4-BH1-BH5 showing the outline of the iron barrier as per design specifications, basic geology and position of electrodes (solid circles) used for electrical imaging. Each borehole (BH) contains 21 electrodes (including the electrode placed at the ground surface). Within the region bound by the borehole electrodes the size of the elements making up the finite element mesh used to model the electrical data is 0.2 m in the horizontal and 0.076 m in the vertical. Location of angle boring 5 in cross section also shown (note than angle boring 5 is offset 17 m south of this image plane).

FIGURE 3. Scanning electron microscopy (SEM) images from samples of angle boring 5 (a) SEM2 showing unreacted zerovalent iron sampled at 50 cm from the up-gradient interface (b) SEM1 showing core material from the reacted zone sampled 7.5 cm from the up-gradient interface showing heavy precipitates formed on the zerovalent iron surface (sample location coincident with core measurement location SIP1 in FIGURE 4). X-ray diffraction results (not reported here) and the hexagonal platelet structure observed with SEM suggest that the precipitates observed are a mixture of green rust and other iron oxide/hydroxides. Sample locations shown in cross-section in FIGURE 2.

FIGURE 4: Comparison of electrical measurements on angle boring (AB) 5 (a) within the reacted zone 7.5 cm from the up-gradient interface (SIP1), and (b) unreacted Fe0 (SIP2) from deeper within the barrier (50 cm from the up-gradient interface). Both cores were fully resaturated with site groundwater (σ_w = 0.81 mS/cm) prior to electrical measurements. The dashed line denotes the measurement frequency (1 Hz) used in the synthetic and field studies. The location of the measurements on AB 5 is shown in FIGURE 2.

FIGURE 5: Synthetic models and inversion results for the Kansas City PRB at (a) t = 0 yrs, (b) t = 15 yrs, and (c) t = 30 yrs for image plane BH4-BH1-BH5. The reacted zone is modeled as a thin strip forming on the up-gradient edge of the barrier (FIGURE 2). The width of the strip at t = 15 and t = 30 yrs was calculated based on analysis of angle borings extracted from the Kansas City PRB. The inverted noisy datasets were characterized by a standard deviation of 0.05 (fractional error) in the resistance and a standard deviation of 1 mV/V (absolute error) in the chargeability.

FIGURE 6: Histogram analysis of the reciprocal errors in the March 04 and May 05 datasets as well as the differences between the two datasets. The resistances are shown as fractional errors whereas the IP measurements are shown as absolute errors (a) March 04 resistance reciprocals (b) May 05 resistance reciprocals (c) difference in the resistances between the May 05 and March 04 datasets (d) March 04 IP reciprocals (e) May 05 IP reciprocals (f) difference in the IP measurements between the May 05 and March 04 datasets. The number of measurements (N), mean (μ), standard deviation (σ_d) and normal distribution are shown for each dataset. Note the difference in the scales in plot (c) relative to plots (a) and (b).

FIGURE 7. Results of electrical imaging measurements at the Kansas City PRB. The inversion of the March 2004 dataset (2223 measurements used) is shown as (a) phase, and (b) real (σ') and imaginary (σ'') conductivity. Part (c) shows an inversion for percentage changes in σ' in the May 2005 dataset relative to the March 2004 dataset (1993 measurements used). Field datasets were characterized by a standard deviation of 0.05 (fractional error) in the resistance and a standard deviation of 1 mV/V (absolute error) in the chargeability.

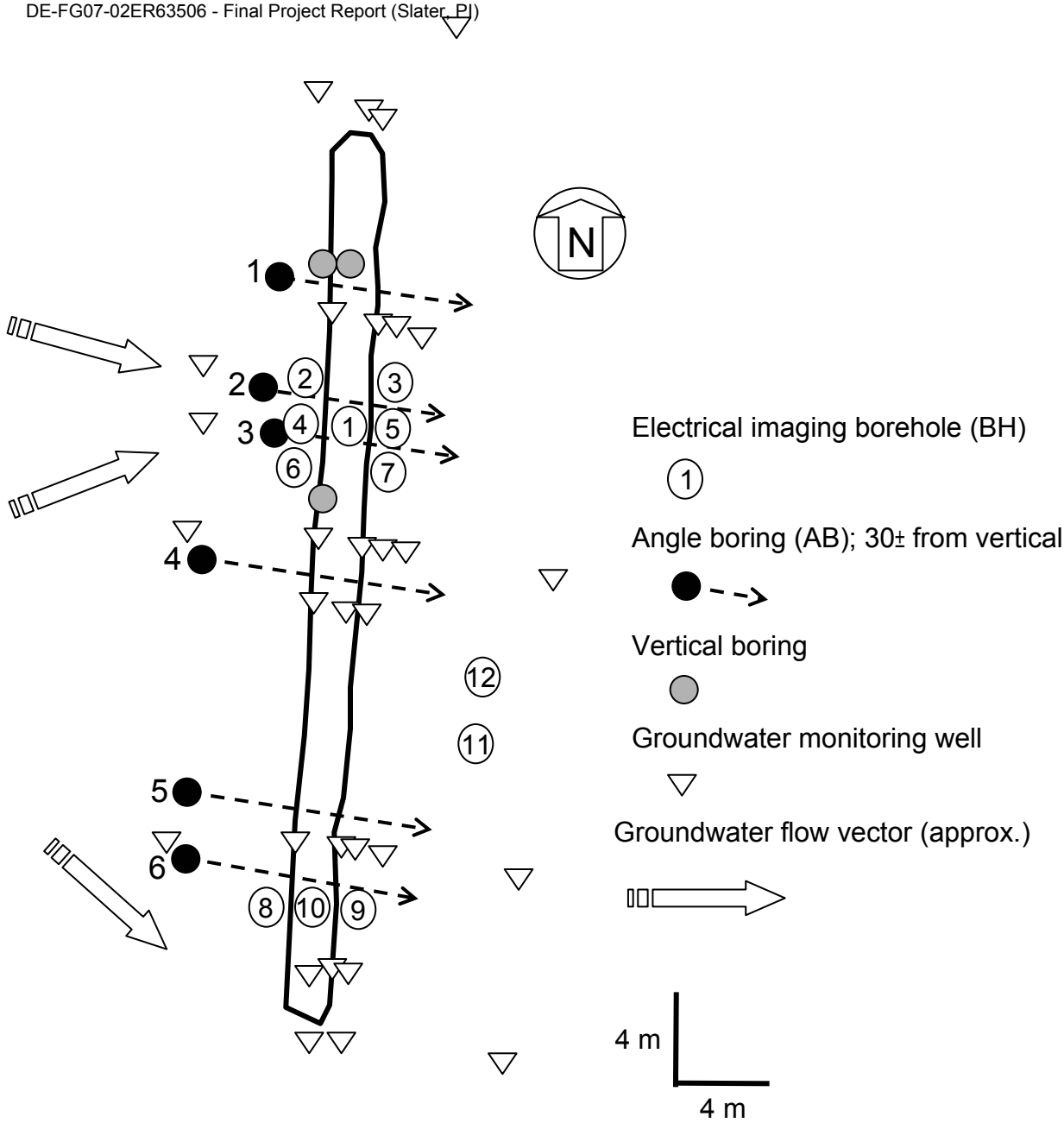

Figure 1: Plan view of Kansas City PRB site showing the outline of the PRB, location of electrical imaging boreholes (BH), 30± (from vertical) angle borings (with direction), vertical borings, groundwater monitoring wells and the approximate groundwater flow vector. BH11 and BH12 are located off the barrier and form a control image panel.

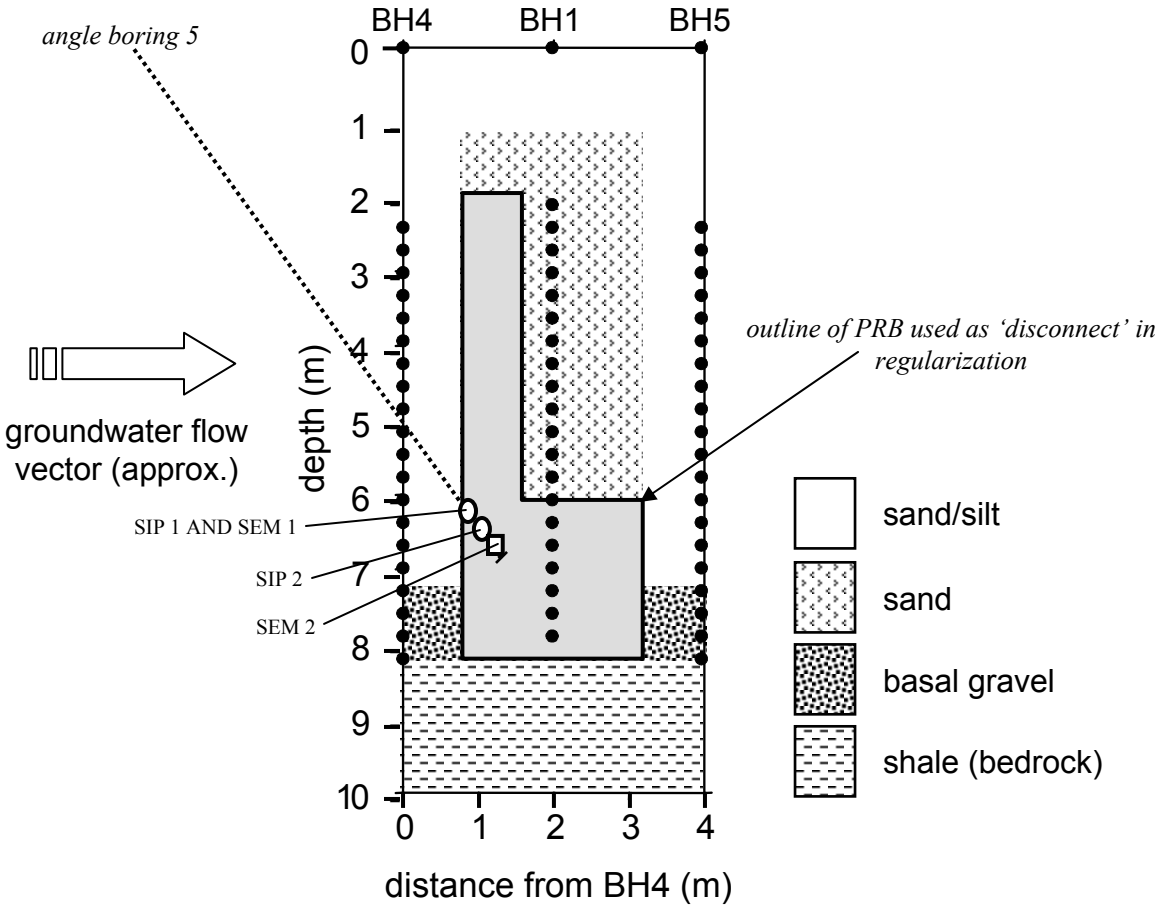

Figure 2: Cross-section of image plane BH4-BH1-BH5 showing the outline of the iron barrier as per design specifications, basic geology and position of electrodes (solid circles) used for electrical imaging. Each borehole (BH) contains 21 electrodes (including the electrode placed at the ground surface). Within the region bound by the borehole electrodes the size of the elements making up the finite element mesh used to model the electrical data is 0.2 m in the horizontal and 0.076 m in the vertical. Location of angle boring (AB) 5 in cross section also shown (note that AB 5 is offset 17 m south of this image plane)

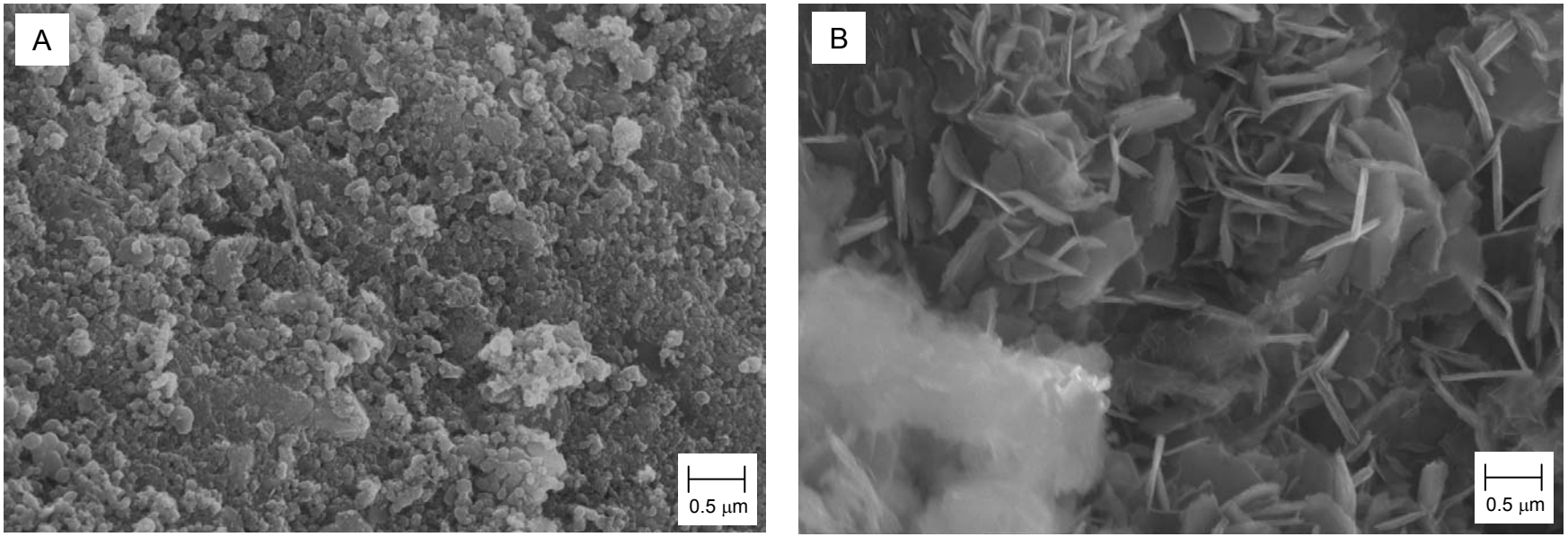

Figure 3. Scanning electron mrcroscopy (SEM) images from samples of angle boring 5 (a) SEM2 showing unreacted zero valent iron sampled at 50 cm from the upgradient interface (b) SEM1 showing core material from the reacted zone sampled 7.5 cm from the upgradient interface showing heavy precipitates formed on the zero valent iron surface (sample location coincident with core measurement location SIP1 in Figure 4). X-ray diffraction results (not reported here) and the hexagonal platelet structure observed with SEM suggest that the precipitates observed are a mixture of green rust and other iron oxide/hydroxides. Sample locations shown in cross-section in Figure 2.

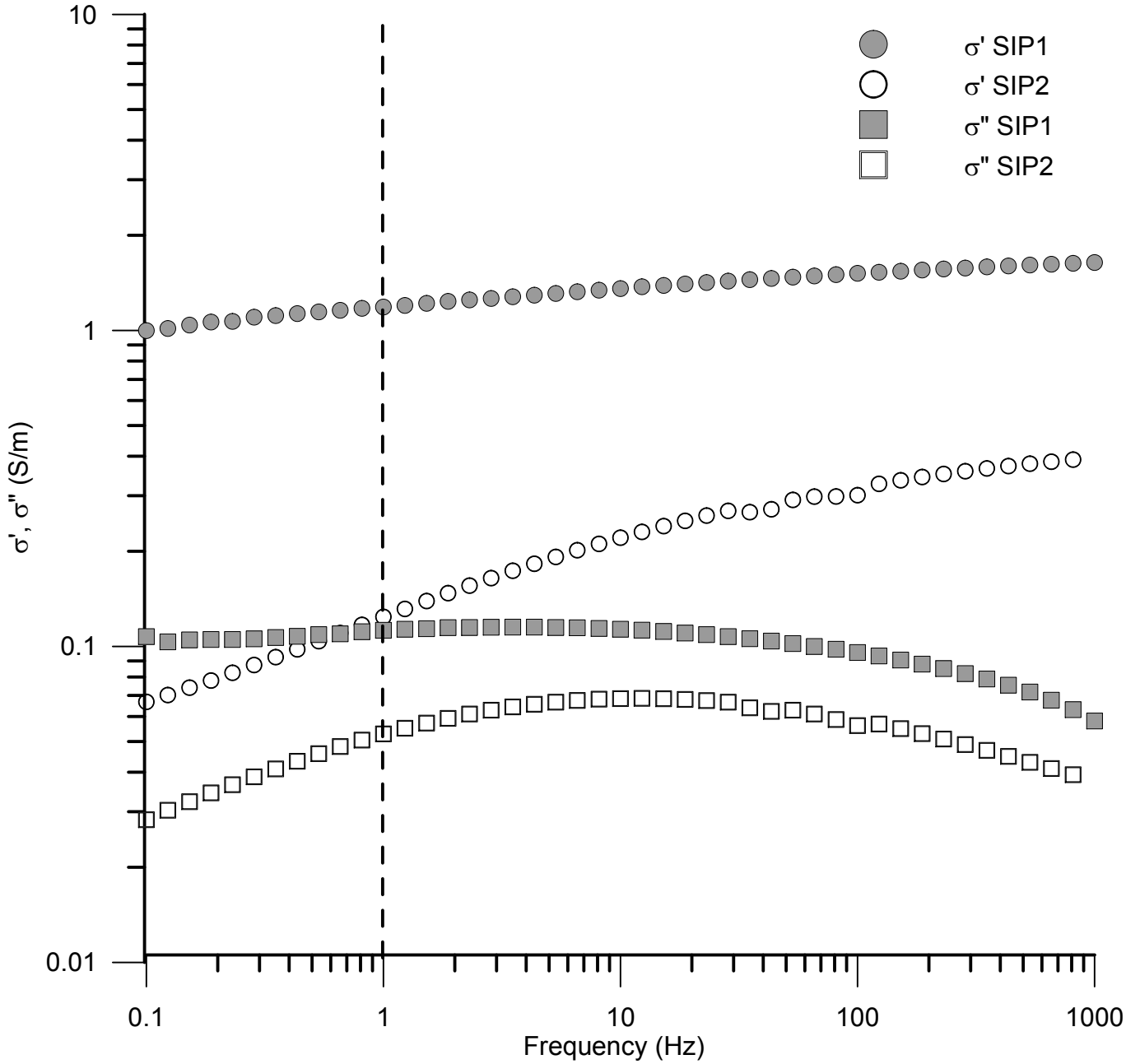

Figure 4: Comparison of electrical measurements on angle boring (AB) 5 (a) within the reacted zone 7.5 cm from the upgradient interface (SIP1), and (b) unreacted Fe^0 (SIP2) from deeper within the barrier (50 cm from the upgradient interface). Both cores were fully resaturated with site groundwater (s_w = 0.81 mS/cm) prior to electrical measurements. The dashed line denotes the measurement frequency (1 Hz) used in the synthetic and field studies. The location of the measurements on AB5 is shown in Figure 2.

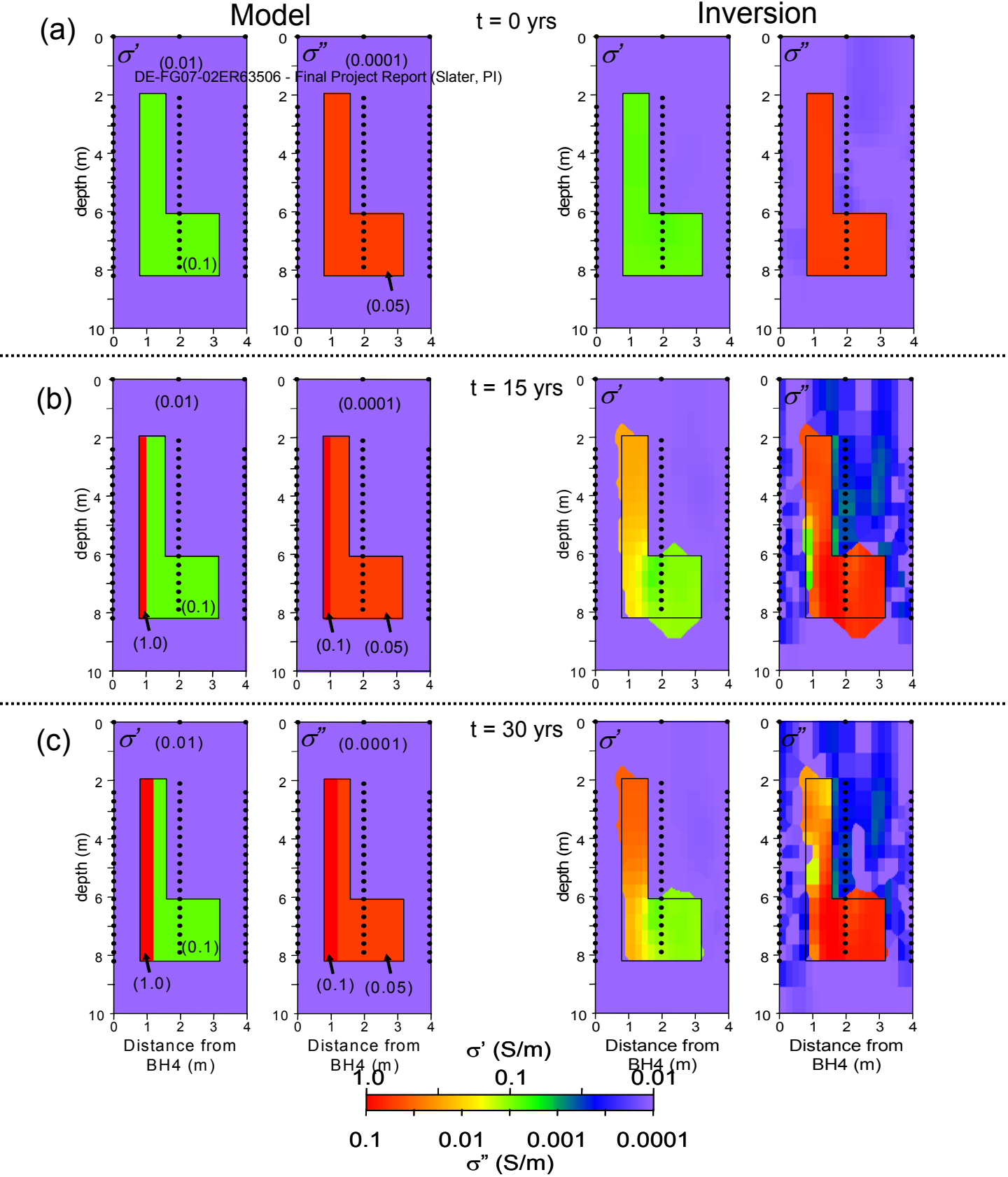

Figure 5: Synthetic models and inversion results for the Kansas City PRB at (a) t = 0 yrs, (b) t = 15 yrs, and (c) t = 30 yrs for image plane BH4-BH1-BH5. The reacted zone is modeled as a thin strip forming on the upgradient edge of the barrier (Fig. 2). The width of the strip at t = 15 and t = 30 yrs was calculated based on analysis of angle borings extracted from the Kansas City PRB. The inverted noisy datasets were characterized by a standard deviation of 0.05 (fractional error) in the resistance and a standard deviation of 1 mV/V (absolute error) in the chargeability.

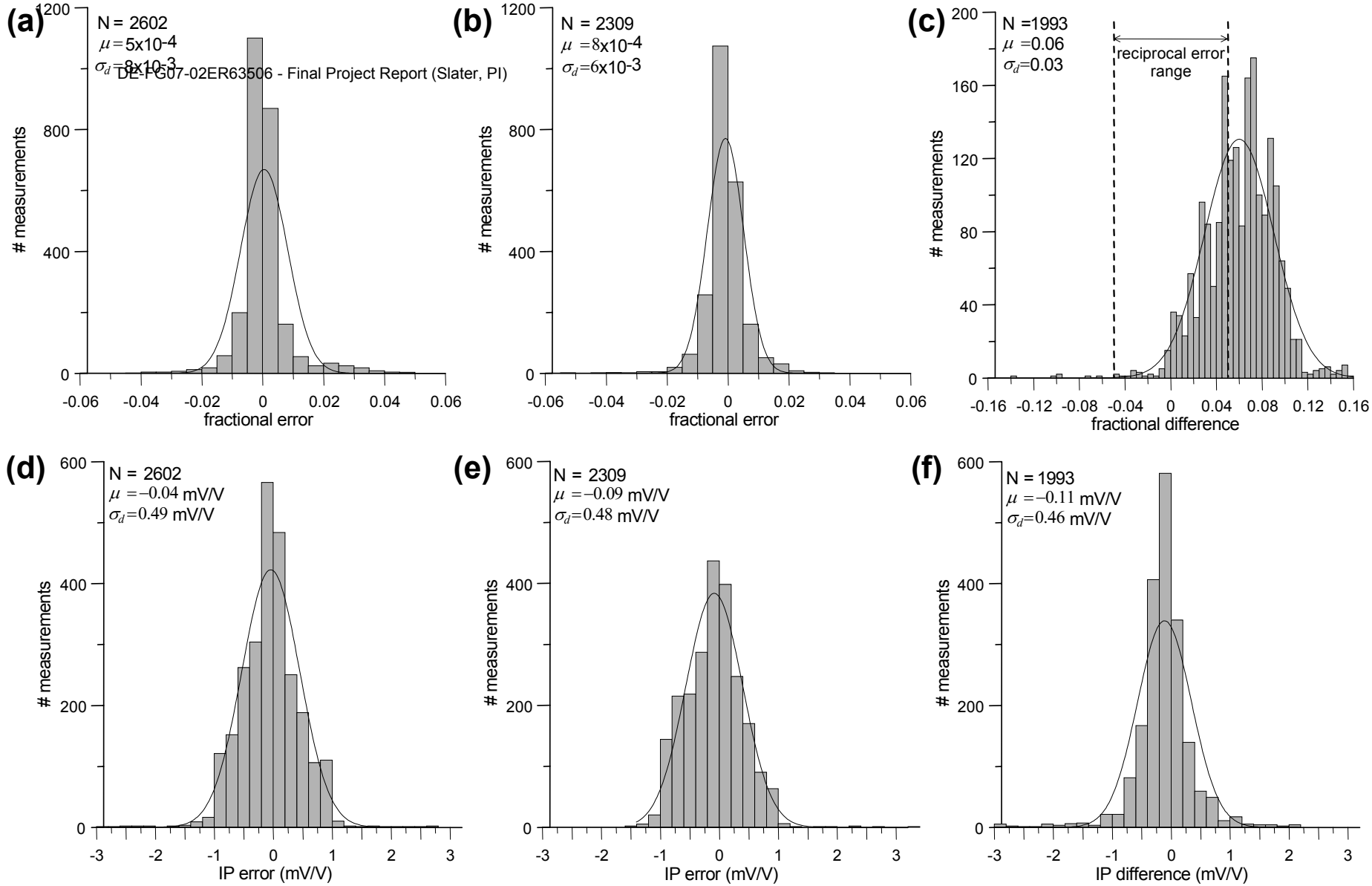

Figure 6: Histogram analysis of the reciprocal errors in the March 04 and May 05 datasets as well as the differences between the two datasets. The resistances are shown as fractional errors whereas the IP measurements are shown as absolute errors (a) March 04 resistance reciprocals (b) May 05 resistance reciprocals (c) difference in the resistances between the May 05 and March 04 datasets (d) March 04 IP reciprocals (e) May 05 IP reciprocals (f) difference in the IP measurements between the May 05 and March 04 datasets. The number of measurements (N), mean (μ), standard deviation (σ_d) and normal distribution are shown for each dataset. Note the difference in the scales in plot (c) relative to plots (a) and (b)

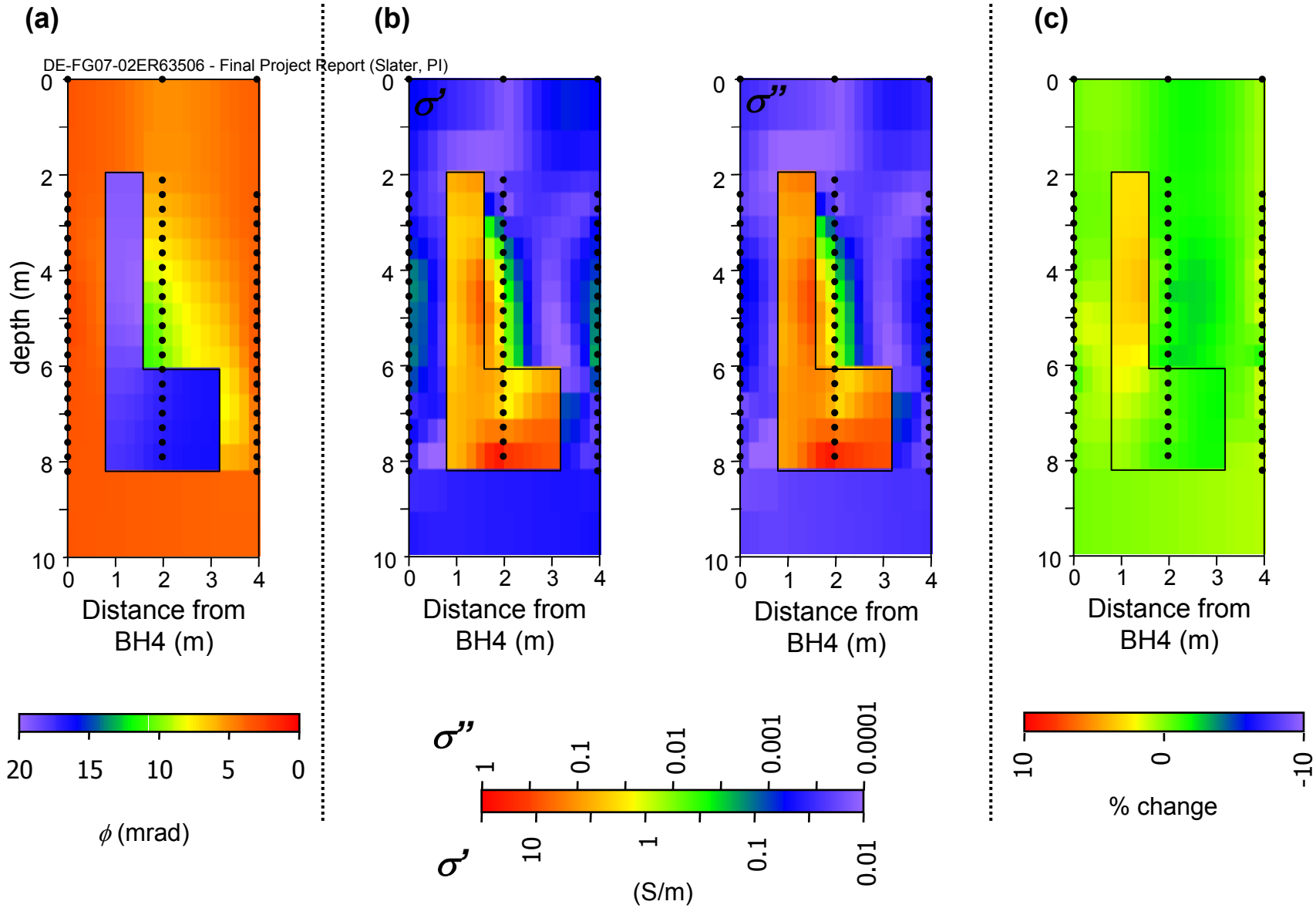

Figure 7. Results of electrical imaging measurements at the Kansas City PRB. The inversion of the March 2004 dataset (2223 measurements used) is shown as (a) phase, and (b) real (σ') and imaginary (σ'') conductivity. Part (c) shows an inversion for percentage changes in σ' in the May 2005 dataset relative to the March 2004 dataset (1993 measurements used). Field datasets were characterized by a standard deviation of 0.05 (fractional error) in the resistance and a standard deviation of 1 mV/V (absolute error) in the chargeability.

APPENDIX 5

Report on groundwater samples from the Kansas City Plant iron wall--samples collected fall 2003

Prepared by Nic Korte, co-PI

1.0 Purpose

The purpose of this report is to interpret groundwater samples taken in and near the Kansas City Plant (KCP) Zero-Valent Iron (ZVI) Permeable Reactive Barrier (PRB). These samples were collected in support of geophysical investigations performed to evaluate physical changes in the barrier. Groundwater had been sampled in and near the barrier in 1999 and 2000 (ORNL 2000). The samples discussed herein were collected in the fall of 2003 to determine whether changes in the geochemical characteristics of the groundwater had occurred since the previous sampling. Besides approximately four years additional aging of the ZVI, changes might have occurred because of the resumption of groundwater pumping downgradient of the PRB. Resumption in pumping might have changed the groundwater flow characteristics at the PRB. Section 2.0 of this report addresses the variation in groundwater geochemistry from the previous sampling period to the current time. Section 3.0 discusses the significance of the measured groundwater parameters with respect to precipitation and biofouling within the PRB. Section 4.0 provides conclusions and recommendations.

2.0 Comparison to Historical Data

Groundwater samples were collected in and around the KCP PRB in 1999 and 2000. The results of that sampling have been discussed previously (ORNL 2000, Laase et al. 2000). The most significant conclusion from the original review of geochemical data was that groundwater apparently did not flow through all of the PRB.

2.1 Sampling Locations

The sampling locations are shown on Figure 1. All of these locations were sampled in previous investigations. Eight wells at six locations were sampled upgradient of the barrier. At some locations, there are two separate well completions. These are designated “U” for upper zone—generally a 5-foot screen at 15-20 feet and “L” for lower zone—a 5-foot screen at the alluvial/bedrock interface, typically between 30 and 42 ft. Four wells, outside and at either end of the barrier were also sampled. Data from all of these wells were used to evaluate any changes in the contaminant plume contacting the barrier.

Eight wells were sampled within the barrier. Data from these wells are useful for evaluating geochemical conditions within the PRB.

Three additional wells sampled are adjacent but downgradient of the PRB. Data from these wells were used to evaluate whether groundwater flowed through the PRB at the specific location.

2.2 Geochemical Results

The results of the groundwater sampling are presented in Table 1. Cation/anion balances indicate excellent data quality. Individual analytes are discussed in the subsections below.

Iron (Fe)—The iron data are unusual for ZVI-PRB sites in that the concentration is higher outside of the barrier than within. The high iron (concentrations ranging to tens of mg/L) outside of the barrier is indicative of the reducing conditions prevalent in the site's groundwater. These data are consistent with previous samplings. Within the barrier, however, the iron concentrations have decreased from the previous sampling, from a few tenths of mg/L to nothing detected in most samples. As noted below, this may be a consequence of precipitation of ferrous sulfides and green rusts.

Manganese (Mn)—The manganese data are analogous to the iron data in that the high dissolved concentrations outside of the barrier (3-10 mg/L) demonstrate reducing conditions are prevalent in the site groundwater. Within the barrier, Mn was typically not detected. These data are consistent with the previously-collected groundwater data.

Calcium (Ca)—The data demonstrate significant removal of calcium by the iron barrier. Typical values for calcium outside of the barrier exceed 200 mg/L, but are often as low as 20 mg/L within the iron. These data are consistent with the previously-collected groundwater data.

Magnesium (Mg)—The data demonstrate significant removal of magnesium by the iron barrier. Typical values for magnesium outside of the barrier exceed 20 mg/L, but are usually 2 mg/L or less within the iron. These data are consistent with the previously-collected groundwater data.

Alkalinity—The data demonstrate significant removal of alkalinity by the iron barrier. Typical values for alkalinity outside of the barrier exceed 500 mg/L, but are 20-40 mg/L within the iron. These data are consistent with the previously-collected groundwater data.

Potassium (K)—The data indicate an increase in potassium within the barrier (from non-detect to 1-4 mg/L). Possibly dissolution from the gravel installed with the iron is the source. These data are consistent with the previously-collected groundwater data.

Sodium (Na)—The data indicate essentially the same concentrations for sodium outside and within the barrier. An increase within the barrier had been noted previously. Perhaps the increase was a consequence of dust introduced during construction. Sodium concentrations are not expected to be affected by interaction with the ZVI.

Chloride (Cl)—The chloride content throughout the system shows little change. There is no evidence of a chloride increase within the barrier. Any chloride produced by the dechlorination of hydrocarbons would be too small an amount to be detected.

Sulfate (SO_4)—The data demonstrate essentially complete removal of sulfate, from up to approximately 100 mg/L to non-detectable. These data are consistent with previous data. However, it is important to note that sulfate was detected at several locations within the barrier soon after construction. Those locations where sulfate was detected now have none detectable. Such data provide direct evidence of the establishment of sulfur-reducing bacteria and the subsequent precipitation of ferrous sulfides and green rusts (See section 3.0).

Electrical Conductivity—Electrical conductivity is a measure of the quantity of ions dissolved in the sample. The previously discussed data shows losses of Fe, Mn, Ca, Mg, alkalinity (carbonate/bicarbonate), and sulfate with the PRB. The trend for conductivity is similar, dropping by approximately 2/3 from outside to within the PRB. A larger decrease is not observed because sodium and chloride, which are not removed by the PRB, are principal contributors to the groundwater's electrical conductivity.

Redox Potential—The redox potential (Eh) can be considered a measure of the reducing or oxidizing power of the groundwater. It can also be a surrogate for an estimate of dissolved oxygen. Eh values that are very positive tend to be rather unreliable because the half reaction $H_2O = ½ O_2 + 2H^+$ is irreversible. Thus, when dissolved oxygen is present (Eh is positive) results may be unreliable. For systems where DO is absent, Eh values are near zero or negative and tend to be more reproducible, although still difficult to relate to specific chemical reactions in groundwater. The presence of dissolved iron and manganese at the KCP indicates anoxic conditions, hence, low or negative Eh values were observed as expected. Conditions within the barrier were more reducing with Eh values approaching -200mv. That conditions are more reducing within the barrier was expected because the reaction of iron with water produces hydrogen.

pH—The pH within the barrier ranges from 9-10 but is 6.6 to 7.2 outside of the PRB. These data, consistent with past results, show little pH buffering within the barrier.

2.3 Concentration Patterns

Those wells expected to be unaffected by the wall, including those that are upgradient and adjacent to the wall (e.g. 210, 212 and 213) show similar concentrations for all of the inorganic analytes. The pattern of contamination for the organic contaminants is also similar to the historical data. There is some variation in contaminant concentration but within a reasonable range.

Results both for inorganic parameters and organic contaminants within the PRB are consistent with historical data. The significance of these results is discussed further in section 3.0.

Highly anomalous data, however, continue to be associated with wells 226 and 245. In conjunction with well 244, these wells are adjacent to and downgradient

of the PRB (Figure 1). As such, water in these wells should show geochemical effects from the PRB. Well 244, adjacent to the north end of the wall, is depleted in calcium, magnesium, alkalinity and sulfate and has an electrical conductivity and pH (9.3) similar to wells located within the ZVI. In contrast, wells 226 and 245, located adjacent to and downgradient of the central and south-central portions of the PRB, show no characteristics of wells affected by the wall. These data indicate groundwater flow from the PRB is not toward wells 226 and 245.

3.0 Mineralogical and Biological Implications

This section discusses the probable reactions occurring within the barrier based on the review of the water quality data.

3.1 Carbonate Precipitates

Because of the disappearance of alkalinity (carbonate/bicarbonate) and the lack of ferrous iron in the barrier samples, $FeCO_3$ (siderite), $CaCO_3$ and $MgCO_3$ are apparently precipitating. All precipitates are carbonates because of the high pH (>9) within the PRB.

3.2 Disappearance of Sulfate

The disappearance of sulfate indicates strong reducing conditions. Eh values for the barrier are -120 to -213 mv (-0.12 to -0.213 v). Converting to pE, the range is -2 to -3.6. Sulfate reduction occurs at approximately pE=-2.5 (Hounslow 1995). Thus, ferrous sulfides (amorphous as well as crystalline mackinawite) are likely forming. The PRB at Oak Ridge National Laboratory (ORNL) contained encrustations of FeS which were believed to be blocking flow in portions of the barrier (Watson 1999, Phillips et al. 2003a,b). Mackinawite (Fe_9S_8), various Fe oxyhydroxides (lepidocrocite, akaganeite, magnetite, and goethite), green rusts (mixture of ferric and ferrous oxyhydroxides sometimes incorporating sulfate and other ions), and amorphous ferrous sulfide all were observed in the Oak Ridge samples. The authors also note that “to date” there is no direct evidence of abiotic sulfate reduction so micro-organisms are apparently responsible for the sulfate loss at the KCP (Phillips et al. 2003a,b).

In column experiments at Oak Ridge, the presence of elevated bicarbonate in sulfate-containing water had significant impact on both geochemical and microbial processes (Gu et al. 1999, Kamolpornwijit et al. 2003). Iron oxyhydroxide and carbonate precipitates were generated in the high bicarbonate systems in both the presence and absence of substantial microbial populations. In addition to causing precipitation of iron oxyhydoxides and carbonate minerals, high concentrations of bicarbonate (with added sulfate) enhanced the corrosion of ZVI and hydrogen production by 4 to 10 fold over sulfate-only influents. (NOTE: the experimental bicarbonate and sulfate concentrations used in some of these experiments were higher than at the KCP but not greatly higher.)

There may be additional significance to the complete disappearance of sulfate at the KCP. Gu et al (1999) suggest that all the sulfate was not consumed in some of

their columns because the residence time was on the order of hours. The residence time at the KCP is designed to be longer, but the question of whether water within the KCP PRB is simply stagnant should also be considered.

3.3 Oxide/Hydroxide Precipitates

Ferric oxide precipitates are sometimes implicated in clogging of PRBs but the low influent Eh at the KCP precludes that possibility. Iron hydroxides may also precipitate although siderite $FeCO_3$ controls the solubility. (See region V, Liang et al. 2000).

3.4 Comparison to a Failed ZVI/PRB

In is instructive to compare the KC site conditions with those of a German ZVI project employing a canister. The latter project is considered a failure of the ZVI technology (Kober et al. 2002). System failure was blamed on high carbonate (9mM or ~550 mg/L). Groundwaters at the KCP and the German site have a similar pH. The KCP has an alkalinity upgradient of the PRB of approximately 600 mg/L as CaCO3. Thus, the KCP water contains more alkalinity than the German site.

Calcium at the German site was 4mM or 160 mg/L which is less than the KCP values of 250-300 upgradient of the PRB. Magnesium values are similar at the two sites. Because calcite is implicated in plugging, the KCP system appears even less favorable geochemically than the German site.

Sulfate at the German site was 1.5 to 2.1 mM or 144 to 200 mg/L. KCP has 80 to 100 mg/L sulfate upgradient of the barrier. Thus, the German site has less favorable conditions than the KCP with respect to sulfate.

Chloride at the German site was 1.5 to 2.3 mM or 50-70 mg/L. The KCP has 100-150 mg/L.

At the German site, all carbonate was removed initially, but as barrier effectiveness decreased, carbonate persisted. pH at the German site was 9 after 24 days, but decreased to 7.5 soon afterward. At the KCP, the carbonate removal and high pH within the barrier indicate the ZVI is not exhausted. Whether this is a consequence of a greater quantity of iron or water not flowing through the barrier cannot be determined from the available data. Nevertheless, based on data from the German site, the same mass of ZVI should be more susceptible to clogging at the KCP.

3.5 Microbial Fouling

Bacteria fouling could be examined at the KCP. However, evidence from other fieldwork suggests diverse bacteria would be found without biofouling (Gu et al. 2002). Moreover, the high pH (9-10) found within the KCP barrier probably precludes significant bacterial build-up. Gu et al. (1999) used high sulfate and carbonate to show that microbial growth eventually occurs. High bicarbonate

buffers the pH, thereby stimulating SRBs (sulfur-reducing bacteria) to use up the sulfate. SRB reduction of sulfate has apparently occurred at the KCP but not to the extent that the pH has decreased within the PRB—at least where sampled by the monitoring wells. In contrast to the KCP where all the sulfate is consumed, at the Oak Ridge barrier only 50% of a 100mg/L sulfate input is consumed (Phillips et al. 2003a,b). The KCP also has 100 mg/L sulfate in the influent water but none is detected inside the barrier. Possibly, differences in residence time and differences in initial conditions (e.g. the Oak Ridge system is oxic) are responsible for this discrepancy. An additional comparison may be made with the Portsmouth site where sulfate decreased from 400 to 150 mg/L (Liang et al. 1997).

3.6 Additional Comparisons with other PRBs

Considering further the Oak Ridge column data (Gu et al. 1999), it can be assumed that the high carbonate columns (3.2 mg/of C per g of Fe) retained the carbon as $FeCO_3$ (siderite). This mineral alone could account for a void volume reduction of ~5% (estimated based on a porosity of ZVI of 0.5 and density of siderite of 3.5 g/cm^3). The precipitates of iron oxyhydroxides and sulfides may account for an additional ~10% void volume reduction. Thus, total reduction could be ~0.42. The actual porosity reduction could be even more because the precipitates may not be densely packed. Such calculations may be possible from data obtained from coring the KCP PRB.

Wilkin et al. (2002) examined two PRBs at the Denver Federal Center. The TDS at these sites is similar (slightly lower) to the KCP. The pH is higher and the Eh is much higher, that is, the system is oxic. The concentration of calcium (~100 mg/L) is lower but sulfate is higher (~230 mg/L). These investigators calculated both sulfate and carbonate loss with depth. They also observed Eh beginning to increase and hydrogen production decreasing within the barrier. Similar observations have not been made at the KCP, again suggesting water may not be flowing through portions of the barrier. Wilkin et al. (2002) also noted that FeS precipitates so quickly sulfide is not detected in the water.

Morrison et al. (2001) reported a higher alkalinity, pH and sulfate for a PRB at Monticello, Utah. pH did not rise significantly in column studies but rose to 9.8 within the barrier. The lack of pH increase in the columns was attributed to the shorter residence time as compared to the PRB. These investigators also reported a decrease in alkalinity (249 mg/L to 22 mg/L) in the field similar to the KCP. Calcium (339 mg/L to 211 mg/L) and sulfate (1190 mg/L to 1160 mg/L) decreased much less. Although reducing conditions were established within the barrier (Eh = -388 mv), sulfur-reducing bacteria have apparently been unable to become established.

Subsequently, Morrison (2003) used the loss of Ca as a means of determining porosity changes. In contrast to the column studies (Morrison et al. 2001), the calcium content of downgradient samples had decreased. By using a large

number of cores, a contour map for calcium in the PRB was prepared. As expected, most precipitation occurred in the upgradient portions of the PRB.

Phillips et al. (2003b) reported on mineralogical characteristics and transformations during long-term operation of the Oak Ridge ZVI system. Data from samples collected at 15 months were compared to data collected at 30months. Based on their observations and analyses, they suggested the upgradient side of the barrier may last less than 5 years. The paper reported several transformations from one mineral to another during the interval between samplings. The authors were also able to separate reduced from oxidized zones by the minerals and by the appearance of the samples. Oxidized zones, however, are not expected at the KCP because of the anoxic nature of the water.

4 Conclusions and Recommendations

The primary conclusions from this review are threefold. First, there is no geochemical evidence of a change in groundwater flow patterns since the PRB was installed. This conclusion holds despite the resumption of groundwater pumping downgradient of the PRB. Second, the geochemical evidence continues to indicate there is little or no flow out of the central and southern portions of the PRB. This latter conclusion is tempered by there being only three monitoring points along the 130 foot length (Figure 1). Finally, the geochemical data are consistent with what would be predicted based on theoretical calculations (e.g. Liang et al. 2000) and data from other PRBs. Thus, the presence within the KCP PRB of certain precipitates (e.g. siderite, mackinawite, etc.) can be predicted with confidence.

The primary recommendation is to use coring to evaluate further the flow characteristics of the PRB. Coring may provide the following information:

- Visual inspection can be used to compare the amount of precipitate and degree of encrustation from one location to another.
- A mass balance can be calculated based on the contents of calcium, sulfate and carbon to estimate how much water has flowed into the PRB. Coring might also be used to determine whether the heterogeneities presumed to exist downgradient of the PRB exist at all or are in similar locations upgradient.

A difficulty with the recommendation to perform coring is whether sufficient sampling can be performed within the scope and budget of the current project. For example, Morrison (2003) collected seventy separate cores from a similarly-sized PRB in Monticello, Utah. Although the author notes many fewer samples may have been adequate for certain analytes, there will be no way of knowing a'priori how many samples are necessary for the KCP barrier. Hence, the performance of a mass balance may be semi-quantitative at best.

5 References

Gu, B., T. Phelps, L. Liang, M. Dickey, Y. Roh, B. Kinsall, A. Palumbo, and G. Jacobs. 1999. Biogeochemical dynamics in zero-valent iron columns: Implications for permeable reactive barriers. Environ. Sci. Technol. 32:2170-2177.

Gu, B., D.B. Watson, L. Wu, D. Phillips, D.C. White, and J. Zhou. 2002. Microbiological characteristics in a zero-valent iron reactive barrier. Environmental Monitoring and Assessment. 77:293-309.

Hounslow, A.W. 1995. Water Quality Data: Analysis and Interpretation. CRC Press.

Kamolpornwijit, W., L. Liang, O.R. West, G.R. Moline, and A.B. Sullivan. 2003. Preferential flow path development and its influence on long-term PRB performance: column study. Journal of Contaminant Hydrology. 66:161-178.

Kober, R., S. Schlicker, M. Ebert, and A. Dahmke. 2002. Degradation of chlorinated ethylenes by Fe^{o}: inhibition processes and mineral precipitation. Environmental Geology. 41:644-652.

Laase, A., N. Korte, J. Baker, P. Dieckmann, J. Vogan, and R. Focht. 2000. Evaluation of the Kansas City Plant Iron Wall. 2nd International Conference on Remediation of Chlorinated and Recalcitrant Compounds. May 2000, Monterey, California.

Liang, L., O.R. West, N. Korte, J. Goodlaxson, D. Pickering, J. Zutman, F. Anderson, C. Welch, M. Pelfrey, and M. Dickey. 1997. The X-625 Groundwater Treatment Facility: A field-scale test of trichloroethylene dechlorination using iron filings for the X-120/X-749 Groundwater Plume. Oak Ridge National Laboratory. ORNL/TM-13410. Oak Ridge, TN.

Liang, L., N. Korte, B. Gu, R. Puls and C. Reeter. 2000. Geochemical and microbial reactions affecting the long-term performance of in situ “iron barriers.” Advances in Environmental Research. 4:273-286.

Morrison, S., D. Metzler, and C. Carpenter. 2001. Uranium precipitation in a permeable reactive barrier by progressive irreversible dissolution of zerovalent iron. Environ. Sci. Technol. 35:385-390.

Morrison, S. 2003. Performance evaluation of a permeable reactive barrier using reaction products as tracers. Environ.Sci. Technol. 37:2302-2309.

ORNL (Oak Ridge National Laboratory) 2000. Lower Northeast Area Characterization and Iron Wall Evaluation Report. June 2000, Grand Junction, Colorado.

Phillips, D. B. Gu, D.B. Watson, and Y. Roh. 2003a. Impact of sample preparation on mineralogical analysis of zero-valent iron reactive barrier materials. J. Environ. Qual. 32:1299-1305.

Phillips, D., D.B. Watson, Y. Roh, and B. Gu. 2003b. Mineralogical characteristics and transformations during long-term operation of a zero-valent iron reactive barrier. J. Environ. Qual. 32:2033-2045.

Watson, D. 1999. Oak Ridge National Laboratory, personal communication with N. Korte.

Wilkin, R.T., R.W. Puls, and G.W. Sewell. 2003. Long-term performance of permeable reactive barriers using zero-valent iron: geochemical and microbiological effects. Ground Water. 41(4):493-503.

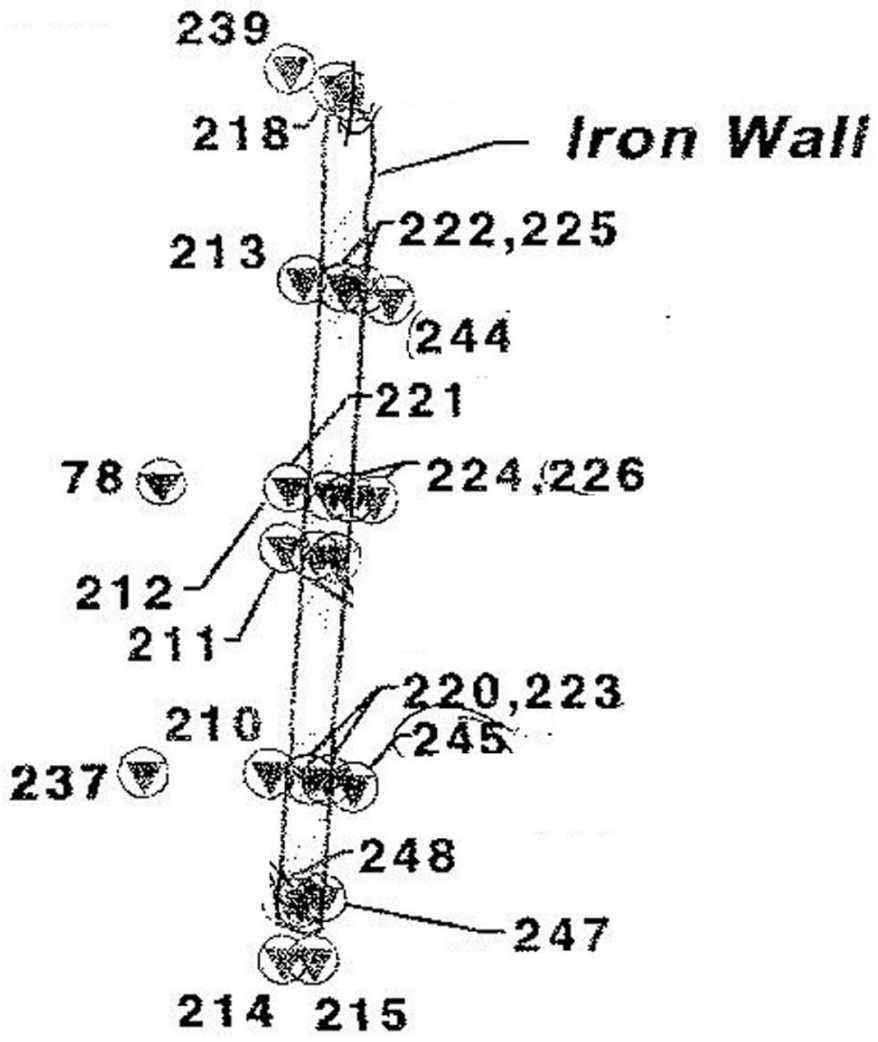

Figure 1. Groundwater Sampling Locations: KCP PRB, Fall 2004

Table 1. Monitoring data from the groundwater wells.

Well # Analyte	1,2-DCE	Vinyl chloride	pH	CDT	Tur-bidity	Eh	Alk-alinity	Ca	Mg	Mn	silica	Fe	SO_4	Ion Balance
Upgradient														
78U	86	1.2	6.6	1791	0.7	13.1	645	335	22.1	18.5	27.5		87.7	3.79
78L	89	18										2.65		
237U	18	0	6.9	1296	3	13.3	579	256	13.7	3.93	23.2	0.109	103	3.89
237L	230	140												
210	140	170	6.8	1247	2	-118	452	181	16.4	3.55	36.8	25	25.8	
211U	89	8.7	6.6	1459	3.1	-36	673	293	21.1	5.68	23.8	0.352	61.3	3.96
212	140	120	6.7	1318	2.3	-112.2	533	207	19.6	2.06	40.8	35.5	16.1	3.2
213	1.3	11	6.6	1296	5.5	-105.2	553	207	18.7	3.86	45.5	41.5	9.18	3.97
downgradient														
226	1.6	94	6.7	1361	7.4	-113.5	474	238	16.2	2.93	38.3	19.4	21	4.43
244	0	0	9.3	405	0.5	-129.8	30	37.8	1.35	0.01	1.7	0.0525	85.8	0.17
245	6.4	97	7.2	1087	2.3	-124.9	422	178	15.5	4.24	45.9	25.3	34.8	4.87
Inside														
220	0	0	9	542	1.1	-182.9	34	36.2	1.89	0	0	0	0	4.81
221	0	0	9	477	3	-174	20	33.9	0.404	0	5.61	0	0	
222	0	0	9.8	257	1.8	-170	49	13.9	0.07	0	1.69	0	0	1.55
223	0.69	0	9.7	498	0.7	-119.9	36	31.8	2.76	0.007	0		0	1.33
224	0	0	9.3	451	2.7	-116.9	20	32.2	0.572	0	3.38	0	0	3.27
225	0	0	10	155	2.6	-213.6	47	5.64	0.23	0	2.88	0.053	1.9	5.1
247	0.56	0	9.9	429	2	-135	27	30	1.9	0	2.8	0	0	3.22
248	2.9	0	9.4	460	0.3	-150.7	35	26.2	2.18	0	19.1		0	3.71
ends														
214	8.5	0	6.6	1102	7.5	-90.5	580	205	17	9.97	29.6	2.31	102	2.92
215	0	0	6.7	1049	5	-114	390	147	16.7	4.43	55.2	3.21	28.9	0.63
218	0	0	6.6	1731	10.3	-109.4	701	199	29.4	4.53	36.4	34.5	1.16	2.45
239			6.7	1380	28.5	-107	432	197	15	6.9	42	45.9	89	3.97

APPENDIX 6

Report on iron coring of the Kansas City Plant iron wall--samples collected May 2005

Prepared by Nic Korte, co-PI

1.0 Purpose

This report describes geochemical analyses of core samples collected May, 2005 from the Kansas City Plant (KCP) Zero-Valent Iron (ZVI) Permeable Reactive Barrier (PRB). The purpose was to determine whether the solid phase composition of the PRB was consistent with previous data and to support geophysical and mineralogical studies performed by personnel from Rutgers University.

1.1 Description of the KCP PRB

The Kansas City barrier resides on relatively impermeable sandstone bedrock and consists of a 6 ft by 6 ft zone of iron overlain by an additional14 feet of barrier composed of 2 ft of iron and 4 ft of sand (Figure 1). The barrier had not been cored previously but extensive hydraulic and geochemical studies had been performed. For example, groundwater samples were collected in and around the KCP PRB in 1999 and 2000 as part of a hydraulic examination of the barrier (ORNL 2000, Laase et al. 2000). A subsequent groundwater evaluation was performed as part of the present project (Korte 2004). The most significant conclusion from the previous studies was that groundwater flow through the barrier was impeded, particularly on the north end.

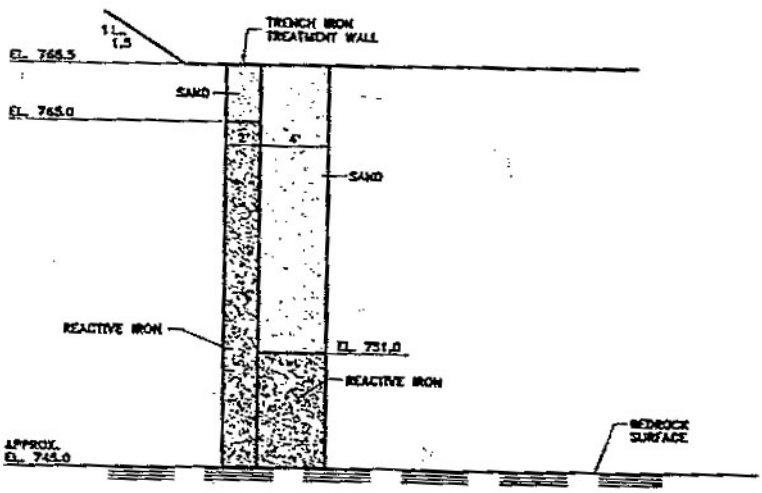

Figure 1. Schematic of KCP-PRB

1.2 Report Description

Section 2.0 describes the data acquisition and presents the data. Section 3.0 discusses the significance of the data with comparisons to previous results from the KCP-PRB and reports in the literature. Section 4.0 provides conclusions and recommendations.

1.3 Sampling and Analysis Program

A sampling plan was prepared by N. Korte—KCP consultant, and revised based on reviews from the KCP, Rutgers, and GEO-Consultants. GEO Consultants (Kevil, KY) supervised sample collection which employed a standard Geoprobe system with a 4-ft sampler. Vertical and angle cores were collected so that precipitates within the barrier could be examined horizontally and vertically. The emphases of the sampling and analyses were to evaluate the upgradient interface and the condition of the iron within the barrier.

2.1 Sample Locations

ANGLE CORES—Six angle cores were collected in three general locations of the PRB. These are borings 1 through 6 as shown on Figure 2. (Borings 2, 3 and 4 were not subjected to geochemical analyses and are not discussed in this report.)

- PRB-1—Two borings were needed because a sampling interval was inadvertently missed initially. PRB-1A and PRB1-B are on the same transect. PRB-1A was drilled 8 ft from the upgradient face of the wall and PRB-1B 7 ft from the upgradient face.
- PRB-5—This boring was drilled from 15 ft upgradient of the face of the wall.
- PRB-6—This boring was drilled from 15 ft upgradient of the face of the wall.

The drilling intercepted the PRB with reference to groundwater monitoring wells 244, 226 and 245 (Figure 2). These wells are downgradient, although the coring “aimed” at the wells from the upgradient side. The locations were selected both to provide spatial coverage of the wall and to sample locations where contaminants are believed to be flowing through the wall and where they are not.

VERTICAL CORES—Three cores (#s 7, 8, and 9) were collected vertically (Figure 2). Two borings were performed along the interface of the upgradient portion of the barrier. Hence, as shown in figure 1, these cores intercepted the entire length of the iron while the third vertical boring was performed along this same hypothetical line for well 244, but intercepted only the bottom 6 ft.

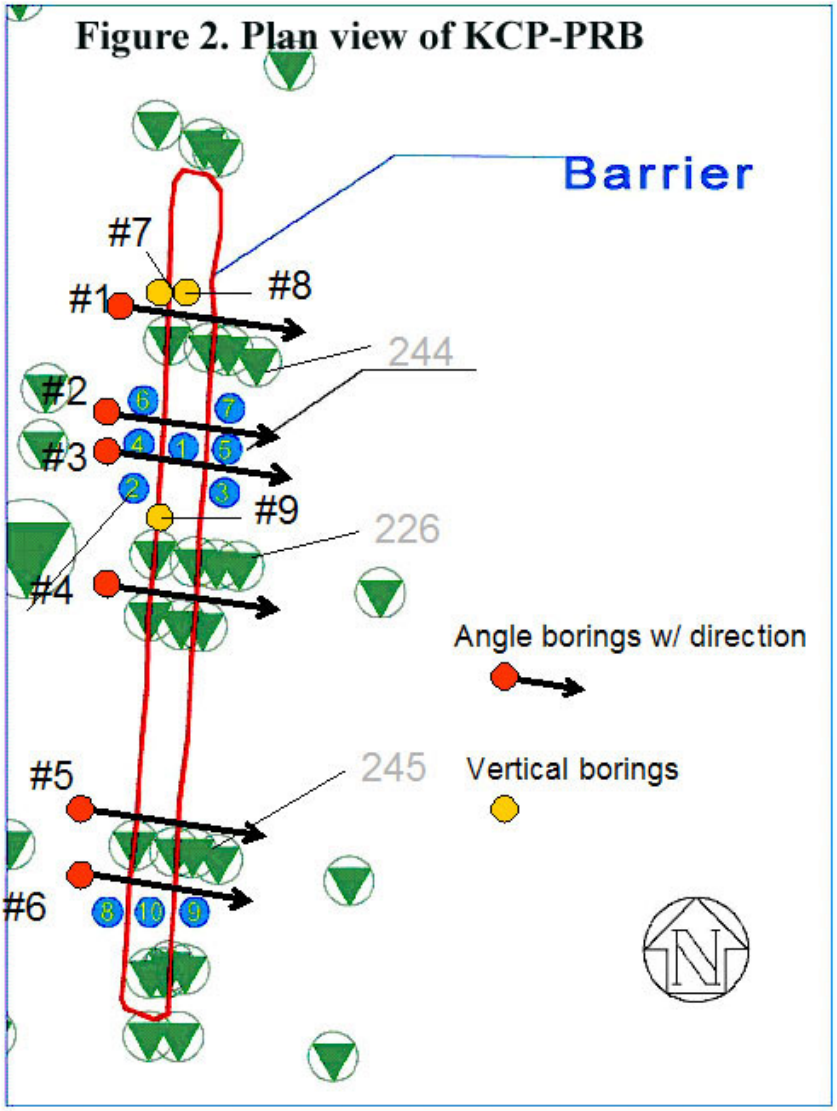
Figure 2. Plan view of KCP-PRB
Barrier
#7
#8
#1
244
#2
#3
#9
226
#4
Angle borings w/ direction
#5
245
Vertical borings
#6
N

2.2 Sampling

ANGLE CORES: Core samples were collected with the Geoprobe. Continuous sampling ensued once the PRB was encountered.

(1) The first sample contained soil upgradient of the PRB and included the interface and as much additional iron from the PRB as fit in the standard sampling sleeve. Figure 3 illustrates the appearance of this core from a test sample collected while evaluating drilling and sampling methods.
(2) Additional cores were collected with a standard sampling sleeve and were collected continuously following the first sample.
(3) Cores 1, 5, and 6 had samples submitted for geochemical analysis. Cores 2, 3 and 4 were used for geophysical and mineralogical analyses only. Data for the latter three cores are reported elsewhere.

VERTICAL CORES: There were two types of vertical cores.

(1) One of the vertical cores (#8) was collected within the PRB. This core intersected approximately 6 feet of iron. Samples were collected approximately from the top, middle and base of the iron. The other vertical cores (#7 and #9) intersected 16 and 17 feet of iron respectively. Seven samples were collected from each of these cores.

Figure 3. Angle Core Showing iron/soil interface.

2.2 Sample Handling

ANGLE CORES: Cores were argon-bathed to limit air contact (Philips et al. 2003a), and marked regarding length, orientation, and for loss of length if void space was encountered. Samples were taped to prevent air contact and packed to remain at 4° C for shipping.

VERTICAL CORES: Iron from the vertical cores was briefly mixed in a stainless steel bowl with a stainless steel spatula. Two splits from each sample location were prepared. One was packed for shipment to the EPA Kerr Laboratory in Ada, Oklahoma and the other sample was delivered locally to Pace, Laboratory in Lenexa, KS. .

2.3 Geochemical Results

The results of the core analyses are presented in Tables 1 and 2.

Table 1. Geochemical results for angle cores (mg/kg).

Sample Name	Color[1]	Inorganic Carbon	Calcium	Silicon	Sulfur
PRB 1b port 0-1	rust/black	204	nd	nd	69
PRB 1b port 1-2	rust/black	367	119	nd	49
PRB 1b port 2-3	rust/black	269	nd	nd	59
PRB 1b port 3-4	rust	373	nd	nd	161
PRB 1b port 4-5	sand	634	1580	444	81
PRB 1b port 5-6	black	11	526	nd	77
PRB 1b port 6-7	rust	168	nd	nd	63
PRB 1b port 7-8	rust	246	nd	nd	31
PRB 5 port 1-2	brown	25	295	nd	1
PRB 5 port 2-3	rust	110	998	nd	50
PRB 5 port 3-4	brown	128	276	nd	40
PRB 5 port 4-5	brown	228	263	nd	56
PRB 5 port 5-6	brown	252	248	nd	68
PRB 6 port 1-2	rust	128	nd	nd	39
PRB 6 port 2-3	brown	17	nd	nd	38
PRB 6 port 3-4	brown	116	nd	nd	54
PRB 6 port 4-5	brown	60	nd	nd	24

[1]Color as recorded by EPA laboratory personnel upon sample receipt.

Table 2. Geochemical results for vertical cores (mg/kg)

Sample Name	Color[1]	Inorganic Carbon	Calcium	Silicon	Sulfur
PRB 7 9-10	black	41	289	nd	28
PRB 7 13-13.5	black	33	1600	nd	28
PRB 7 17-17.5	rust	19	525	nd	25
PRB 7 19.5-20	rust	24	498	nd	58
PRB 7 20-20.5A	rust	399	363	nd	85
PRB 7 22-22.5A	rust	5737	6310	nd	1225
PRB 7 24-24.6A	brown	834	2370	nd	91
PRB 8 20-20.5A	rust	99	283	nd	58
PRB 8 22-22.5A	rust	7	179	nd	40
PRB 8 24-24.5A	brown	160	694	nd	38
PRB 9 12-12.5	black	46	199	nd	43
PRB 9 13-13.5	black	54	134	nd	55
PRB 9 16.5-17	brown	32	180	nd	36
PRB 9 17-17.5	brown	82	186	nd	90
PRB 9 21-21.5	rust	80	157	nd	43
PRB 9 25.5-26A	rust	1130	980	nd	142
PRB 9 28.5-29A	brown	647	12100	nd	84

[1]Color as recorded by EPA laboratory personnel upon sample receipt.

3.0 Data Interpretation

Previously-collected groundwater and hydraulic data has indicated there is flow through the PRB (Figure 2) on the north end, but that flow through the barrier is either not occurring or is very much restricted at the south. Moreover, hydraulic data has confirmed a significantly higher mass flux through a basal gravel zone relative to the silty clay portions higher in the aquifer. It was expected, therefore, that data from the core samples would be consistent with the previous interpretations.

Silicon (Si)—Other research has postulated a role for precipitation of silica in the fouling of PRBs. Accordingly, samples were submitted for total Si analysis. Unfortunately, laboratory detection limits were relatively high. The only value reported is sufficiently near the detection limit that, in the absence of other quantitative results, no interpretation is possible.

Calcium (Ca)—Groundwater data reported previously (Korte 2004) demonstrated significant removal of calcium by the iron barrier. However, because calcium carbonate precipitates rapidly, the disappearance of calcium in the groundwater provides no information regarding the amount of flow through that portion of the barrier. A review of the core data indicates overall good contrast, but some samples inexplicably were reported at non-detect. Nonetheless, the data support the groundwater and hydraulic data. For example, vertical cores 7 and 9 (front edge of barrier) have much higher

concentrations (up to 1-2 orders of magnitude) of Ca in the basal gravel zone indicating preferential flow at the bottom of the aquifer. Similarly, cores 7 and 9, being closer to the front of the barrier have, as expected, higher values for calcium than boring 8. Calcium removal tends to be rapid such that highest values are found near the upgradient interface.

The data also show much higher concentrations of calcium in the northern vertical core (#7) versus the core from the center (#9). Such data also demonstrate more flow through the northern end. Note that the deepest sample has a lower concentration, but according to the description, this sample contained soil as well as iron. Thus, the sample collected just above this bottom sample illustrates the conditions in the basal gravel.

The data from the angle cores is also consistent with previous interpretations. The angle cores have two to three times more calcium in the north (core 1) than in the south (cores 5 and 6) indicating that more water must be flowing through the north end. Indeed, no calcium was detected in core #6 suggesting little or no flow is occurring at the extreme south end of the barrier.

Sulfur (S)—Groundwater data demonstrated essentially complete removal of sulfate, from up to approximately 100 mg/L to non-detectable (Korte 2004). As with calcium, the sulfur data indicate more removal on the north end of the wall. Vertical core # 7 has much higher S in the basal gravel than 9, which indicates more flow at the north than in the middle. The angle cores also suggest more removal in the north end, although except for one or two values the contrast is low.

The disappearance of sulfate in the groundwater samples and its precipitation in the barrier indicates strong reducing conditions. Eh values for the barrier are -120 to -213 mv (-0.12 to -0.213 v). Converting to pE, the range is -2 to -3.6. Sulfate reduction occurs at approximately pE=-2.5 (Hounslow 1995). Thus, ferrous sulfides (amorphous as well as crystalline mackinawite) have probably formed (Watson 1999, Phillips et al. 2003a,b). Mackinawite (Fe_9S_8), various Fe oxyhydroxides (lepidocrocite, akaganeite, magnetite, and goethite), green rusts (mixture of ferric and ferrous oxyhydroxides sometimes incorporating sulfate and other ions), and amorphous ferrous sulfide all were reported by these authors who noted that “to date” there is no direct evidence of abiotic sulfate reduction. Apparently, microbial activity is responsible for the sulfate loss at the KCP (Phillips et al. 2003a,b).

Inorganic Carbon—The inorganic carbon data provide the best contrast and most consistent interpretation. Inorganic carbon in groundwater, similar to calcium and sulfur and as indicated by alkalinity results, showed significant removal within the barrier. Typical values for alkalinity outside of the barrier exceed 500 mg/L, but are 20-40 mg/L within the iron. Vertical cores 7 and 9 (front of barrier) show much higher concentrations (up to 1-2 orders of magnitude) of inorganic carbon in the basal gravel zone indicating preferential flow at the bottom of the aquifer. These data are consistent with the angle cores which show the highest values on the north and the lowest in the south. Presumably, the disappearance of alkalinity (carbonate/bicarbonate) and the lack of

ferrous iron in the barrier samples, indicates precipitation of $FeCO_3$ (siderite) and $CaCO_3$. Carbonates will dominate because of the high pH (>9) within the PRB (Korte 2004).

3.1 Reactivity Loss within the PRB

A previous report (Korte 2004) compared the groundwater characteristics of the KCP PRB to a German site where the ZVI technology was considered a failure (Kober et al. 2002). Based on data from the German site, the same mass of ZVI should be more susceptible to clogging at the KCP. At the German site, all carbonate was removed initially, but as barrier effectiveness decreased, carbonate persisted. pH at the German site was 9 after 24 days, but decreased to 7.5 soon afterward. At the KCP, the carbonate removal and high pH within the barrier indicate the ZVI is not exhausted. Additionally, the relatively low inorganic carbon values suggest much more removal is possible. Whether the remaining reactivity is a consequence of a greater quantity of iron or water not flowing through the barrier cannot be determined from the available data.

3.2 Porosity Loss within the PRB

Considering data from the literature, Gu et al. 1999 showed that 3.2 mg/of C per g of Fe could account for a void volume reduction of ~5% (estimated based on a porosity of ZVI of 0.5 and density of siderite of 3.5 g/cm^3). The highest reported value in the KCP data (~0.6 mg/g) is a factor of five lower and all other KCP values are at least another order of magnitude lower yet. Similarly, Morrison et al. (2001) measured calcium values in seventy cores (four samples per core) from a PRB in Utah. Calcium values averaged two orders of magnitude higher than those at the KCP. Morrison (2001) estimated the volume of calcite deposited as 3.2% of the total porosity. Hence, calcium data from the KCP do not indicate imminent problems with loss of porosity. Indeed, the low level of calcium at the KCP is probably an indication that there is little flow through the barrier.

4.0Conclusions

It is emphasized that the conclusions and indications discussed in this report are based on a small number of samples. For example, Morrison (2001) used 70 vertical cores, 4 samples per core (280 total samples) to develop a concentration profile for a PRB. Although interpretation of Morrison's data indicated fewer samples would have been sufficient, the adequacy of sampling cannot be addressed for the KCP barrier. Nonetheless, the groundwater geochemical results, hydraulic testing, and now core data all indicate the same overall interpretations for the KCP PRB as follows:

- The mass of groundwater flowing through the basal gravel is higher than elsewhere along the vertical height of the aquifer.
- Groundwater flow through the south end is apparently much less than at the north. The data suggest a gradient of decreasing flow through the barrier from north to south.

The relative magnitude of the calcium, sulfur and inorganic carbon precipitated also suggest two other conclusions when the data are compared to results reported elsewhere:

- To date, porosity of the barrier has not been significantly affected by precipitation.

- The relatively low values for precipitates indicate a low mass flux through the barrier.

5. References

Gu, B., T. Phelps, L. Liang, M. Dickey, Y. Roh, B. Kinsall, A. Palumbo, and G. Jacobs. 1999. Biogeochemical dynamics in zero-valent iron columns: Implications for permeable reactive barriers. Environ. Sci. Technol. 32:2170-2177.

Gu, B., D.B. Watson, L. Wu, D. Phillips, D.C. White, and J. Zhou. 2002. Microbiological characteristics in a zero-valent iron reactive barrier. Environmental Monitoring and Assessment. 77:293-309.

Hounslow, A.W. 1995. Water Quality Data: Analysis and Interpretation. CRC Press.

Kamolpornwijit, W., L. Liang, O.R. West, G.R. Moline, and A.B. Sullivan. 2003. Preferential flow path development and its influence on long-term PRB performance: column study. Journal of Contaminant Hydrology. 66:161-178.

Kober, R., S. Schlicker, M. Ebert, and A. Dahmke. 2002. Degradation of chlorinated ethylenes by Fe^{o}: inhibition processes and mineral precipitation. Environmental Geology. 41:644-652.

Korte, N. 2004. Report on Groundwater Samples Collected from the Kansas City Plant Iron Wall—Samples Collected Fall 2003. Project Report to J. Baker, Kansas City Plant and to Lee Slater, Principal Investigator, In support of: EMSP #88615: ER63506-1020409-0009643, Investigating the potential for long-term permeable reactive barrier (PRB) monitoring from the electrical signatures associated with the reduction in reactive iron performance.

Laase, A., N. Korte, J. Baker, P. Dieckmann, J. Vogan, and R. Focht. 2000. Evaluation of the Kansas City Plant Iron Wall. 2nd International Conference on Remediation of Chlorinated and Recalcitrant Compounds. May 2000, Monterey, California.

Liang, L., O.R. West, N. Korte, J. Goodlaxson, D. Pickering, J. Zutman, F. Anderson, C. Welch, M. Pelfrey, and M. Dickey. 1997. The X-625 Groundwater Treatment Facility: A field-scale test of trichloroethylene dechlorination using iron filings for the X-120/X-749 Groundwater Plume. Oak Ridge National Laboratory. ORNL/TM-13410. Oak Ridge, TN.

Liang, L., N. Korte, B. Gu, R. Puls and C. Reeter. 2000. Geochemical and microbial reactions affecting the long-term performance of in situ “iron barriers.” Advances in Environmental Research. 4:273-286.

Morrison, S., D. Metzler, and C. Carpenter. 2001. Uranium precipitation in a permeable reactive barrier by progressive irreversible dissolution of zerovalent iron. Environ. Sci. Technol. 35:385-390.

Morrison, S. 2003. Performance evaluation of a permeable reactive barrier using reaction products as tracers. Environ.Sci. Technol. 37:2302-2309.

ORNL (Oak Ridge National Laboratory) 2000. Lower Northeast Area Characterization and Iron Wall Evaluation Report. June 2000, Grand Junction, Colorado.

Phillips, D. B. Gu, D.B. Watson, and Y. Roh. 2003a. Impact of sample preparation on mineralogical analysis of zero-valent iron reactive barrier materials. J. Environ. Qual. 32:1299-1305.

Phillips, D., D.B. Watson, Y. Roh, and B. Gu. 2003b. Mineralogical characteristics and transformations during long-term operation of a zero-valent iron reactive barrier. J. Environ. Qual. 32:2033-2045.

Watson, D. 1999. Oak Ridge National Laboratory, personal communication with N. Korte.

Wilkin, R.T., R.W. Puls, and G.W. Sewell. 2003. Long-term performance of permeable reactive barriers using zero-valent iron: geochemical and microbiological effects. Ground Water. 41(4):493-503.

ACKNOWLEDGEMENTS
The assistance of Richard Wilkin, U.S. Environmental Protection Agency, Kerr Laboratory, Ada, Oklahoma, for providing the sulfur and carbonate analyses is gratefully acknowledged.